AD-A253 605

(2)

AUTOMATED HANDLING AND ASSEMBLING OF NON-RIGID OBJECTS

Fifth Semiannual Report

for period

16 January 1992 through 15 July 1992

DTIC
S ELECTE JUL 23 1992 D
A

for

OFFICE OF NAVAL RESEARCH

on

Contract No. N00014-90-J-1516

by

Yuan F. Zheng
Principal Investigator
Dept. of Electrical Engineering
The Ohio State University
Columbus, OH 43210

This document has been approved for public release and sale; its distribution is unlimited.

92-19372

92 7 21 047

TABLE OF CONTENTS

1. INTRODUCTION 1

2. PASSIVE AND ACTIVE STEREO VISION FOR SMOOTH SURFACE DETECTION OF DEFORMED PLATES 2

   2.1 Passive Stereo Vision to Reduce the Likelihood of the False-Boundary Problem 2

   2.2 Matching Criteria in Active Stereo Vision 3

   2.3 Dynamic Sensing Process 6

3. ERROR ANALYSIS ON THE NON-CONTACT 3-D DIGITIZING SYSTEMS 8

4. RESEARCH ACTIVITIES FOR THE NEXT PERIOD 11

APPENDIX A

PASSIVE AND ACTIVE STEREO VISION FOR SMOOTH SURFACE DETECTION OF DEFORMED PLATES 14

APPENDIX B

DIGITIZING AN UNKNOWN SURFACE WITH MULTIPLE NON-CONTACT LASER SENSORS 45

DTIC QUALITY INSPECTED 3

Accesion For
NTIS CRA&I ☒
DTIC TAB ☐
Unannounced ☐
Justification ....
By pn A 245321
Distribution /
Availability Codes
Dist | Avail and/or Special
A-1

1. INTRODUCTION

This is the fifth semi-annual report of the project entitled "Automated Handling and Assembling of Non-Rigid Objects". This report covers the period from January 16, 1992 to July 15, 1992.

The objective of this research project is to identify mechanisms for automated handling and assembling of non-rigid objects. To accomplish the goal, four aspects of the problem have been identified in our original proposal. They are -

a. Study the deformation characteristics of non-rigid materials.

b. Investigate optimal tool structures for handling non-rigid objects.

c. Develop sensing mechanisms to locate non-rigid objects.

d. Develop motion control mechanisms for the host machines.

To explore these aspects, many technical issues need to be examined. During the past six months, two topics were studied by the Principal Investigator and his team. The first topic investigates methods for detecting smooth surfaces of deformed plates. This study is beneficial in many applications where metal plates are used such as in shipbuilding, automobile, and aerospace industries. In order to automatically handle the deformable plates, the shape of the plate must be detected. One difficulty in detecting such a shape is that the smooth surfaces of deformed plates do not have matching features for stereo vision to use. We propose a passive-active stereo vision method for this purpose. Passive stereo vision without the projection of structured light is used to obtain the boundary of the smooth surfaces, and active stereo vision with the projection of structured light is applied to detect the details of the surface. An inherent problem in stereo vision, called the false boundary problem, is identified and solved by calibrating the structured light.

The second topic continues the study of digitizing an unknown surface using laser displacement sensors (LDS). As mentioned in the fourth semi-annual report, vision sensors can only identify the global shape of a deformed object. To precisely measure the profile of an unknown surface, a touch probe has customarily been used to digitize the surface. This process of digitizing is very slow due to a large number of contacts that need to be made by the probe. We have proposed to use non-contact laser displacement sensors (LDS) to speed up the measurement process. In the fourth semi-annual report, we described two approaches to using the LDS, i.e., the multiple beam approach and the extrapolation approach. During the past six months, we also studied precision issues associated with the two approaches. Through this study, we have shown that the digitizing error parameters are bounded functions when using these two approaches to digitize an unknown surface which has a finite maximum curvature. These functions can be used to determine an adequate sampling arc length, if the maximum surface curvature is known, or they can be used to determine the maximum surface curvature that can be accurately digitized for a given sampling length.

In the next two sections, research results of the above two topics will be summarized. Detailed descriptions of these two studies can be found in Appendices A and B respectively.

2. PASSIVE AND ACTIVE STEREO VISION FOR SMOOTH SURFACE DETECTION OF DEFORMED PLATES

In this study, we consider to use stereo vision to detect the 3-D shape of deformed plates. This study is necessary when the handling of deformable plates needs to be automated.

Stereo vision is an attractive technique for depth perception in many applications. For detecting the shape of deformed plates, however, special problems need to be considered. The first problem is called the **false boundary** problem, which is caused by the curved surface of deformed plates. When this occurs, the actual boundary of the surface may be hidden from the camera. The second problem is that the smooth surface does not generate matching features in the image pair of stereo vision. As a result, the depth of the object cannot be derived directly by matching extracted features through the triangulation method. To solve the preceding problems, we propose a passive-active stereo vision method plus a dynamic sensing process. Essentially, we use passive stereo vision to detect the boundary of the curved surface. Active stereo vision with the projection of structured light is then used to detect the details of the surface. The passive-active stereo vision is further enhanced by a *dynamic sensing process*. That is, the stereo vision system is dynamically positioned and oriented to effectively detect the shape of a deformed plate.

2.1 Passive Stereo Vision to Reduce the Likelihood of the False-Boundary Problem

When a surface is seen by the two cameras of stereo vision, the boundary of the surface detected in each camera might not correspond to the actual boundary of the surface. Shown in Fig. 1 are two examples of this problem. In (a) of Fig. 1, the right side of the surface boundary is hidden from the left camera, and the left side of the surface boundary is hidden from the right camera. In (b) of Fig. 1, the lower side of the surface boundary is hidden from both cameras.

Two methods are proposed to eliminate the false boundary problem. One method is to orient the center line of the stereo vision sensor in order that the center line will bisect and be perpendicular to the line segment connecting the two end points of the most bent curve drawn on the surface. Such an arrangement will reduce the likelihood of the surface boundary been hidden from the views of the cameras. The other method is to move the stereo vision

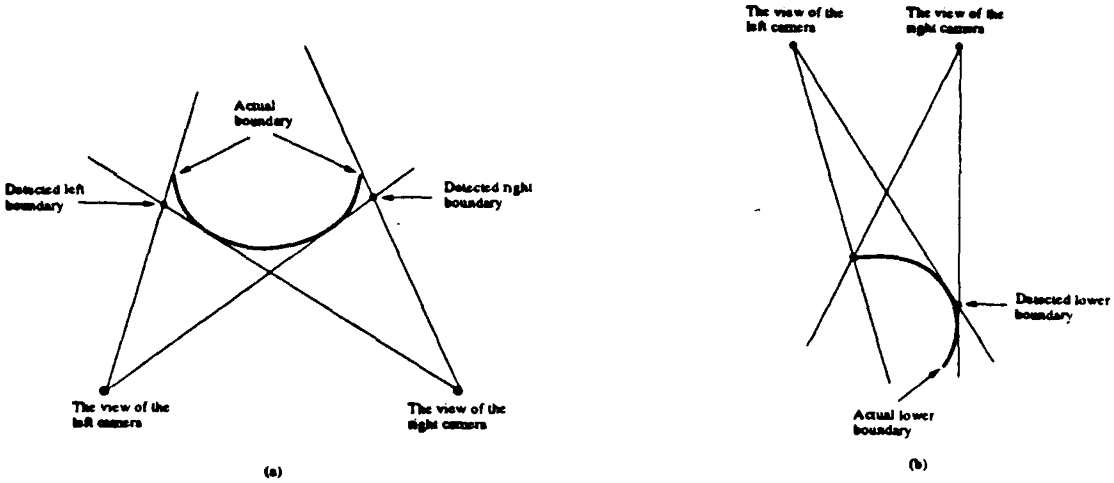
Actual boundary
Detected left boundary
Detected right boundary
The view of the left camera
The view of the right camera
(a)
The view of the left camera
The view of the right camera
Detected lower boundary
Actual lower boundary
(b)

Fig. 1 Two examples of the false-boundary problem in stereo vision

sensor farther away from the surface. In this way, the view angle of the camera formed by the curved surface will decrease and may eliminate the false boundary problem. These two approaches are illustrated in Fig. 2 and Fig. 3 respectively.

The above two approaches can reduce the likelihood of the false boundary problem, but cannot eliminate the false boundary problem. The passive stereo vision method must cooperate with active stereo vision and dynamic sensing to totally eliminate the false boundary problem.

2.2 Matching Criteria in Active Stereo Vision

Since the surface of a deformed plate is smooth, it is necessary to use active vision to detect the 3-D shape of the surface. For active stereo vision, structured light with certain patterns must be used. We choose to use an array of squares as shown in Fig. 4 to be the light pattern. The corners of the squares are used as matching point for deriving the data points in the 3-D space. Squares are chosen because they are simple and provide more matching points than other simple features such as circles and triangles.

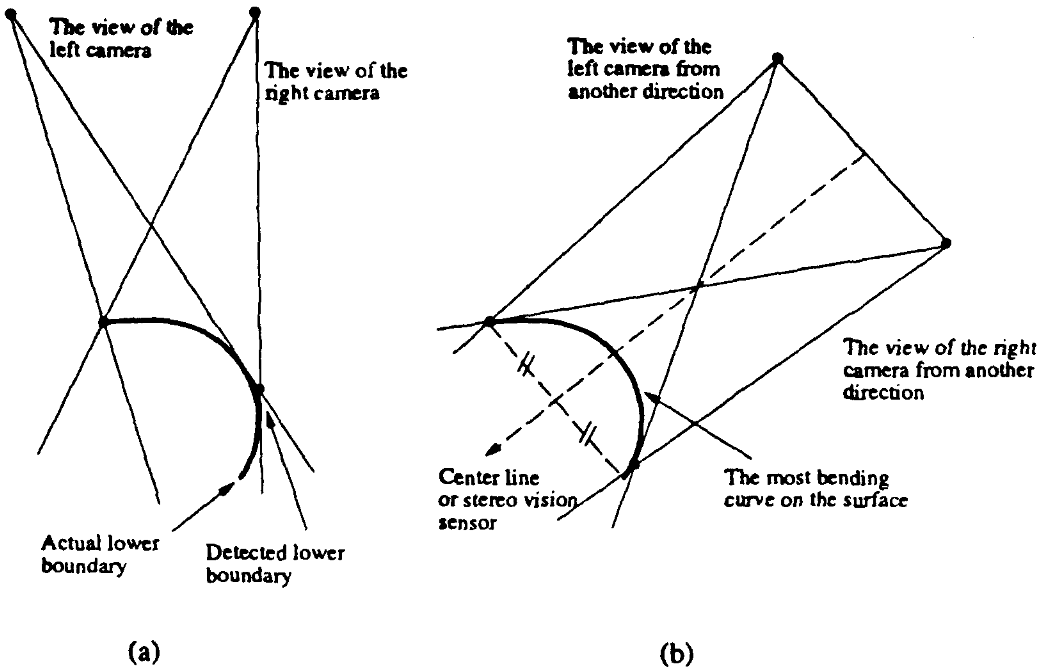
The view of the left camera
The view of the right camera
Actual lower boundary
Detected lower boundary
(a)
The view of the left camera from another direction
The view of the right camera from another direction
Center line or stereo vision sensor
The most bending curve on the surface
(b)

Fig. 2: (a) The false boundary problem occurs.
(b) The center line of the stereo vision sensor is bisecting and perpendicular to the line segment to reduce the likelihood of the false-boundary problem.

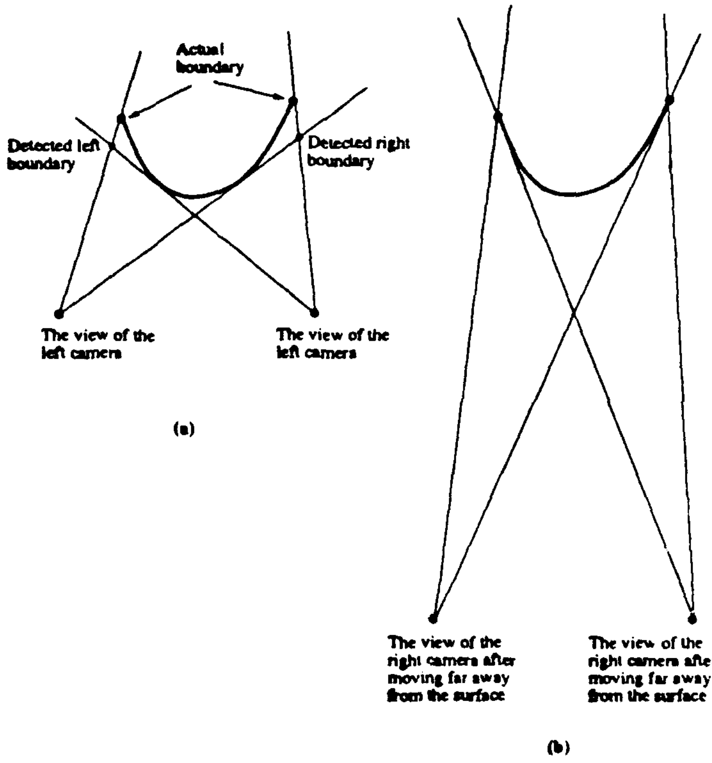
Actual boundary
Detected left boundary
Detected right boundary
The view of the left camera
The view of the left camera
(a)
The view of the right camera after moving far away from the surface
The view of the right camera after moving far away from the surface
(b)

Fig. 3: (a) The false-boundary problem occurs. (b) The vision sensor is moved farther away from the surface to reduce the likelihood of the false boundary problem.

The key problem in active stereo vision is the matching of the squares in the image pair. The matching criteria that we use can be explained by Fig. 5. An arbitrary surface is assumed to be flat and parallel to the image planes of the cameras (imaginary flat surface in Fig. 5). An imaginary plane, named "structured light plane", is defined as the intersection of the structured light and an arbitrary plane perpendicular to the center ray of the structured light. The center ray of the structured light is oriented parallel to the optical axes of the cameras while the structured light is oriented parallel to the optical axes of the cameras. The created matching squares on the structured light plane will then lie parallel to the x and y axes of the structured light plane.

The uniqueness constraint and continuity constraint identified by Marr and Poggio [1] can be used for matching the squares in the case defined above. According to the uniqueness constraint, there will be only one square in the images of the cameras corresponding to one square on the flat surface. According to the continuity constraint, adjacent squares in the image will be projected from adjacent squares on the flat surface. With the use of uniqueness and continuity constraints, each square in the horizontal array in the image pair can be matched according to their relative positions in the x direction. The above description defines the matching criteria.

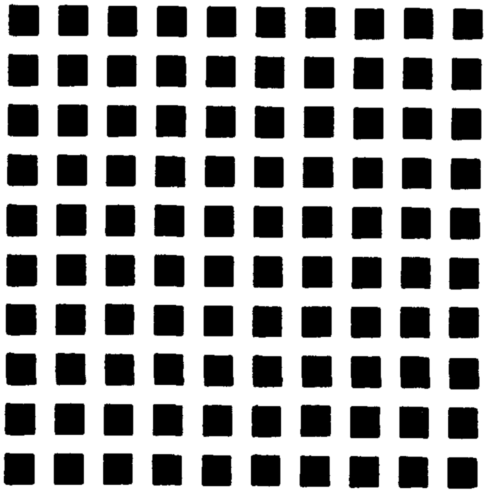

Fig. 4 The patterns of the structured light in active stereo vision

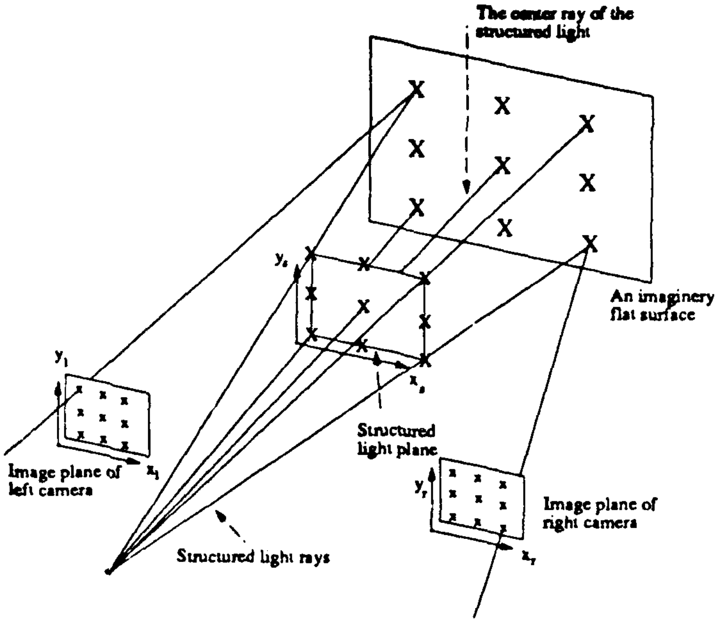
The center ray of the structured light
An imaginery flat surface
y_s
x_s
y_l
x_l
Image plane of left camera
Structured light plane
y_r
x_r
Image plane of right camera
Structured light rays

Fig. 5 The explanation of the matching criteria in active stereo vision

In reality, a deformed plate may have a curved surface. As a result, the positions of the squares in the image pair will be shifted from their positions projected in the flat surface case. This, however, will not cause any problems in feature matching. The space between two adjacent squares in the x direction can be adjusted to be *sufficiently small such that* two adjacent squares in the structured light plane will be projected to the image pairs as two adjacent squares in the x direction. Furthermore, the space between two adjacent horizontal square arrays in the projection plane can be designed sufficiently large such that two squares from two adjacent horizontal square arrays will never be projected as two adjacent squares in the image pairs. The above two spacing criteria are further explained in Fig. 6. Apparently, the space between the adjacent squares must be selected in accordance with the maximum curvature of the deformed plates.

2.3 Dynamic Sensing Process

Based on the passive-active stereo vision mechanism discussed above, the dynamic sensing process for detecting the shape of the curved/smooth surface include three stages.

In the first stage, passive stereo vision is applied to obtain a rough boundary of the surface. The detected boundary may not be the real boundary of the surface because of the false boundary problem. The rough boundary detected in this stage will define a boundary plane. The boundary plane is defined to be the best-fit plane of the detected boundary. That is, the overall distance from the detected boundary to the boundary plane is at minimum. The boundary plane will guide the movement of the cameras in the second stage.

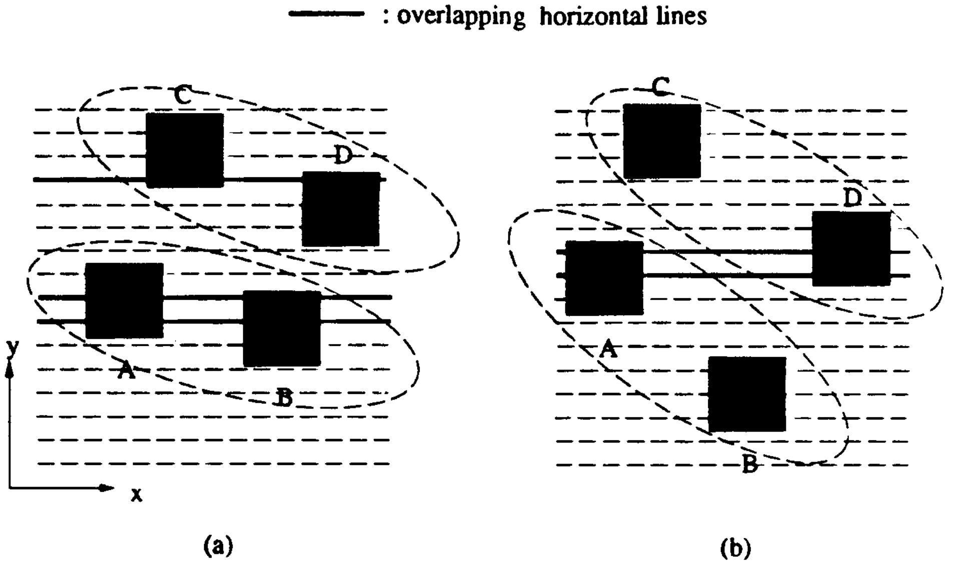

Fig. 6 In (a) and (b), squares A and B are projected from the same horizontal square array, and C and D are projected from another horizontal square array. A and D should not be interpreted as on the same horizontal array and should be avoided.

In the second stage of the sensing process, the cameras will be moved to a closer position to the surface so that the distance between the cameras and the surface will be within the effective focal length of the cameras. In addition, the image planes are oriented parallel to the boundary plane found in the first stage. The boundary detected by passive vision in this stage reduces the likelihood of the false boundary problem and will define the area where active stereo vision should be applied.

In the third stage of the sensing process, without moving the cameras, the projector moves to a proper position and orientation to project the structured light on the surface. The images of the surface are acquired by the two cameras. The created matching squares within the surface boundary in the image can be extracted. The existence of the false boundary problem can be detected by comparing the number of squares extracted in the image pairs to the actual number of squares within the square boundary. If the two numbers are different, the false boundary problem is detected. The cameras should be moved farther away from the surface to see the real boundary.

After the false boundary problem is totally avoided, the corners of the squares in the image pair can be used as the matching points for deriving the data point of the surface.

The sensing process as described above has been confirmed by experiments done in our laboratory. A PUMA robot was used to carry the stereo vision system, and another PUMA robot was used to carry the projector. The results of the experiments proves that the proposed passive-active stereo vision is effective for detecting the shape of the smooth surface of deformed plates.

3. ERROR ANALYSIS ON THE NON-CONTACT 3-D DIGITIZING SYSTEM

In recent years, computer controlled digitizing systems such as coordinated measuring machines (CMM) have become very popular for measuring a complex sculptured surface. Traditional digitizing systems use a touch probe to measure individual points on the surface. This is a slow process since the probe has to make contact with the surface many times. We have proposed to use Laser Displacement Sensors (LDS) to replace the touch probe. The LDS can digitize an unknown surface without any contact. As a result, the speed of measurement can be increased.

However, the LDS has certain limitations. First, the effective stand off distance of a LDS is limited, and secondly, the laser beam must be oriented perpendicular to the object surface. If these two limitations are violated, either the LDS fails to give a measurement or the measurement given is not precise. Since the surface is unknown, it is difficult to keep the LDS from violating the two limitations. We have developed an active sensing concept. The idea is to install the LDS on an articulate CMM so that the position and orientation of the LDS can be actively adjusted. For adjusting the CMM, we have developed two methods to predict the variation of the surface. They are the Multiple Beam Approach and the Extrapolation Approach. The concepts of these two approaches are described in the previous semi-annual report (the fourth semi-annual report). For convenience, they are briefly discussed here again.

The multiple beam approach uses three LDS to measure the curvature and tangent of an unknown surface. As a result, the LDS can locally follow surface variations although the global shape of the surface is not known. The n^{th} order polynomial extrapolator, on the other hand, is the process of extrapolating a continuous function between the present sampling instants and the next sampling instant. The polynomial has the following standard form:

$$z(x) = a_n x^n + a_{n-1} x^{n-1} + \ldots + a_1 x + a_0 \qquad (1)$$

The n+1 unknown coefficients in the polynomial are solved for by using the previous n+1 data points. Once all the coefficients are solved, the next sampling point can be predicated by using this same polynomial.

Over the past six months, we have further evaluated the two digitizing approaches by analyzing the error parameters associate with the digitizing process. There are three error parameters associated with the digitizing process: ρ, θ and Δs. The first two error parameters, ρ and θ, are a result of limitations associated with the LDS. ρ is the displacement between the LDS's reference position and the object's surface. θ is the angle between the laser beam and the surface normal vector (Fig. 7).

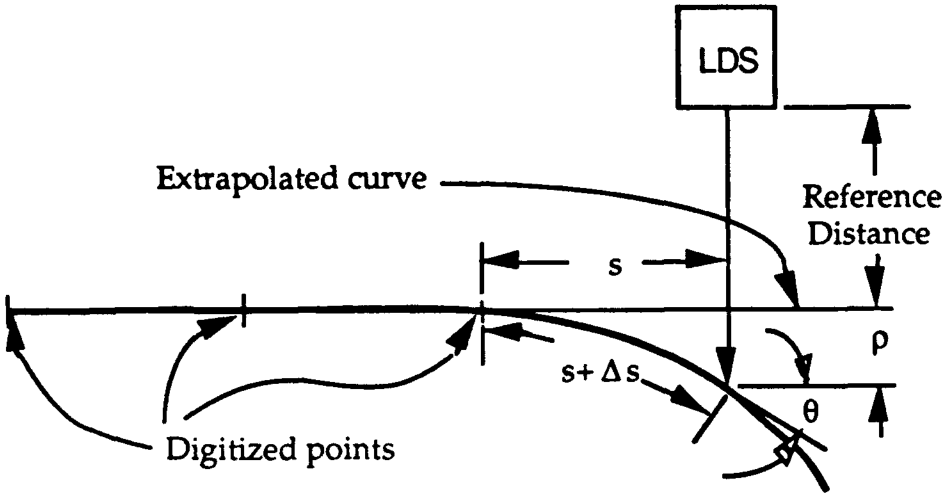

Fig. 7 Digitizing error parameters

In order to have a precise measurement, ρ and θ must be bounded within the manufacturer's specifications. The last parameters, Δs, is related to the sampling arc length. It is the difference between the desired sampling arc length, s, and the actual arc length, $s+\Delta s$, as measured between adjacent digitized points. Our study evaluates the bounds on the three parameters as a result of using the two digitizing approaches.

The bounds on these error parameters are developed through three steps. In the first step, we prove that the next sampling point is within a bounded area if the sampling arc length s is bounded and the maximum curvature of the surface is finite. In the second step, we prove that within the bounded area defined in the first step, any sampling point will have a bounded maximum slope and a bounded minimum slope. In the third step, based on the worst case conditions, we derive the error parameters as functions of the ratio between the sampling arc length and radius of maximum curvature. These three steps are now presented in greater detail.

A. A Plane Curve with Finite Maximum Curvature is Bounded Locally

In the two digitizing approaches, the surface is digitized one row at a time where the rows are formed by the intersection of parallel planes with the surface. The intersection of a plane with the surface forms a plane curve. We have shown that a plane curve which is known to have a finite maximum curvature, κ_m, and to pass through the point P_o, with a tangent vector, T_o, is bounded locally by two tangent circles with radii, R, where $R = 1/\kappa_m$ (Fig. 8). A sufficient condition for this locality is $|s| \leq (\pi/2)\,R$ where s is the curve's arc length measured from the point P_o. The curve will not cross into these tangent circles as long as the arc length satisfies this condition. The shaded area in Fig. 8 highlights the locally bounded region of the next sampling point.

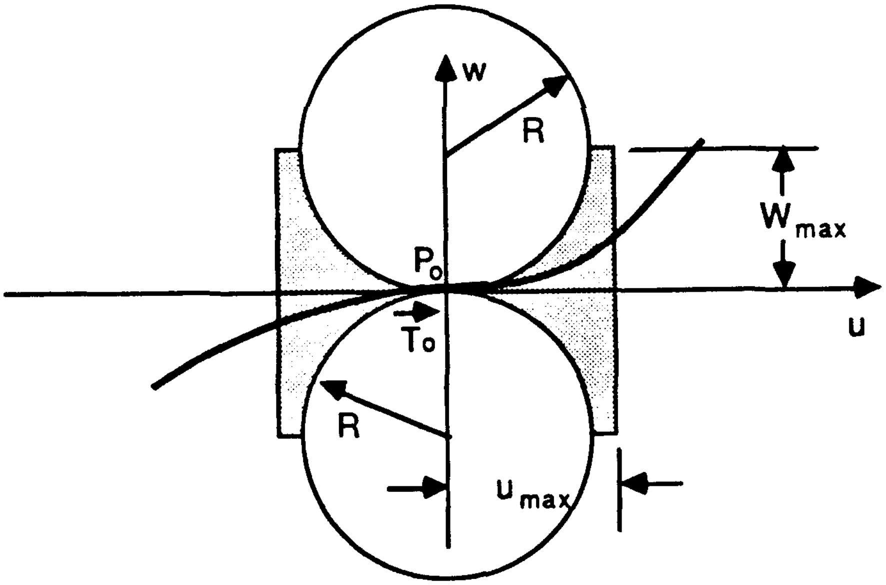

Fig. 8 Locally bounded region

B. A Curve's Slope is Bounded in the Locally Bounded Region

Suppose the following four things are known about a plane curve: 1) It has a finite maximum curvature, 2) It passes through the point P_o, 3) It has a known tangent vector, T_o, at the point P_o, and 4) It passes through the point P_2 where P_2 is located in the locally bounded region defined above. With these constraints, the slope of the curve at the point P_2 is bounded by the maximum and minimum slopes m_l and m_s respectively (Fig. 9).

To determine the worst possible orientation that the plane curve might have with the LDS's beam, maximum and minimum slope values need to be determined for points along a line which extends across the locally bounded region. This line represents the LED's beam, and it intersects the origin of the lower tangent circle while forming an angle, γ, with the w axis as shown in (Fig. 10). Clearly, if the plane curve follows the top tangent circle, the angle between the laser beam and the normal vector of the plane curve will be the largest. The other error parameters are also maximized under these conditions.

C. Deriving Error Parameter Functions

Based on the worst prediction conditions as defined in **A** and **B**, we derived error parameters as functions of the ratio of sampling arc length to radius of maximum curvature. These functions are respectively written as:

$$\frac{\Delta s}{R} = -\frac{s}{R} + \sin^{-1}\left\{\sin\left(\frac{2s}{R}\right) - \sin\left(\frac{s}{R}\right)\sqrt{2\cos\left(\frac{2s}{R}\right)-1}\right\}, \tag{2}$$

$$\frac{\rho}{R} = 2\cos\left(\frac{s}{R}\right) - 1 - \sqrt{2\cos\left(\frac{2s}{R}\right)-1} \tag{3}$$

and

$$\theta = \frac{s}{R} + \sin^{-1}\left\{\sin\left(\frac{2s}{R}\right) - \sin\left(\frac{s}{R}\right)\sqrt{2\cos\left(\frac{2s}{R}\right)-1}\right\}. \tag{4}$$

From the above three equations, the error parameters are shown to be monotonically increasing functions of the ratio of the sampling arc length to radius of maximum curvature. By using these equations, we can determine what the sampling arc length should be given the limitations on the sampling errors.

4. RESEARCH ACTIVITIES FOR THE NEXT PERIOD

In the next period, we plan to investigate and complete the following two topics:

a. Graduate student Rached Zantout has been studying the deformation of two dimensional objects since the beginning of this year. He is currently investigating how to identify the deformation characteristics of a two dimensional plate. This investigation contains two steps:

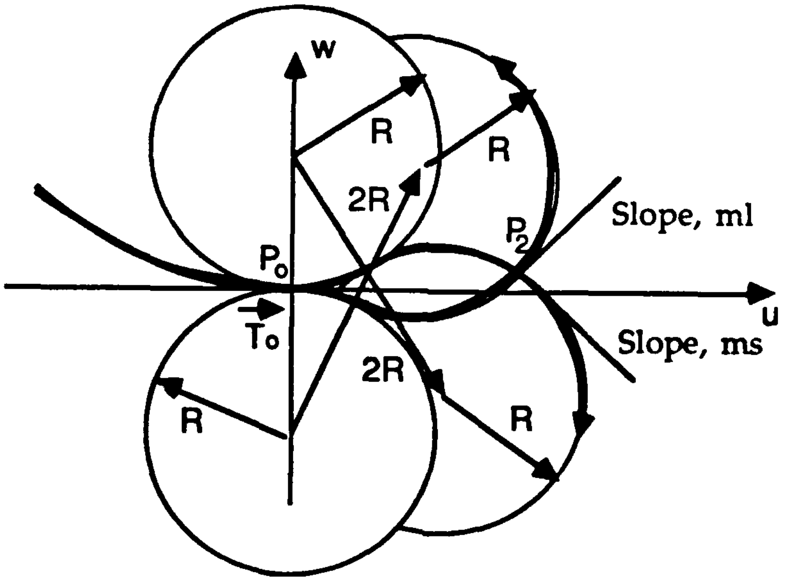
w
R
R
2R
Slope, ml
P2
Po
u
To
Slope, ms
2R
R
R

Fig. 9 Bound on local slope values

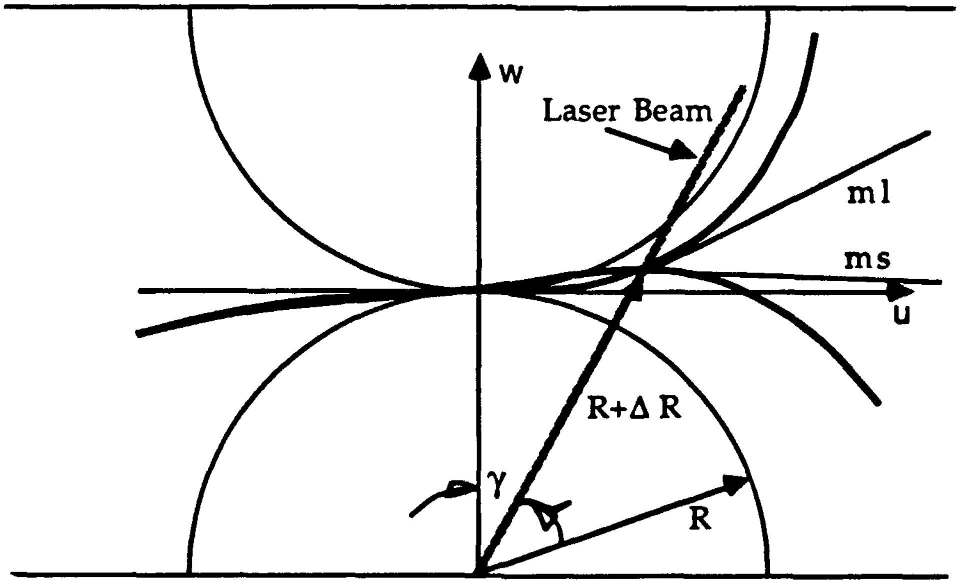
w
Laser Beam
ml
ms
u
R+Δ R
γ
R

Fig. 10 Extreme LDS beam orientation

(1) identifying the deformation of a plate under external loads, and (2) calculating the parameters which governs the deformation behavior of the plates. A geodesic approach is being used to measure the deformation, and a Finite Element Method (FEM) is being used to determine the deformation characteristics. We expect that this study can be completed by the end of the next period.

b. A new approach for surface representation of a deformed plate. Last year, we developed a new approach, based on energy minimization and Coon's patches, to represent the surface of a deformed plate. Recently, we have found another new approach which may be more convenient than the previous approach. This new approach is based on the perturbation technique. By using the perturbation technique, the number of patches used to represent a surface can be significantly reduced.

The results of the above research activities will be presented in the next semi-annual report.

REFERENCES

1. D. Marr and T. Poggio, "Cooperative computation of stereo disparity," *Science*, vol. 194, pp. 283-287, 1976.

APPENDIX A

Passive and Active Stereo Vision For Smooth Surface Detection of Deformed Plates[1]

Chichyang Chen and Yuan F. Zheng

Department of Electrical Engineering
The Ohio State University
2015 Neil Avenue
Columbus, OH 43210

Abstract

Passive stereo vision is proposed to work in a complimentary manner with active stereo vision for the detection of smooth surfaces of deformed plates. Passive stereo vision without the projection of structured light is used to obtain the boundary of the smooth surfaces; whereas active stereo vision with the projection of structured light is applied to detect the details of the surfaces. An inherent problem in stereo vision, called false boundary problem, is identified and solved by calibrating the structured light. The matching criteria in active stereo vision and the sensing process of the proposed approach are presented. An experiment was conducted to test the effectiveness of the proposed approach.

---

[1] Acknowledgment: This work is supported by the Office of Naval Research under grant N00014-90-J-1516

I. Introduction

Making the machine "see" an object is one of the most important tasks in machine intelligence, manufacturing automation, and robotics. To enable a machine "see" involves two works: sensor detection to obtain data points of the object and shape representation of the object for the process of object recognition, inspection, and manipulation for the machine. 3-D shape reconstruction of the object is the process of these two works, obtaining data points of 3-D objects and constructing its shape from the sensed data points through interpolation or approximation.

A special case in 3-D shape detection using stereo vision is considered in this paper. We are concerned about how to detect the smooth surfaces of metal plates. This study is stimulated by the observation that metal plates are often used in many applications. For example, in shipbuilding, aerospace, and automobile industries, vehicle bodies are the essential parts of their products. These bodies are usually constructed by assembling together numerous pieces of metal plates. Vision sensor is chosen for shape detection of these parts because of its harmlessness and lower cost compared to other sensors such as laser range scanners.

Stereo vision is an attractive technique for depth perception, which is suitable in almost all application domains [1]. In stereo vision, matching points are first extracted from the stereo image pair by observing the changes of the ambient light reflection or radiation from the object [2]. Depth of the object can then be derived directly by matching these extracted points through triangulation method. Depth sensing using stereo vision does not depend on the projection of active light source. Lighting of the working environment for stereo vision does not need to be well controlled. Hence, stereo vision is useful for more general vision applications [1]. However, the operation of stereo vision relies on the changes of the light reflection or radiation from the object surfaces. For objects made of metal plates, it is difficult to use stereo vision to detect its smooth surface since the smooth surface will not generate matching features in the image pair. This inherent problem prevents stereo vision from being widely used in industrial automation applications where the objects to be detected are smooth.

Active ranging methods by the projection of structured light provide solutions to the inherent problem of stereo vision in detecting smooth surfaces. In essence, ranging methods using structured light are still stereo methods. If only one camera is used, depth of the object can be derived by matching the created features on the surface of the object to the features extracted from the acquired image through triangulation. A typical work using this method can be seen in [3]. Alternatively, a pair of cameras can be used. In such cases, depth of the object is derived by using exactly the same method in stereo vision except that the matching features in the image pair are created by the projection of structured light. By using structured light, it is easier to extract image features from the image pair. Usually, binary images can be generated when the illumination of the working environment is well controlled. Most importantly, the correspondence problem in stereo vision becomes simpler since the pattern of the matching features in the stereo images are more regular following the pattern of the light source [3]. The ranging method using structured light is named "**active stereo vision**". Conversely, conventional stereo vision without the usage of structured light is referred to as "**passive stereo vision**" in this paper.

The correspondence problem does not exist in active stereo vision if a single light beam or a single light plane is used as the light source. Only the brightest spot or curve in the images generated by the light beam or the light plane respectively, need to be detected and matched. As successive scanning will be required to detect the whole surface, sensing process will become slow. If a grid of light is used as the light source, there will be more data points in one single detection, and the matching of the created features in the image pair will become complicated. The matching problem can be solved by imposing unique properties on the stripes of the light. Approaches using colors [4], thickness [5], space encoding [6, 7] have been suggested and implemented. These approaches require special devices (color or thickness detection) and require multiframes (space encoding), and are thus not convenient for implementation. It is easier to generate and detect a uniform grid of light. However, matching the features created by the uniform grid of light is a difficult task. Such a task has been studied by Hu and Stockman. They used constraint propagation to solve such a matching problem in active stereo vision, assuming that the spatial frequency of the surface is less than the stripe frequency [3].

The algorithms provided by Hu and Stockman for matching grid points in the image plane to the grid points in the projection plane are complicated. The complication of their algorithms are mainly caused by the fact that the surfaces of the objects might be occluded in general cases and it is difficult to distinguish x stripes from y stripes in the image plane. Furthermore, due to blooming effects, surface discontinuities, and the difference in the viewing angle of the cameras, some of their topological constraints for matching the grid points may not hold [3]. In consequence, it is difficult to identify the grid point in the projection plane corresponding to a particular grid point in the image plane. Several matchings between the grid points in the image plane and the projection plane can be resulted by applying their algorithms. In order to check which matching combination is the correct one, the deduced surface solution from a particular matching has to be back projected to the projection plane. Their algorithms are therefore time consuming.

In this study, passive stereo vision is proposed to detect the boundary of the surface of the deformed plates. Active stereo vision with the projection of structured light is used to detect the details of the surface. The two cameras and the projector are proposed to be mounted on movable platforms such as robot manipulators. The cameras and the projector can thus be moved to appropriate positions and orientations for easy detection and matching the features created by the projection the smooth surface. Such a *dynamic sensing mechanism* is also necessary for the detection of 3-D objects in 3-D space since the complete description of 3-D objects can only be obtained by sensing the objects from multiple views.

A particular problem in stereo vision has to be considered in applying passive and active stereo vision for the detection of smooth surfaces. When the surface is curved, the actual boundary of the surface may be hidden from the cameras. As a result, the observed boundary from passive stereo vision is not accurate. This problem, named the **"false boundary"** problem in this paper, will also complicates feature matching in active stereo vision.

The viewing direction and position of the stereo vision sensor affects the occurrence of the false boundary problem in stereo vision. Since the extent of the smooth surface is not available, the pose of the stereo vision sensor can hardly be devised to prevent the false boundary problem. The proposed dynamic sensing allows the sensor and the projector be moved to better positions to achieve accurate sensing based on the information obtained from previous sensing, and prevent the false boundary problem.

In order to test the effectiveness of the proposed approach using integration of passive and active stereo vision for the detection of smooth surfaces, an experiment was conducted. A curved rectangular plate is considered as the target for shape detection.

In the following sections, we will first explain the so-called "false-boundary" problem in stereo vision in Section II. Then, the matching criteria for active stereo vision in the case without the occurrence of false boundary problem is described in Section III. The process of dynamic sensing which integrates passive and active stereo vision for detecting smooth surfaces is presented in Section IV. The experiment is described in Section V. Conclusions and some discussions are given at the end of this paper.

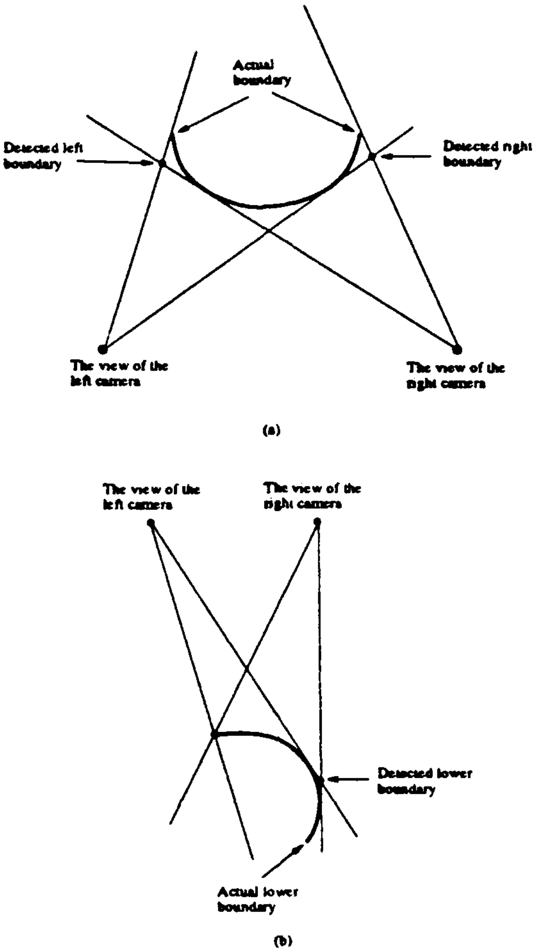
Actual boundary
Detected left boundary
Detected right boundary
The view of the left camera
The view of the right camera
(a)
The view of the left camera
The view of the right camera
Detected lower boundary
Actual lower boundary
(b)

Figure 1: Two examples of the false-boundary problem in stereo vision.

II. False-Boundary Problem in Stereo Vision

When a curved surface is seen by the two cameras of the stereo vision sensor, the boundary of the surface detected in each camera might not correspond to the actual boundary of the surface. As a result, the boundary of the surface recovered from matching these two "false boundaries" in the two cameras by triangulation will be incorrect. Shown in Fig. 1 are two examples of this problem. In (a) of Fig. 1, the right side of the surface boundary is hidden from the left camera and the left side of

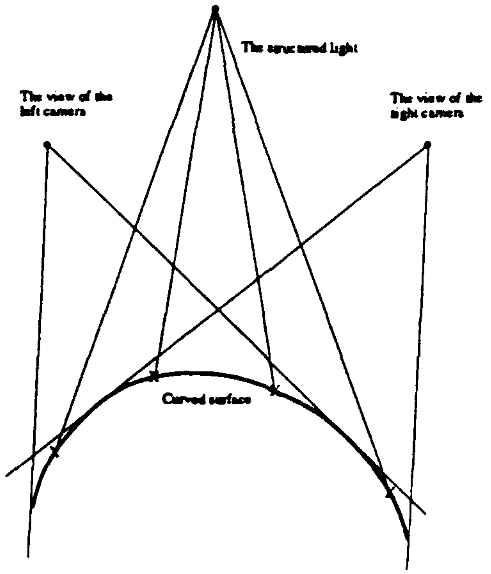

Figure 2: A mismatch of the created features on the surface. The "x" symbols stand for the created features.

the surface boundary is hidden from the right camera. In (b) of Fig. 1, the lower side of the surface boundary is hidden from the two cameras.

The false-boundary problem also affects the correctness of feature matching in active stereo vision. Fig. 2 shows an example of feature mismatching in active stereo vision. In Fig. 2, four features are created by the structured light on the surface. However, each camera can only see three of the four created features. If the three features in the image pair of the stereo vision are matched to one another, the recovered depth corresponding to the features on the surface will be incorrect.

There are two ways to eliminate the occurrence of the false boundary problem in stereo vision. One is to orient the center line of the stereo vision sensor in order that the center line will bisect and be perpendicular to the line segment connecting the two end points of the most bending curve drawn on the surface. Such arrangement of the center line will reduce the likelihood that the surface boundary is hidden from the views of the cameras. The other is to move the stereo vision sensor farther away

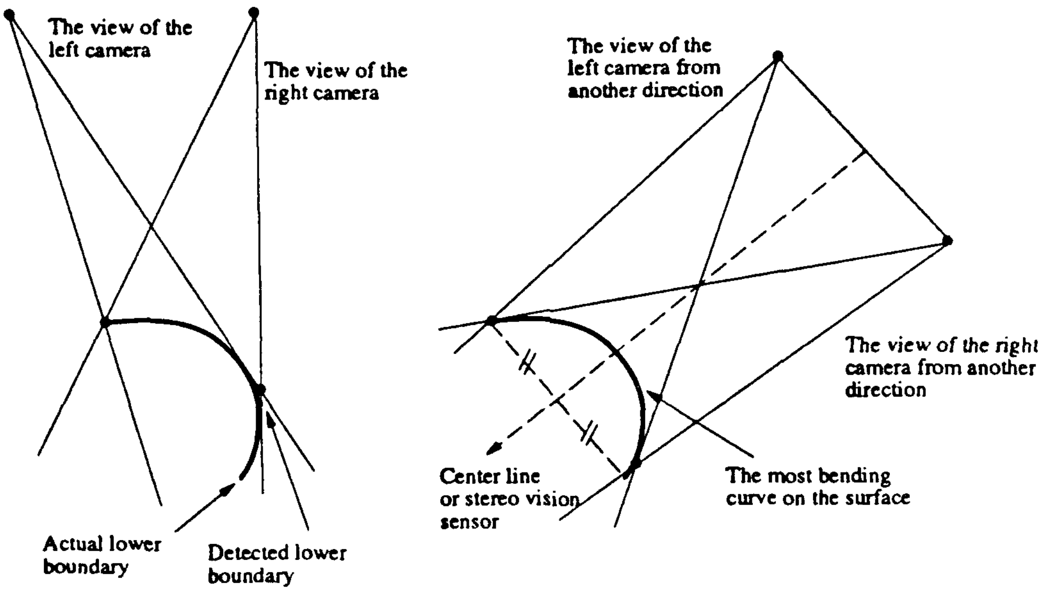
The view of the left camera
The view of the right camera
Actual lower boundary
Detected lower boundary
The view of the left camera from another direction
The view of the right camera from another direction
Center line or stereo vision sensor
The most bending curve on the surface

(a) (b)

Figure 3: (a) The false boundary problem occurs. (b) The center line of the stereo *vision sensor is bisecting and perpendicular* to the line segment connecting the two end points of the most bending curve on the surface. The false boundary problem may be eliminated.

from the surface. In this way, the view angle of the cameras formed by the curved surface will be decreased and may eliminate the false boundary problem. These two approaches are illustrated in Fig. 3 and 4, respectively. However, if the surface is so curved that the projection of its actual boundary in the image plane is within the projection of its apparent boundary, as shown in Fig. 5, the false boundary problem can not be resolved by these two approaches. In such a case, it is necessary to detect the surface from multiple views of the stereo vision sensors. The latter case will not be emphasized in this study. The approaches developed in this paper, however, can be easily extended and become applicable to the case. We only need to apply the approach several times from different directions of the stereo vision sensor.

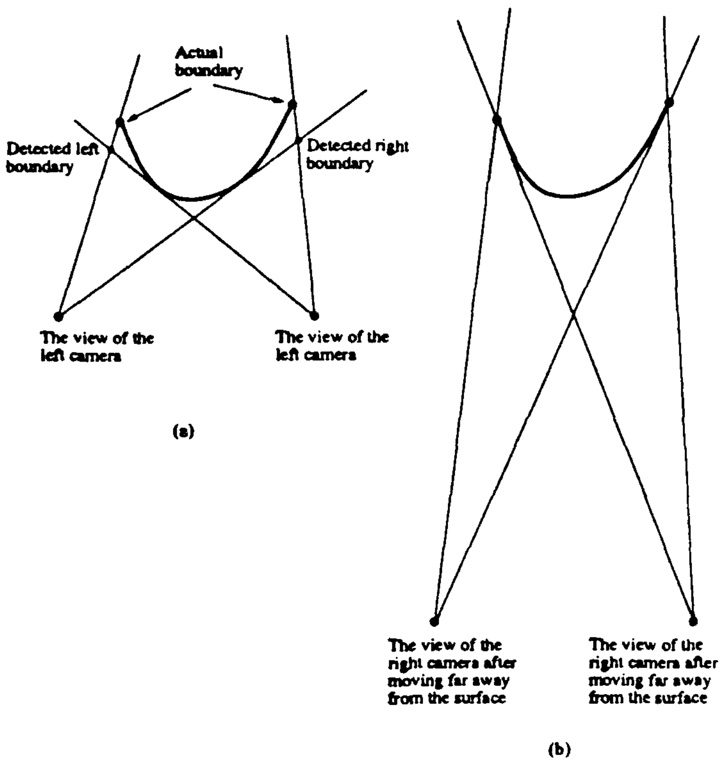
Actual boundary
Detected left boundary
Detected right boundary
The view of the left camera
The view of the left camera
(a)
The view of the right camera after moving far away from the surface
The view of the right camera after moving far away from the surface
(b)

Figure 4: (a) The false boundary problem occurs. (b) The stereo vision sensor is moved farther away from the surface to prevent the false boundary problem.

III. Matching Criteria in Active Stereo Vision

In this section, we discuss the criteria for matching the features in the image pair in the case where the false boundary problem does not exist. The features created by the structured light are chosen to be an array of squares, as shown in Fig. 6. The corners of the squares can be used as matching points for deriving the data points in 3-D space. Squares are chosen because they provide more matching points than other simple features such as circles and triangles. The detection of the corners of squares is more reliable than that of more complicated features such as pentagons and hexagons. In the case that the detection of the corners is not accurate when the

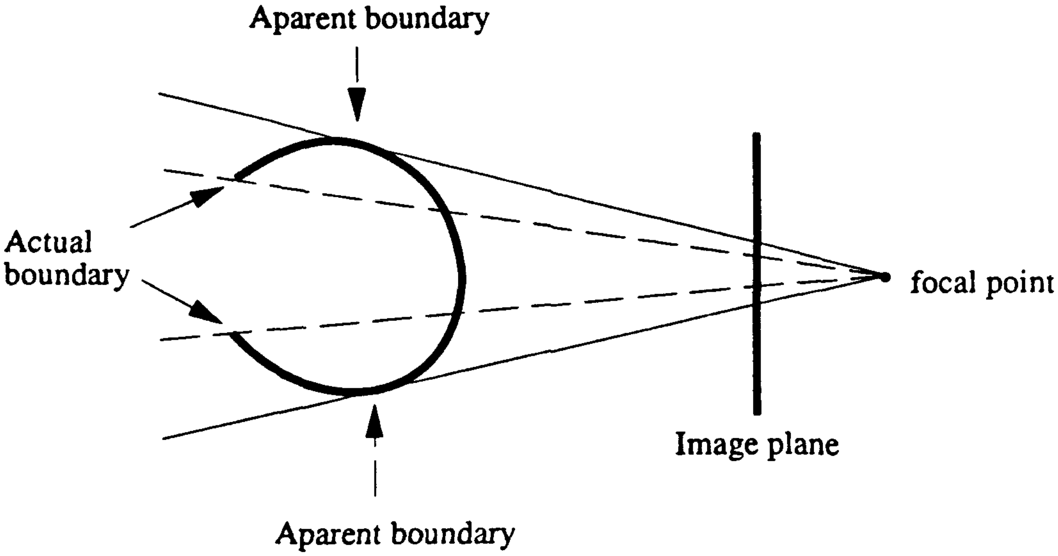

Figure 5: A case when the surface has to be detected from multiple views.

lighting is not well controlled, the geometric centers of the features should be chosen as the matching points. In such cases, simpler features are preferred. Considering the convenience for solving the correspondence problem, we chose the conventional imaging geometry for the use of stereo vision. Such geometry involves a pair of cameras, with their optical axes and image planes mutually parallel and separated by a horizontal distance denoted as the stereo baseline.

Fig. 7 shows an illustration of the case well defined to help explain the matching criteria in active stereo vision. A surface is assumed to be flat and parallel to the image planes of the cameras. An imaginary plane, named **"structured light plane"** in this paper, is defined as the intersection of the structured light and an arbitrary plane perpendicular to the center ray of the structured light. The center ray of the structured light is oriented parallel to the optical axes of the cameras, while the structured light plane is oriented parallel to the image planes of the cameras. The created matching squares on the structured light plane will then lie parallel to the

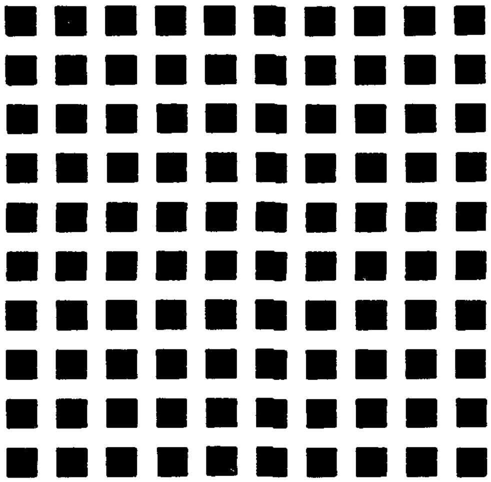

Figure 6: The features to be created by the structured light in active stereo vision.

x and y axes of the structured light plane. The orientation of the matching squares is chosen the same as that of the structured light plane. For the convenience of the following discussion, we denote each row of squares positioned in the structured light plane as a **"horizontal square array"** in the structured light plane. In the image plane, the squares projected from a horizontal square array in the structured light plane are referred to as **"horizontal square array"** in the image plane.

The uniqueness constraint and continuity constraint identified by Marr and Poggio [8] can be utilized for matching the squares in such a well defined case. According to the uniqueness constraint, there will be only one square in the images of the cameras corresponding to one square on the flat surface. Adjacent squares in the image will be projected from adjacent squares on the flat surface if continuity constraint is imposed. With the use of epipolar constraint, the squares in horizontal square arrays in the image planes can be matched according to their y coordinates in the image planes. With the use of the uniqueness and continuity constraints, each square in the horizontal square array in the image pair can be matched according to their relative positions in the x direction. The matching criteria described above is not

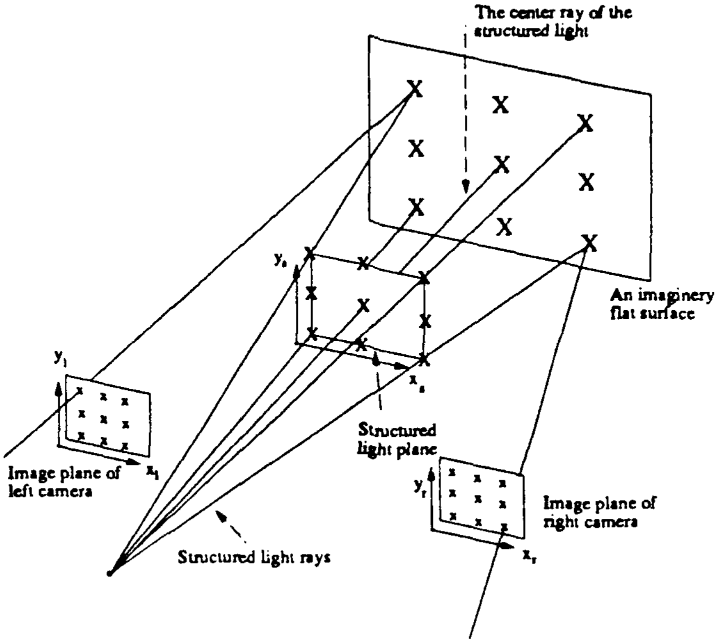
The center ray of the structured light
An imaginery flat surface
y_s
x_s
Structured light plane
y_l
x_l
Image plane of left camera
y_r
x_r
Image plane of right camera
Structured light rays

Figure 7: A well defined case for explaining the matching criteria in active stereo vision. Symbols "x" stand for the matching squares.

restricted to the case of rectangular surfaces shown in Fig. 7. In cases that the surface is not rectangular, the numbers of squares in the horizontal square arrays will not be the same. The matching criteria described above are still applicable to these non-rectangular cases.

In reality, a deformed plate may have a curved surface. As a result, the positions of the squares in the image pair will be shifted from their positions projected in the well defined case. However, shown in the image pair, the relative positions in the x direction of the squares projected from a horizontal square array in the structured light plane are preserved. Similarly, the relative positions in the y direction of the horizontal square arrays are also preserved. Since the spacing between adjacent squares in the x direction in the structured light can be designed to be sufficiently small, we can assure that two adjacent squares in the x direction in the structured light plane will be projected to the image plane as two adjacent squares in the x direction with their

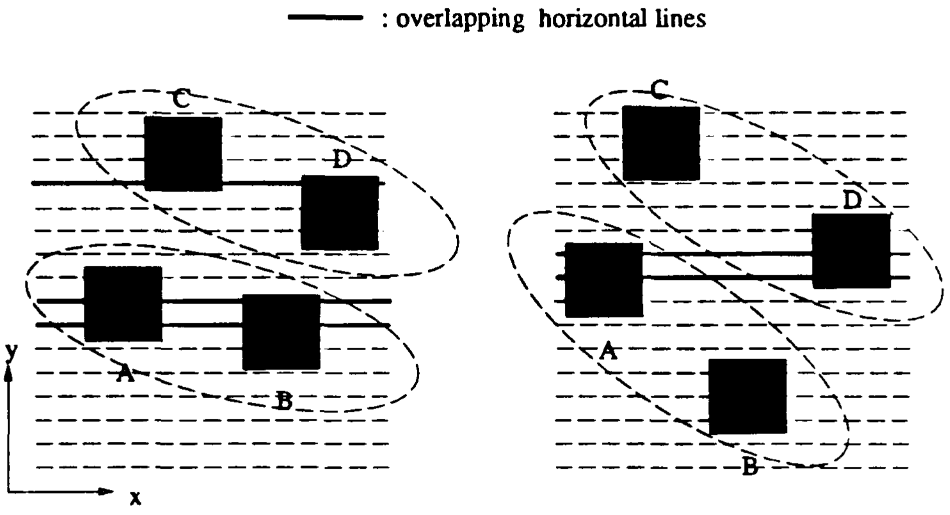

(a) (b)

Figure 8: (a) A required projection of two "horizontal square arrays" in the structured light plane to the image plane. (b) A projection that should be avoided. In (a) and (b), squares A and B are projected from the same horizontal square array, and squares C and D are projected from another horizontal square array.

y coordinates overlapping. Furthermore, the spacing between two adjacent horizontal square arrays in the projection plane can be designed sufficiently large in order that a square in the image plane projected from a particular "horizontal square array" in the structured light plane will be adjacent to squares projected from the same horizontal square array in the structured light plane. These two conditions are explained in Fig. 8.

Based on the above description about the positional arrangement of the matching squares in the image pair of stereo vision, matching of the squares can be stated as follows. First, the squares in each image are sorted into groups, corresponding to the horizontal square arrays in the structured light plane. The sorting of the squares can be performed by applying the following algorithm to the image pair:

1. Start from an arbitrary square extracted from the image. Denote this square as the current square.

2. Search the square in the image that is left adjacent to the current square. If searched, link it to the left of the current square and denote it as the left square.

3. If the left square is found, search the square that is left adjacent to the left square, link the square to the left of the left square, and denote it as the new left square. Repeat this step until there is no square that is left adjacent to the left square.

4. Search the square in the image that is right adjacent to the current square. If searched, link it to the right of the current square and denote it as the right square.

5. If the right square is found, search the square that is right adjacent to the right square, link the square to the right of the right square, and denote it as the new right square. Repeat this step until there is no square that is right adjacent to the right square.

6. Choose an arbitrary square from the squares that have not been linked to other squares. Denote it as the new current square.

7. Repeat step 2 to step 6 until there is no more square left in the image.

After the squares are sorted, groups in the image pair can be matched according to the y coordinate of their leftmost squares. Each square of a matched group in the image pair can be matched according to their relative positions in the x direction.

Based on the above description, the conditions that will ensure successful feature matching are summarized as follows.

1. First, the projector should be oriented in such a way that the center ray of the structured light is parallel to the optical axes of the cameras and the structured light plane is parallel to the image planes of the cameras (Fig. 7).

2. Second, according to the matching criteria, it is required that the regions where the squares are to be matched be defined. The regions can be defined by detecting the surface boundary in the image pair.

3. Third, the two conditions shown in Fig. 8 regarding the relation of the squares in the image planes should be satisfied. To ensure these two conditions the spacing between adjacent squares in the x direction in the structured light plane should be designed sufficiently small and the spacing between adjacent horizontal square arrays should be designed sufficiently large. However, it is not always easy to estimate the required spacing between two adjacent squares in the structured light. To further ensure these two conditions, the structured light plane and the image planes should be oriented perpendicular to the normal vector of the **boundary plane**. The boundary plane is defined to be the best-fit plane of the detected boundary. That is, the overall distance from the detected boundary to the boundary plane is minimum. Mathematically, the boundary plane should minimize the following integral:

   $$\oint D(s)ds,$$

   where $D(s)$ is the distance from a point s on the boundary to the plane. The result of this arrangement is that the average normal vector of the surface is more likely to be in the same direction as the optical axes of the cameras and the disparity in the y direction of adjacent squares in the image planes is decreased. In consequence, the likelihood of the false boundary problem as shown in Fig. 1 and the mismatch problem as shown in Fig. 8(b) is reduced. Mathematical proof of this advantage is out of the scope of this paper and will not be discussed here.

A special case should be considered in identifying the matching squares in the image planes. In the case that the squares are projected from the structured light on the boundary of the surface, the squares in the image pair will be greatly distorted. Their shapes could become triangular, quadrilateral, pentagonal, etc. and their size will become smaller. A criterion is needed to treat these "partial" squares as either matching features or as noisy features. The design of such a criterion should be based on how robust the image processing is used to extract the features.

IV. Sensing Process

Two kinds of calibration must be performed to ensure that the stereo vision sensors and the projector can be applied to detect the curved surface in dynamic and exploratory sensing. One is the robotic hand/eye calibration of the stereo vision sensors mounted on the robot arm. The hand/eye calibration is to obtain the relative position and orientation between the robot hand and the cameras. As a result, the images of the cameras can be used to precisely measure the position of a target. The other is the structured light calibration, designed to obtain the equations that describe the structured light in the coordinate system of the robot arm holding the projector. Based on the results of the structured light calibration, the position and orientation of each structured light ray generating the matching squares on the structured light plane can be derived in the coordinate system of the robot arm holding the projector. The structured light calibration can be performed by using the same method for the hand/eye calibration of the stereo vision sensors. A simple calibration method is provided in another paper [9] and will not be further addressed here.

The structured light calibration serves two purposes. During the process of active stereo vision sensing, the structured light should be oriented to the desired positions and orientations as described in Section III to ensure successful feature matching. The other purpose of the structured light calibration is to help detect the false boundary problem in stereo vision, which will be explained later in this section. The process of dynamic sensing for detecting the shape of the curved/smooth surfaces including three basic stages is described in the following.

In the first stage, passive stereo vision is applied to obtain a rough boundary of the surface. In the literature, there are many approaches proposed to solve the matching problem in passive stereo vision. Matching algorithms based on edges [10], areas [11], segments [12], curves [13], structural descriptions of image primitives [14], and regions [15] are often mentioned and used [16]. However, passive stereo vision is not the emphasis of this research. We consider a specific working environment that will simplify the implementation of passive stereo vision, instead of a general environment considered in these approaches. The working environment is assumed to be dark with light illuminated from the top to the black ground. As a result, it will be easy to extract and recognize the boundary of the targeted surface in each image of stereo vision. However, the detected boundary of the surface may not be accurate because the false-boundary problem might occur and the surface can be out of the range of the effective focal length of the cameras. Such a rough boundary detected in this stage provides guidance for the movement of the cameras in the second stage of sensing.

In the second stage of the sensing process, the vision sensor will be moved to a closer position to the surface so that the distance between the cameras and the surface will be within the effective focal length of the cameras. In addition, the image planes are oriented as perpendicular to the boundary plane as described in condition three in Section III. The surface boundary is detected more accurate by applying passive stereo vision again. The boundary detected by passive stereo vision in this stage will define the area where active stereo vision should be applied.

In the third stage of the sensing process, without moving the cameras, the projector is moved to a proper position and orientation in order that it can project the structured light on the surface and satisfy the conditions stated in the previous section. The images of the surface are acquired by the two cameras. The created matching squares within the surface boundary in the images can be extracted. The squares can be mismatched due to the false boundary problem as explained in Section II. The existence of the false boundary problem can be detected by comparing the number of squares extracted in the image pair to the actual number of squares within the surface boundary. If the number of the squares within the surface boundary is larger than that in either of the two images, the false boundary problem exists. The actual number of squares within the surface boundary can be known by checking how many structured light rays are projected within the surface boundary since the position and orientation of the structured light rays are all known. If the false boundary problem is detected, the cameras can be moved far enough away from the surface to view the real boundary as shown in Fig. 4.

After the squares in the image pair are matched, either the corners or the centers of the squares in the image pair can be chosen as the match points for deriving the data points of the surface. The data points of the surface can be chosen as the points in space that minimize the sum of their distance from each of the back-projection lines which correspond to the match points in the image pair.

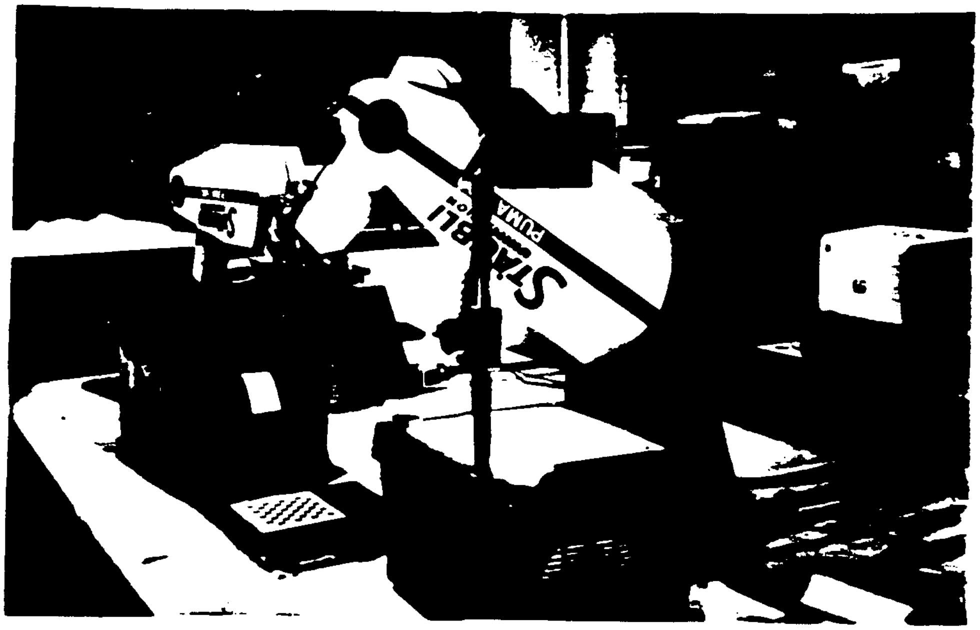

Figure 9: The setup for the experiment in reconstructing the shape of a plate.

V. Shape Detection of a Deformed Plate

In order to illustrate the proposed approach to smooth surface detection, integration of passive and active stereo vision, an experiment was conducted to detect the shape of a deformed plate. The procedure and the results of the experiment are described in this section.

A. The Setup of the Experiment

Shown in Fig. 9 is the picture of the setup of the experiment. The target for this experiment is a rectangular plate with 11.65 cm in length and 7.35 cm in width. The plate has a bright white color and is bent by 10° such that a curved surface is formed. A dark background is chosen. Such a design of the working environment simplifies the image processing for the passive and active stereo vision. An overhead

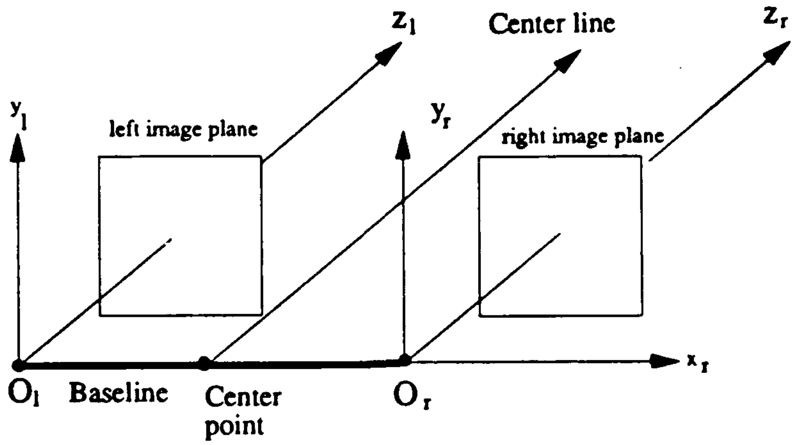

Figure 10: The structure of a stereo vision sensor with conventional imaging geometry.

projector is used to project structured light on the plate. One TM-540 camera is used for the stereo vision and mounted on a PUMA 560 robot arm. The left and the right images in the conventional imaging geometry of stereo vision are acquired by moving the camera to two different positions. In the following description, this single-camera stereo vision sensor will be treated as if there were two cameras mounted on the robot arm.

B. Exploring Strategy for the Experiment

Exploring strategies is essential for the three stages of vision sensing described in Section IV. The missions of the exploring strategy are to determine the pose of the vision sensor and the projector, and to develop the path planning for the robot arms. The performance of the vision sensor depends on the pose of the vision sensor and the projector, which will be the emphasis of this section. Path planning for the robot arms, irrelevant to the performance of the vision sensing, is not discussed in this study.

The determination of the pose of the stereo vision sensor is affected by many factors. According to [17], the requirement that will affect camera placement include the resolution, focus, field of view, visibility, view angle, and prohibited regions of the cameras. These requirements should be satisfied for the proper operation of the cameras. In addition, some parameters of the stereo vision sensor should be considered in developing the exploring strategy. In the case of a conventional imaging geometry, these parameters that will determine the pose of the stereo vision sensor include the pose of the center line, the orientation of the baseline, and the distance between the object and the center point of the stereo vision sensor. Fig. 10 shows these parameters in the structure of the stereo vision sensor. In developing the exploring strategy for the three stages of vision sensing, we are mainly concerned about these parameters.

The exploring strategy for the sensing process in detecting the targeted plate is developed in the following. In the following discussion, we assume that the length of the baseline is fixed and the focal lengths of the lenses of the cameras are on-line adjustable.

1. Strategy for the First Stage of the Sensing Process

The exploring strategy in the first stage of the sensing process should be developed in a way that a rough boundary of the plate can be sensed. The field of view of the cameras should cover the possible extent of the plate to fulfill the goal of obtaining a rough boundary of the plate for the stereo vision sensor.

As the deformed shape of the plate is not available, the possible extent of the plate is not known. However, by moving the cameras far enough away from the plate, all the area of interest in the workspace can be covered by the field of view of the cameras. The pose of the center line and the orientation of the baseline can be chosen arbitrarily since only rough boundary of the plate is needed in this stage. Based on the rough boundary, the boundary plane can be determined.

2. Strategy for the Second Stage of the Sensing Process

With the rough boundary of the curved plate available, the three parameters of the stereo vision sensor can be chosen to prevent the likelihood of the false-boundary problem in stereo vision as much as possible. When the center line of the stereo vision sensor is oriented passing through the geometric center of the actual plate boundary and perpendicular to boundary plane, the false-boundary problem has the least likelihood to occur. Once the center line was determined, the baseline should be oriented perpendicular to the direction where the plate is bent most. This arrangement of the baseline increases the similarity of the shapes seen by the two cameras, and decreases the possible occurrence of the false-boundary problem. The distance between the plate and the center point of the stereo vision sensor should be determined long enough for the field of view of the cameras to cover the extent of the plate. By the above arrangement, a more precise boundary is found from the stereo images. *Based on this new boundary, a new boundary plane can be defined.*

3. Strategy for the Third Stage of the Sensing Process

The mission of the exploring strategy in this stage is to determine the pose of the structured light projector. The projection of the structured light has been described in Section III. The center ray of the structured light should pass through the center of and perpendicular to the boundary plane as defined in the second stage.

C. *Process of the Experiment*

The process of the experiment follows the three stages of the sensing process described in Section IV. Fig. 11 shows the process of these three stages.

In the first stage, the two cameras were moved to obtain a rough location of the plate boundary. The position and orientation of the cameras were decided by the

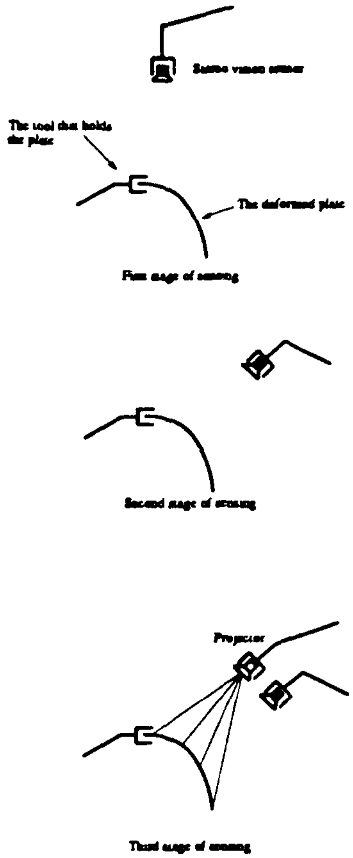
Stereo vision sensor
The tool that holds the plate
The deformed plate
First stage of sensing
Second stage of sensing
Projector
Third stage of sensing

Figure 11: The process of the vision sensing in detecting the deformed plate.

exploring strategy in the first stage of sensing process stated in subsection B.

In the second stage, the stereo vision sensor was moved to the location and orientation as discussed in the previous section. A more precise boundary is defined. By using passive stereo vision in the first and second stages, the false boundary problem can be largely eliminated.

In the third stage of sensing, the projector was moved to a position and orientation as described in the previous subsection. The matching squares created by the structured light in the two images were detected and matched. The geometric centers of the four corners of the matching squares in the images were considered as the matching points for deriving the range data of the plate. The data points of the plate corresponding to the match points in the two images were derived by the method described in Section IV.

D. *Image Processing Techniques*

The image processing for the experiment needs to detect the corners of the matching squares in the image. Based on the design of the working environment in this experiment, the images in the passive and active stereo vision can all be thresholded into binary images. Four tasks are designed to accomplish the image processing for the detection of the corners of the squares in the image: thesholding the image, boundary extraction of the squares, contour following of the squares, and corner detection of the squares. The implementation of the last three tasks is modified from the methods introduced by Cabrelli and Molter [18]. These four tasks are described in the following.

1. Thesholding

The purpose of this task is to obtain the region projected in the image from the plate in passive stereo vision as well as the regions projected in the image from the matching squares in active stereo vision. The bi-level moment preserving thresholding technique introduced by Tsai [19] was implemented for this task. This thresholding technique has two advantages. One is that the threshold value can be generated automatically. The other is that this technique can recover the ideal image from a blurred version [19]. After thresholding, the regions of the squares are black and their environment is white.

2. Boundary Extraction

In this task, the pixels on the boundary of the squares are detected by applying the following algorithm on every pixel in the thresholded image:

1. If the pixel is black and its 4NNs (four nearest neighbors: left, right, up, and down neighbors) are also black, the pixel is marked as an interior point.
2. In any other cases, the color of the pixel remains unchanged.

After this algorithm is applied, the resulting images contain a set of closed contours that are extracted from the regions of the matching squares. In order to eliminate noisy contours or pixels in the image, each black pixel in the image was examined to see if it is connected to an interior point. If it is not, it is considered to be a noisy pixel and is painted white.

The right thresholded image of the matching squares is shown in Fig. 12 (a). Its boundary-extracted image is shown in Fig. 12 (b).

3. Contour Following

The purpose of this task is to distinguish the boundary points of each square from all the boundary points which were extracted in task two and to sort these distinguished boundary points according to the order of their positions on the square boundary. The implementation of this task is similar to that in [18] and is not described.

4. Corner Detection

To detect the corners of each square in the image, we first compute the inner product of the right and the left unit tangent vector at each pixel on the boundary of the square. The right/left unit tangent vector can be approximated by the unit

(a) (b)

Figure 12: (a) Right thresholded image of the matching squares. (b) Right boundary-extracted image of the matching squares.

direction vector of the line that best fit the pixel and the following/proceeding K pixels. These two lines that best fit the $K+1$ pixels are found by using the eigenvector line fitting method [20]. The value of K is arbitrary. In this experiment, K is chosen to be eight.

After the inner products of all the boundary pixels are computed, a threshold value of the inner product can be set. The boundary pixels with their inner products larger than the threshold value are eliminated. As a result, smooth portions of the boundary of the squares are eliminated. The thresholding will provide several intervals at which the inner products of the pixels are smaller or equal to the threshold value. Each corner of the square is detected to be the pixel with minimum inner product within each interval.

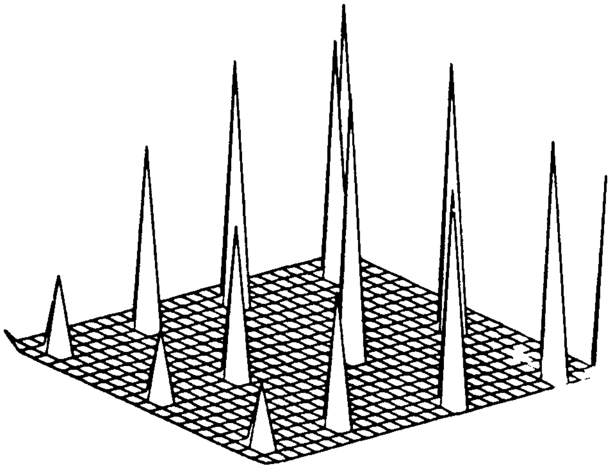

Figure 13: The sensed data points of the curved rectangular plate.

E. Results

The surface of the plate interpolated from the sixteen sensed data points by using energy minimization method is shown in Fig. 14. These sixteen points, including the four corners of the plate and center points of the twelve matching squares, are shown in Fig. 13. Energy minimization interpolation method is described in another paper [21]. In Fig. 14, the domain of the plate in the x-y plane is assumed to be a rectangular since the bending of the plate in the x and y direction is very small to be negligible.

Because the exact position and shape of the plate are not known, there is no way to measure the accuracy of the sensed data points and the interpolated surface. A test was conducted to estimate the accuracy of the passive stereo vision. Passive stereo vision was applied to detect the positions of the corners of a square on the target block that was used in hand/eye calibration. The actual coordinates of the corners of the square on the target block are known. By comparing the detected positions

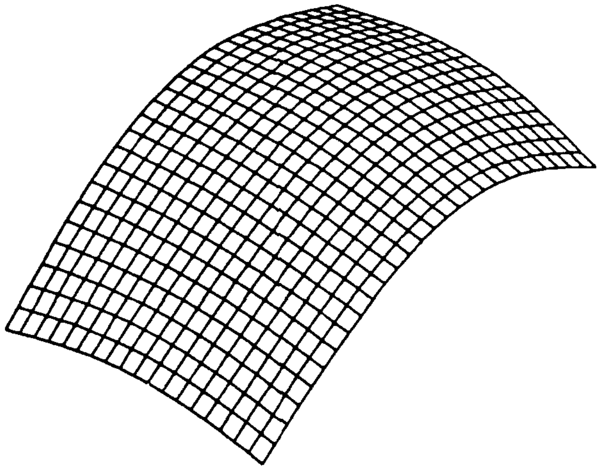

Figure 14: The interpolated surface of the deformed rectangular plate.

and the actual positions of these corners, the accuracy of the passive stereo vision that was used in this experiment can be roughly estimated. The error in the depth (z coordinate in the coordinate system of the target block) is within 2 mm and the error in the x and y coordinates is within 1 mm at a distance of about 40 cm.

VI. Conclusions and Discussions

Integration of passive and active stereo vision is introduced in this paper for shape detection. This approach is designed to detect the shape of curved/smooth surface of metal plates. The boundary and shape are first roughly identified by passive stereo vision. This identification helps ease the correspondence problem in active stereo vision; whereas active stereo vision detects detailed surface of the object. In particular, this passive and active integration approach is shown effective in detecting and solving the false-boundary problem embedded in the shape detection of the deformed metal plates. An exploring strategy is developed to assist such a sensing approach.

The three stages of sensing described in Section IV should be sufficient for detecting surfaces that are not seriously deformed such as those targeted in Section V. For surfaces that are bent in a large angle as shown in Fig. 5, the three sensing stages should be applied in different directions and distances, and repeated whenever needed. The development of the exploring strategy for the movement of the vision sensor in such cases will be much more complicated than that in the case described in Section V.

VII. References

[1] Stephen T. Barnard and Martin A. Fischler, "Computational stereo," *ACM Computing Surveys*, vol. 14, pp. 553–572, December 1982.

[2] Yeon C. Kim and J. K. Aggarwal, "Positioning three-dimensional objects using stereo images," *IEEE Journal on Robotics and Automation*, vol. RA-3, pp. 361–373, August 1987.

[3] Gongzhu Hu and George Stockman, "3-D surface solution using structured light and constraint propagation," *IEEE Transactions on Pattern Analysis and Machine Intelligence*, vol. 11, pp. 390–402, April 1989.

[4] K. L. Boyer and A. C. Kak, "Color-encoded structured light for rapid active ranging," *IEEE Transactions on Pattern Analysis and Machine Intelligence*, vol. PAMI-9, pp. 14–28, January 1987.

[5] J. Le Moigne and A. M. Waxman, "Multi-resolution grid patterns for building range maps," *University of Maryland, Tech. Report.*

[6] J. L. Posdamer and M. D. Altschuler, "Surface measurement by space-encoded projected beam systems," *Computer Vision, Graphics, and Image Processing*, vol. 18, pp. 1–17, 1982.

[7] P. Vuylsteke and A. Oosterlinck, "Range image acquisition with a single binary-encoded light pattern," *IEEE Transactions on Pattern Analysis and Machine Intelligence*, vol. 12, pp. 148–164, February 1990.

[8] D. Marr and T. Poggio, "Cooporative computation of stereo disparity," *Science*, vol. 194, pp. 283–287, 1976.

[9] Chichyang Chen and Yuan. F. Zheng, "A new robotic hand/eye calibration method by active viewing of a checkerboard pattern," *Submitted for publication*, 1991.

[10] W. E. L. Grimson, *From Images to Surfaces: A Computational Study of the human Early Visual System.* Cambridge, MA: The MIT Press, 1981.

[11] H. P. Moravec, "Towards automatic visual obstacle avoidance," *Proc. Fifth International Joint Conference on Artificial Intelligence*, p. 584, 1985.

[12] G. Medioni and R. Nevatia, "Segment-based stereo matching," *Computer Vision, Graphics, and Image Processing*, vol. 31, pp. 2–18, 1985.

[13] Luc Robert and Oliver D. Faugeras, "Curve-based stereo: Figural continuity and curvature," *Proc. IEEE Conference on Computer Vision and Pattern Recognition*, pp. 57–62, June 1991.

[14] K. L. Boyer and A. C. Kak, "Structural stereopsis for 3-D vision," *IEEE Transactions on Pattern Analysis and Machine Intelligence*, vol. PAMI-10, pp. 144–166, March 1988.

[15] Suresh B. Marapane and Mohan M. Trivedi, "Region-based stereo analysis for robotic applications," *Proceedings of the IEEE Systems, Man, and Cybernetics Conference*, vol. 19, pp. 1447–1464, November/December 1989.

[16] Umesh R. Dhond and J. K. Aggarwal, "Structure from stereo—a review," *Proceedings of the IEEE Systems, Man, and Cybernetics Conference*, vol. 19, pp. 1489–1510, November/December 1989.

[17] Cregg K. Cowan and Peter D. Kovesi, "Automatic sensor placement from vision task requirements," *IEEE Transactions on Pattern Analysis and Machine Intelligence*, vol. 10, pp. 407–416, May 1988.

[18] Carlos A. Cabrelli and Ursula M. Molter, "Automatic representation of binary images," *IEEE Transactions on Pattern Analysis and Machine Intelligence*, vol. 12, pp. 1190–1196, December 1990.

[19] W. H. Tsai, "Moment-preserving thresholding: A new approach," *Computer Vision, Graphics, and Image Processing*, vol. 29, pp. 377–393, 1985.

[20] R. O. Duda and P. E. Hart, *Pattern Classification and Scene Analysis.* New York: Wiley, 1973.

[21] Chichyang Chen and Yuan. F. Zheng, "Visual surface reconstruction using patches," *Submitted for publication*, 1991.

APPENDIX B

DIGITIZING AN UNKNOWN SURFACE WITH MULTIPLE NON-CONTACT LASER SENSORS*

A Technical Report

by

Kevin Smith and Yuan F. Zheng

Dept. of Electrical Engineering
The Ohio State University
Columbus, OH 43210

---

* ACKNOWLEDGMENT: This work was supported by the Office of Naval Research under grant N00014-90-J-1516 and by the Engineering Research Center for Net Shape Manufacturing of the Ohio State University.

EXECUTIVE SUMMARY

Project Statement and Objective

This research investigates digitizing methodologies for maintaining ideal sensor-to-surface orientation for digitizing an unknown object. A digitizing system was built to aid in this investigation. In this system, two Laser Displacement Sensors (LDS) are position during the digitizing process by a six degree-of-freedom robot. A state-of-the-art review of other research in this area is presented in the introduction. Also, an extensive list of companies marketing Laser Displacement sensors and Digitizing Systems is found in the appendix.

Progress to date

This report represents the work accomplished over a two years period culminating in a Masters Thesis defense. During this period, a review on the state-of-the-art in the digitizing technology was conducted. The review consisted of three aspects. The first aspect studies the current technology in Laser Displacement Sensors. The second aspect studies the methodologies of the digitizing process, and

the third aspect studies the surface reconstruction using digitized discrete data points.

From studying the existing technology, maintaining a near normal sensor-to-surface orientation was found to be a key issue in obtaining a precise reconstruction of an unknown surface. Since the surface is unknown, however, it is difficult to predict such an orientation. A new methodology is proposed to achieve a precise measurement. The new methodology incorporates a six degrees-of-freedom robot and multiple laser displacement sensors (LDS). Using multiple LDS, variations in surface contour can be locally predicted. Using this result, the ideal sensor-to-surfaced orientation can be maintained. This report details the system's implementation and describes the proposed sensor-to-surface orientation techniques. A detailed error analysis is presented using the assumption that the unknown surface has a finite maximum curvature. And finally, an experimental verification of the proposed techniques is presented.

Further Work

Future work will examine new digitizing approaches which continue to scan the unknown surface as planer curve but removes the restriction on the LDS orientation vector that it be kept within a plane.

TABLE OF CONTENTS

CHAPTER PAGE

EXECUTIVE SUMMARY ii

LIST OF TABLES vii

LIST OF FIGURES viii

I. INTRODUCTION 1

II. DIGITIZING TECHNOLOGY REVIEW 6

- 2.1 Introduction 6
- 2.1 The Principle of the Triangulation Approach 9
- 2.2 Research on the LDS 11
  - 2.2.1 Improving the Existing LDS Performance 11
  - 2.2.2 Reducing LDS Sensitivity to Surface Inclination 14
- 2.3 Improving the Digitizing Process 17
  - 2.3.1 The Center of Gravity Approach 17
  - 2.3.2 Condensation-Assisted Approach 19
  - 2.3.3 Rotating the Object Approach 20
- 2.4 Surface Reconstruction Techniques 21
  - 2.4.1 Regularization Approach 22
  - 2.4.2 The Parametric Grid Construction Approach 25

2.5 Summary....................27

III. MATHEMATICAL DEVELOPMENT....................29

3.1 Multiple Beam Approach....................29

3.2 Extrapolation Approach....................33

3.3 Summary....................37

IV. EVALUATION OF EXTRAPOLATION APPROACHES....................38

4.1 General Overview....................39

4.2 A Plane Curve With Finite Max. Curvature is Bounded Locally....................41

4.3 A Curve's Slope Is Bounded In The Locally Bounded Region....................47

4.4 Worst Extrapolation Case....................54

4.5 Deriving Error Parameter Functions....................56

4.5.1 Relationship Between $\Delta s/R$ and s/R....................57

4.5.2 Relationship Between ρ/R and s/R....................59

4.5.3 Relationship Between θ and s/R....................61

4.6 An Example Of Calculating The Sampling Arc Length....................63

4.7 Summary....................65

V. EXPERIMENTAL SYSTEM....................66

5.1 System Architecture....................66

5.2 System Software....................69

5.3 Nonlinear Robot Position Accuracy....................72

5.4 Summary....................80

VI. EXPERIMENT....................81

6.1 Calibration....81
6.2 Digitizing Rate....82
6.3 Demonstration of Extrapolation Approaches....83
6.4 Surface Reflectivity....87
6.5 Angle of Incidence Error....87
6.6 Summary....89
VII. CONCLUSIONS....90
APPENDIX....92
REFERENCES....95

LIST OF TABLES

TABLE PAGE

2.1 Select Listing of Laser Displacement Sensors 13
5.1 Hardware Specification..68
6.1 Digitizing Rate...82

LIST OF FIGURES

FIGURE PAGE

2.1 Principle of Triangulation Approach 10

2.2 Structure of Multiple Lens Approach 15

3.1 Multiple Beam Approach - Two LDS 30

3.2 Multiple Beam Approach - Three LDS 32

3.3 2nd Order Polynomial Extrapolation 34

4.1 Digitizing Error Parameters 40

4.2 A Plane Curve and Bounding Tangent Circles 42

4.3 Bound on Local Curve Points 45

4.4 Locally Bounded Region 46

4.5 Bound on Local Slope Values 48

4.6 Extreme LDS Beam Orientation 49

4.7 Maximum Slope Curve Showing Angles {B, C} 51

4.8 Min. Slope Curve Showing Angles {A, D, F} and Side x 53

4.9 Extreme Slope Curves as a function of $\frac{DR}{R}$ with LDS Orientation, g, Held Constant 53

4.10 Worst Case Curve Estimation 55

4.11 Measured Curve's Arc Length 58

4.12 Plot of Error Parameter $\frac{\Delta s}{R}$ as a Function of Normalized sampling arc length, $\frac{s}{R}$ 59
4.13 Plot of Error Parameter $\frac{\rho}{R}$ as a Function of Sampling Arc Length, $\frac{s}{R}$ 60
4.14 Plot of Error Parameter θ as a Function of Sampling Arc Length,$\frac{s}{R}$ 62
4.15 Composite Plot of Error Paramters as a Function of Sampling Arc Length 62
5.1 Major Components in Digitizing System 67
5.2 Control Software Modules 69
5.3 Two link Robot 73
5.4 Positioning Locations within the Operating Envelope of a Two-Link Robot Arm with a1=2 a2 75
5.5 Positioning Locations within the Operating Envelope of a Two-Link Robot Arm with a1 = a2 76
5.6 Manipulability Ellipsoids with a1 = 2 a2 78
5.7 Manipulability Ellipsoids with a1 = a2 79
6.1 Photograph of Complex Surface and Digitizing System 84
6.2 Plot of Digitized Complex Surface (units=mm) 84
6.3 2nd Order Polynomial Extrapolation with Bad Data Point 86

6.4 The Difference Between the Average Digitized z Axis Value with the LDS Oriented at 60° and the Average Value with the LDS Oriented at 90°nce Between the Average Digitized z Axis Value with the LDS Oriented at 60° and the Average Value with the LDS Oriented at 90°....................88

6.5 The Difference Between the Average Digitized z Axis Value with the LDS Oriented at 120° and the Average Value with the LDS Oriented at 90°...89

CHAPTER I

INTRODUCTION

In recent years, digitizing product model surfaces has become increasingly important to the manufacturing industry. The digitizing technology is especially important when computer-aided-design systems fail to aid in the design process of product surfaces. For example, in the automobile industry, draw die engineers often build a ceramic draw die model in order to design the draw die addendum surfaces. The addendum surfaces are constructed around the periphery of the model's product surfaces (e.g. an automobile body part). These addendum surfaces are designed to control the draw characteristics of the forming sheet metal. If these surfaces are not adequately designed, the sheet metal will be either wrinkled or torn. Due to their complexity, the addendum surfaces are created by hand on the ceramic models [1]. The engineer uses his or her own experience to determine the "correct" surfaces to use. (Note, the surface design is not unique. This can be observed by comparing the addendum surfaces designed by different engineers for the same product surface model.

The designs are usually significantly different.) Once designed, these surfaces are digitized to create a data base that the CAM software can use. The CAM software is used to aid in manufacturing a prototype draw die.

In other cases, even the product surfaces are too complicated to be designed using CAD tools. Instead, the product surfaces are entirely designed using clay or ceramic models. To manufacture draw dies or injection molds for these kinds of products, the clay or ceramic models must first be digitized. The digitizing data can then be used to generate programs for numerically controlled (NC) machines which machine the dies or molds.

Another application of the digitizing technology is in "rapid part acquisition" or so called "3-D copying" [2] . This is a process which reduces the time and cost to manufacturing critical parts whose CAD model is not available. Such a process is important in the efficient and effective maintenance of valuable equipment utilized in both military and civilian organizations.

Although the digitizing technology is increasingly important in today's manufacturing activities, many aspects of the technology still need to be enhanced. As illustrated, the digitizing process needs to be fast, accurate, reliable, nondestructive, and needs to produce an efficient data base for CAM software to use. In the past, coordinate measuring machines (CMM) using touch probes have been used for digitizing sculptured surfaces. Digitizing using a CMM with a touch probe is accurate and reliable; however, it is also slow. This has motivated several tool manufacturers to replace the touch probe with a Laser Displacement Sensor (LDS). In addition, 3-axis machining centers are now being used to position the LDS while digitizing. See Appendix A for a list of tool manufacturers that market digitizing machines.

The LDS can collect sculptured surface data faster than a touch probe. In addition, the LDS does not require mechanical parts to come in contact with the sculptured surface, thus protecting the surface from possible damage or movement. However, the LDS's accuracy depends on the position and orientation of the laser with respect to the sculptured surface. The LDS is most accurate when its orientation is nearly normal to the sculptured surface and the surface is within the LDS's effective stand-off range.

On 3-axis machines, the LDS is held in a fixed orientation while digitizing. This limits the types of sculptured surfaces that can be digitized. Because, the LDS's orientation must be within a specified range of sensor-to-surface perpendicularity, only sculptured surfaces that fall within that range can be digitized. Work has been done to increase the LDS's surface-to-sensor orientation range [3]. However, by using a six degree-of-freedom robot for positioning and orienting the LDS, a more general sculptured surface (one with high tangential variations) can be digitized. Use of an articulated machine is suggested by the authors. The LDS's position and orientation can then be continuously changed during the digitizing process. Thus, narrower variations in sensor-to-surface orientation can be maintained.

To study the issues involved with maintaining a near perpendicular orientation between the sculptured surface and LDS, a non-contact 3-D digitizing system with six degrees-of-freedom was constructed. The system uses two LDS's which are positioned using a robot manipulator. Two different approaches to maintaining sensor-to-surface orientation while digitizing were investigated, namely the Multiple Beam Approach and the Extrapolation Approach.

The structure of this report is as follows. In the next chapter, we review the state-of-the-art in laser digitizing technology. The review will include three main topics: LDS technology, digitizing methodologies, and surface reconstruction. The first topic, LDS technology, is a review of the current state-of-the-art in the Laser Displacement Sensor. The second topic, digitizing methodologies, is a review of the methodologies for digitizing unknown surfaces. And, the third topic, surface reconstruction, is a review of methods for representing the surface based on the digitized data.

The rest of the report will present our research results. Chapter 3 outlines the mathematical background for the two proposed digitizing approaches. Chapter 4 studies the theoretical limitations of these two approaches given that the unknown surface has a finite maximum curvature. Chapter 5 describes the hardware and software used to construct the digitizing system and briefly discusses the nonlinear positioning accuracy of an articulated machine. Chapter 6 presents the experimental results of the proposed digitizing approaches. Finally, the report concludeds with a summary.

CHAPTER II

DIGITIZING TECHNOLOGY REVIEW

2.1 Introduction

Digitizing techniques have been used in the manufacturing industry since the '70s. Automotive and aerospace engineers have used digitizing methods to produce prototype tooling directly from clay models. In recent years, digitizing surfaces has become useful in more applications, such as in the production of injection molds, die molds, and in rapid prototyping. As applications for digitizing technology have increase, more research activities have been conducted to improve the precision, efficiency, and flexibility of this technology. The research is especially active in Japan and in European countries.

In the earlier years and still today, digitizing systems have used touch probes for their measuring sensor. As the name suggests, touch probes need to come in contact with the object's surface in order for the digitizing system to take a single measurement. Due to the slow mechanical nature of this process, measuring a large number of data points can be very time consuming using a touch probe. In recent years, non-contact measurement sensors have been introduced which do not require the sensor to physically come in contact with the object's surface. This dramatically decreases the time needed to digitize a surface. A number of optical techniques are available for taking non-contact measurements. Most of them can be classified into three categories. They are time-of-flight, interferometry, and triangulation methods [4].

The time-of-flight approach is effective when the object is at least several meters away from the sensor and high precision is not required. The interferometric approach, on the other hand, is effective for short range measurements and provides resolution in the range of a few microns. Both time-of-flight and interferometric approaches require a complicated optical-mechanical system and are not practical to implement. By far, the most popular approach is the triangulation approach. The triangulation approach is simple to implement. It only requires a light source and a light sensor to make distance measurements (the principle of the triangular approach will be discussed later in this chapter). Many commercial products based on the triangulation principle are available on the market. Among them, a device called a laser displacement sensor (LDS) is the most popular. In such a device, a laser beam generated by a laser diode serves as the light source and a charged coupled device (CCD) sensor serves as the light sensor. With the advent of the laser diode technology, a LDS can be designed in compact sizes. These small housing allow the LDS to be mounted on the spindle of CNC machines. As a result, CNC machines can be easily turned into a digitizing system. In addition, the LDS can also replace the touch probe on a coordinated measurement machine (CMM). Increasing the digitizing speed has been the main advantage to replacing the touch probe on the CMM.

Overall, the digitizing process of an object is divided into two main steps. The first step is to obtain a set of point measurements on the object's surface. The second step is to turn this set of data points into a CAD representation. This step is often called surface reconstruction. Performance of the first step is measured by the speed and accuracy in obtaining the data points and by the robustness in the digitizing method, i.e., the range of surface variations that can be accurately digitized. Performance of the second step is measured by the efficiency in the representation of the reconstructed surface and by the efficiency in the algorithm which converts the data points into the reconstructed surface.

Research directed towards improving the digitizing process performance is actively being conducted all over the world. Improvement is being achieved in three different areas. The first area improves the LDS technology by designing new and innovative structures. The goal is to improve the resolution of the LDS and to make the resolution insensitive to surface conditions. The second area improves the digitizing process by maintaining sensor-to-surface orientation. One approach, uses image processing to filter the data obtained from the LDS. This method is called the center of gravity approach. The objective is to increase measurement precision by eliminating the noise sensed by the sensor. Another approach, artificially varies the surface's reflective attributes such that the LDS can digitize even transparent surfaces. This method is called the condensation-assisted approach. The third approach discussed in this area is the rotating-the-object approach. The third main area involves improving algorithms for surface reconstruction. After an introduction to the triangulation principle, current progress made in these three main areas will be reviewed.

2.1 The Principle of the Triangulation Approach

In the triangulation approach, a laser beam is used as a light source to generate a spot on the object's surface. The spot is detected by a light sensing device (a CCD sensor for example) through a focus lense. As the distance from the spot to the light source varies, the projection of the spot on the CCD sensor also varies, see Fig. 2.1. By identifying the projected spot's position on the CCD sensor, the displacement of the object surface can be calculated.

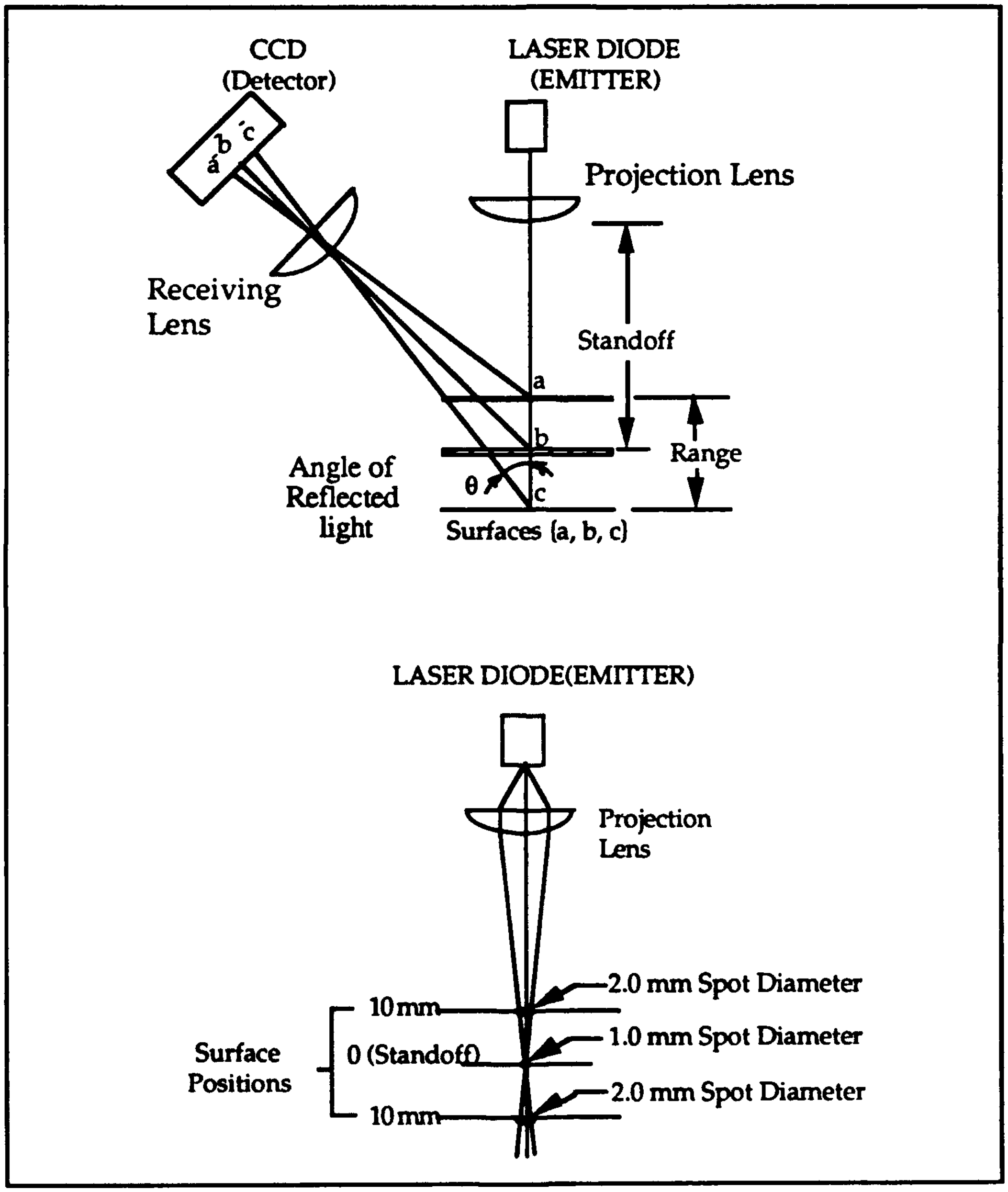
CCD
(Detector)
LASER DIODE
(EMITTER)
a
b
c
Projection Lens
Receiving
Lens
Standoff
a
b
c
Range
Angle of
Reflected
light
θ
Surfaces (a, b, c)
LASER DIODE(EMITTER)
Projection
Lens
2.0 mm Spot Diameter
1.0 mm Spot Diameter
2.0 mm Spot Diameter
10mm
0 (Standoff)
10mm
Surface
Positions

Figure 2.1 Principle of Triangulation Approach

The precision of the triangulation approach depends on a number of factors, such as, the resolution of the CCD sensor, the area of the spot, and the reflectance property of the surface, etc. Considerable research has been conducted by both industry and academia. These will be reviewed in the rest of this chapter.

2.2 Research on the LDS

2.2.1 Improving the Existing LDS Performance

The performance of the LDS can be improved in many ways. Fundamentally, the diameter of the laser beam should be as small as possible so that the light source will ideally activate only one pixel on the sensing device. In addition, the resolution of the CCD sensing device should be as small as possible. This requires increasing the pixel density on the CCD sensing device. In recent years, improvements in these two areas have resulted in many new LDS products with outstanding performance. A selected list of LDS products (available in the North American market) and a limited summary of their specifications are shown in Table 2.1.

As shown in Table 2.1, the LDS (CyberOptics PRS-15) with the highest resolution (0.381 mm) also has the smallest measuring range (±0.15 mm). A small light spot is necessary to attain the higher precision. However, since a small light spot generates a weak light intensity, the CCD sensor must be close to the spot in order to sense it. As a result, higher precision is achieved at the cost of a smaller measuring range. This general observation is illustrated by comparing two LDS marketed by Keyence (models LB-70 and LB-72). Model LB-70 has a spot diameter of 1.0 x 2.0 mm, a resolution of 40 mm, and a measuring range of 100 ±40 mm. Whereas, Model LB-72 has a spot diameter of 1.0 mm, a resolution of 15 mm, and a measuring range of 40 ± 10 mm [5].

Another factor that affects the LDS's precision is the angle of incidence (or angle of inclination) of the laser beam. Clearly, when the light beam is normal to *the object* surface, the light spot has the smallest area, and the LDS provides the highest resolution. When the light beam angle is changed from its normal orientation, the spot area increases. As illustrated earlier, this enlarged spot area decreases the resolution of the LDS. For example, when the incident angle is off 30 degrees from a normal orientation, the Keyence LDS generates an error as big as 2% of the measured distance [5]. This error is too large for many applications.

Even worse, if the incident angle is larger than 45° the LDS can fail [3]. The triangulation approach assumes that the diffused light reflected from the object surface will reach the CCD. When the orientation of the laser beam is not normal to the object surface, the

Table 2.1 Select Listing of Laser Displacement Sensors available in the North American market.

Company Part No.	Measuring Range (mm)	Resolution (mm)	Response Time (ms)	Sensor Size (sq-in)
Aromat				
MQLAS4LA 120V14	40 ±10	2.5	25	3.1
MQLAS3LA C120VS10	150 ±50	600	2	3.1
Chesapeake Laser Systems				
LTG-2101	254 ±2.5	2	0.6	5.4
LTG-2125	635 ±38	13	0.6	217
CyberOptics				
PRS-15	6.60 ±0.15	0.381	N/A	7.4
PRS-1600	60.96 ±16	40	N/A	4.6
Keyence				
LB-72	40 ±10	15	2	2.0
LB-70	100 ±40	40	20	2.0
Micro Switch				
HSV 100	39 ±6	6	10	47.6
Renishaw				
OP5M	50 ±10	2.5	15	12.3
Selcom				
2301	95±4	N/A	N/A	N/A
2005	1200 ±512	N/A	N/A	N/A
Medar				
MDC-250	200 ±50	116	1	109.5

amount of diffused light that reaches the CCD may be insufficient. As a result, the sensor is rendered disabled. However, maintaining a normal orientation to an unknown surface is not easy. To resolve this problem, researchers have looked at ways to make the LDS less sensitive to surface inclination. Their efforts will be reviewed in the next subsections.

2.2.2 Reducing LDS Sensitivity to Surface Inclination

A notable research effort in reducing the LDS sensitivity to surface inclination was made by Saito and Miyoshi of Hokkaido University in Japan [3]. They proposed a multiple lense structure to overcome tne sensitivity problem. The structure consists of a He-Ne laser, four optical lenses and three CCD sensors as shown in Fig. 2.2.

One lens is larger in diameter than the other three and is called the object lens, L_1. The other three lenses called converging lenses are positioned between the object lens and a CCD sensor. The three converging lenses and three CCD sensors are spaced 120° apart around the optical axis of the object lens. The CCD sensor (7 mm by 2560 pixels) is placed at the focus length of the converging lense, f_2. The laser beam is directed through the center of the object lens and onto the target surface. Some of the diffused light reflected off of the target surface passes back through the object lens. This light continues

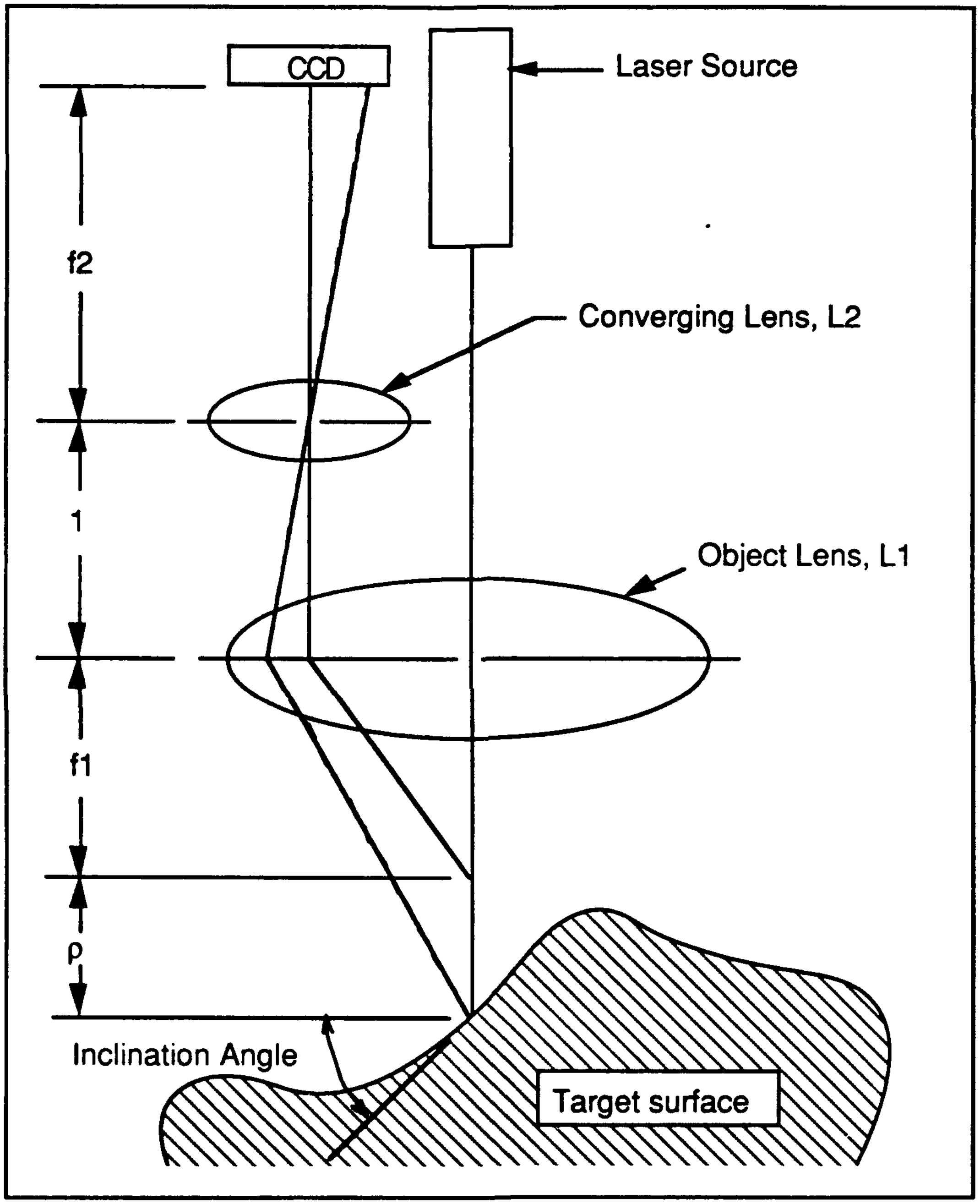
CCD
Laser Source
f2
Converging Lens, L2
1
Object Lens, L1
f1
p
Inclination Angle
Target surface

Figure 2.2 Structure of Multiple Lens Approach

through the converging lenses and is finally detected at the CCD sensors. From the position of the sensed light on the CCD sensors, the distance ρ can be determined. The distance ρ is the distance from the object lens focus length, f_1, to the target surface. The location of the spot on the CCD sensor, d, is determined by the following equation:

$$d = \frac{a\, f_2\, \rho}{(f_1)^2} \tag{2.1}$$

Since, {a, f_1, f_2} are constants and {d} is determined by the CCD sensor, the unknown displacement value, ρ, can be calculated from Eq. (2.1).

Using multiple CCD sensors, this LDS structure can measure larger contour variations in the target's surface. Due to the position of the three converging lenses and CCD sensors, each CCD sensor measures the same displacement, ρ. As the target surface inclination renders one or two of the CCD sensors disabled, the remaining CCD sensors can continue to measure the displacement, ρ. In this way, the LDS becomes less sensitive to surface inclination. This LDS sensor design is reported able to measure target surface inclinations up to 70° [3]. Although, this new LDS increased the surface inclination range that could be measured without a complete sensor failure, the accuracy of the measurement is still proportional to the inclination. This problem was not addressed by the authors.

2.3 Improving the Digitizing Process

Several companies have implemented the LDS on 3 axis CNC milling machines, see appendix A. The LDS is mounted on the machine's spindle where a cutting tool would normally be mounted [6]. Because of the machine's limited degree-of-freedom, the LDS is maintained in a fix spindle-to-sensor orientation during the digitizing process. Since the measurement accuracy is a function of the inclination angle, a limited range of surfaces can be digitized using this method. Recently, two different efforts have been made to improve the precision and robustness of the digitizing process. The first effort is called center of gravity approach which processes a video imagine of the CCD sensor. The second effort artificially modifies the object surface conditions. These two approaches will now be discussed in more detail.

2.3.1 The Center of Gravity Approach

More advanced technology is needed to implement a reduced laser spot area method, as discussed above, for improving the LDS's precision. Due to this technology limitation, an "effective" spot area reduction approach has been developed, called the center of gravity approach. In the center of gravity approach, the center of a relatively large spot is identified. This center point is used to calculate the displacement. Using this approach, the LDS's resolution is dramatically improved.

The spot's center of gravity is identified using a moment computation technique developed in computer vision [7]. Accuracy of the calculated center of gravity is within a single pixel on the CCD sensor. As a result, the precision can be improved by a factor of ten. As an example, using this approach CyberOptics Corp's LDS has a resolution ten times better than that of a similar LDS made by Keyence [8] which uses a "traditional" approach. Because an image processing unit is needed, the hardware used to implement the center of gravity approach is more expensive.

In [9], Soucy et al. further study the case when the spot crosses over a reflectance discontinuity. When the laser spot crosses over a reflectance discontinuity, only part of the spot is likely to be seen by the CCD sensor. Consequently, there will be an error between the center of gravity point obtained from the sensed spot and the actual center of gravity point on the surface. In order to better understand the performance of LDS in this case, a model is presented to describe the behavior of the center of gravity position. First, the intensity of the laser spot is assumed to be a 2-D Gaussian distribution and the reflectance discontinuity is an ideal step function. In this model, the interpolation error is proportional to the integral of the image spot's variance over the discontinuity. This study reveals that the center of gravity approach has significant errors when the laser spot crosses over areas with reflectance discontinuity. Although, an error analysis model is given by [9], no approach is proposed to cope with the discontinuity.

Another error in center of gravity position is introduced when the incidence angle varies. This alters the relative position of the center of gravity within the spot. Thus, measurement precision is affected when the incident angle is not zero.

2.3.2 Condensation-Assisted Approach

As just discussed, variations in the light reflectance property of the object surface can introduce errors in the LDS measurements. When the object surface is reflective or transparent instead of diffuse, the orientation of the LDS to the surface is more critical, because the the light can be directed away from the CCD sensor. To prevent this problem, Little and Vavreck developed a condensation-assisted approach to artificially modify the reflectance property of the surface [10]. In the condensation-assisted approach, a thin layer of water droplets is deposited on the object surface by directing warm moist air at the laser spot. Here, the surface takes on a semi-diffuse reflectance property, allowing normal operation of the LDS. As a result, a diffuse-type LDS can be used to measure shiny or transparent surfaces. The disadvantage of this approach is the necessity to implement a complicated mechanical system for water deposit.

2.3.3 Rotating the Object Approach

When the object has a round or cylindrical shape, maintaining a reasonable inclination angle is difficult. An alternative approach to digitizing small objects with these shapes has been investigated. In this approach, the LDS is kept stationary and the object rotates.

Saint-Marc et. al. recently developed a PC-based range finding system composed of an independent laser system which projects a sheet of light on the object surface [11]. The object is mounted on a rotary table driven by a personal computer. As the table rotates, the entire area of the object can be digitized while maintaining a reasonable incident light angle.

In Japan, the same rotating-object approach is used to digitize the profile of a last [12]. The profile data is integrated into a CAD system and used for designing shoes. During the digitizing process, the last is rotated while the LDS is moved along the rotating axis. As a result, the entire last can be digitized with high precision.

2.4 Surface Reconstruction Techniques

After digitizing a surface, the set of discrete data points needs to be converted into a mathematical representation. The mathematical representation is necessary to store and modify the surface information in a convenient and efficient manner. In general, the surface can be expressed in an implicit or explicit form [13]. In the explicit form, the surface height is expressed as a function of the surface plane coordinates (x,y):

$$z = f(x, y). \tag{2.2}$$

In the implicit form, the surface is expressed as the function

$$f(x, y, z) = 0 \tag{2.3}$$

where (x, y, z) are the Cartesian coordinates of the surface point. The above approaches are widely used in computer vision for recognizing objects.

The CAD systems, on the other hand, uses a parameterized approach. In general, the parameterized form expresses the surface using the following equation:

$$X(u, v) = (x(u, v), y(u, v), z(u, v)), \tag{2.4}$$

where (u, v) are parameters within the range [0, 1]. There are many parameterized representations in CAD systems including Coon's Patch, B-Spline, and Beizer-Surface [14]. Since they are all well defined approaches, the details of these representations will not be addressed here.

Difficulties in creating a mathematical representation for the surface fall into one of two categories. Either, there is insufficient data, or too much redundant data in the set of digitized data points. Approaches for handling these two cases are presented below.

2.4.1 Regularization Approach

The regularization approach finds a surface representation from a sparse data set. Because the data set is sparse, a surface that satisfies the set's constraint is not unique. This approach utilizes a stabilizing functional S(s) and a penalty functional P(s). Here, s defines the point coordinates on the surface. The penalty functional defines a cost associated with an inexact match between the reconstructed surface and the discrete data points. The stabilizing function, on the other hand, restricts the possible surface space. Thus, the surface reconstruction problem requires minimizing the following energy function

$$E(s) = S(s) + P(s). \tag{2.5}$$

Grimson is probably the first one to give a rigorous mathematical derivation of the stabilizing functional. According to his "surface consistency theorem" [15], the reconstructed surface should be the smoothest surface that passes through the data points. The stabilizing functional he chose is

$$S(s)=\iint [(s_{xx})^2+2(s_{xy})^2+(s_{yy})^2]\, dx\, dy. \tag{2.6}$$

This functional is the strain energy of a thin plate, usually called "thin plate spline". The penalty functional Grimson chose for surface approximation is

$$P(s)= b \sum [s(x_i, y_i) - d_i]^2 \tag{2.7}$$

where i indicates the digitized points. By minimizing the energy as defined above, Grimson was able to find a smooth surface from a sparse set of data [15].

More recently, Muraki et al. extended the regularization approach by introducing more constraints [16], which included smoothness, fitness, and contour line constraints. These constraints are used to ensure that the reconstructed surface smoothly approximates the known elevation values. They also ensure that surface has the same height value for all points on [illegible] contour line. Thus, the reconstructed surface is a better representation of the original surface. The energy functional is minimized by solving a large linear system of simultaneous equations. The authors have successfully reconstructed a detailed 3D surface by applying this method on a sparse data set from a known surface.

The preceding two methods convert a sparse data set into a dense data set. However, the dense data set is still not in a parameterized representation. Recently, Chen and Zheng [17] developed a new approach based on the energy minimization principle. First, they used a Coon's composite patch approach to represent the unknown surface. Then, using the energy minimization approach, the coefficients of the Coon's patch representation are calculated. As a result, the reconstructed surface is represented in a format compatible with CAD systems.

There are many variations to the regularization approach; however, all are based on the energy minimization principle.

Although, they are not elaborated here, other regularization approaches can be found in [13].

2.4.2 The Parametric Grid Construction Approach

In comparison, few papers are published on the subject of surface reconstruction from a dense set of data. A notable work in the area is by Vemuri [18, 19]. He developed a parametric grid approach for finding a surface representation from a dense set of digitized data. In his approach, a parametric or computation grid $\{(s_i, t_j)\}$, $i = 1, \ldots, m$, $j = 1, \ldots, n$, is first constructed. The grid is constructed in such a way that for each i and j, there exists (s_i, t_j) that satisfy the following equation:

$$(f^1(s_i, t_j), f^2(s_i, t_j), f^3(s_i, t_j)) = (x_{ij}, y_{ij}, z_{ij}) = p_{ij} \tag{2.8}$$

where (x_{ij}, y_{ij}, z_{ij}) represents the dense data set and the functions $f^k(s_i, t_j)$, k=1,2,3, are to be determined.

The parametric grid construction yields a boundary conforming curvilinear coordinate system. Here, some coordinate lines are coincident with each boundary segment and the other curvilinear coordinates vary along the boundary segment monotonically. With the values of the curvilinear coordinates thus specified on the boundary, the values in the Cartesian coordinate system were generated, one-to-one, from these boundary values.

The increments of all the curvilinear coordinates were defined to be unity. Then, these coordinates were normalized to the interval [1, N], where N = n, m. More precisely, the grid points s and t were determined in the following way:

$$s_{i+1} = s_i + \frac{1}{n} \sum_{j=1}^{n} (\frac{(\| p_{i+1,j} - p_{i,j} \|)}{(\Sigma \| p_{k+1,j} - p_{kj} \|)} \tag{2.9}$$

and

$$t_{j+1} = t_j + \frac{1}{n} \sum_{j=1}^{n} (\frac{(\| p_{i,j+1} - p_{i,j} \|)}{(\Sigma \| p_{i,k+1} - p_{kj} \|)} \tag{2.10}$$

With the parameters s and t defined above, the mapping between the Cartesian coordinates and the curvilinear system is unique.

Once the parametric grid is constructed, the same energy-minimization principle is used to find a smooth surface representation which minimizes the error between the constructed surface and the digitized points. If the digitized data measurements are accurate, they can be used directly to fit CAD surface formats, such as Coon's patch, B-spline, or Beizer [18, 19].

2.5 Summary

In this chapter, we have reviewed the state-of-art in digitizing technology. In addition to the works mentioned above, research efforts have also been made in references [20-44]. As discussed, the current research direction can be grouped in the three aspects, i.e., LDS technology, digitizing methodologies, and surface reconstruction algorithms. Overall, the progress in the LDS technology is more advanced than the digitizing methodologies. That is, current digitizing methodologies do not adequately utilize the high precision available in LDS. For example, Aromat Corporation of Japan has released preliminary specifications claiming their LA300 series LDS (to be on the market in 1992) has a resolution of 0.2 mm ($8x10^{-6}$ inch). The best mechanical positioning accuracy is far less sensitive than this. Even when the positioning resolution is high, if good orientation between the LDS and the surface is not maintained, the LDS's resolution will be degraded or rendered disabled.

To improve the digitizing process performance, we propose a new approach. The approach uses a six degree-of-freedom robot to automatically orient the LDS's beam so that the optimum resolution of the sensor is maintained. Our efforts in this direction are reported in the remaining chapters.

CHAPTER III

MATHEMATICAL DEVELOPMENT

The two proposed extrapolation approaches are developed mathematically in this chapter. The Multiple Beam Approach is presented first followed by the Polynomial Extrapolation Approach. The purpose of these approaches is to estimate (or extrapolate) the position and orientation of the surface at the next point to be digitized. This information is used to position and orient the LDS so that it maintains a near perpendicular orientation to the surface and a constant stand-off distance from the surface.

3.1 Multiple Beam Approach

The multiple beam approach consists of positioning and orienting a set of LDS which simultaneously collect local information about the surface. The gathered information is then used to extrapolate the next surface point to be digitized. The amount and type of information gathered depends on the number of LDS in the set. Using two LDS, a surface point along with a surface tangent vector through that point can be determined. Using three LDS, the local surface curvature can also be determined. The concept of the Multiple Beam Approach using two LDS can be explained through use of the illustration in Fig. 3.1.

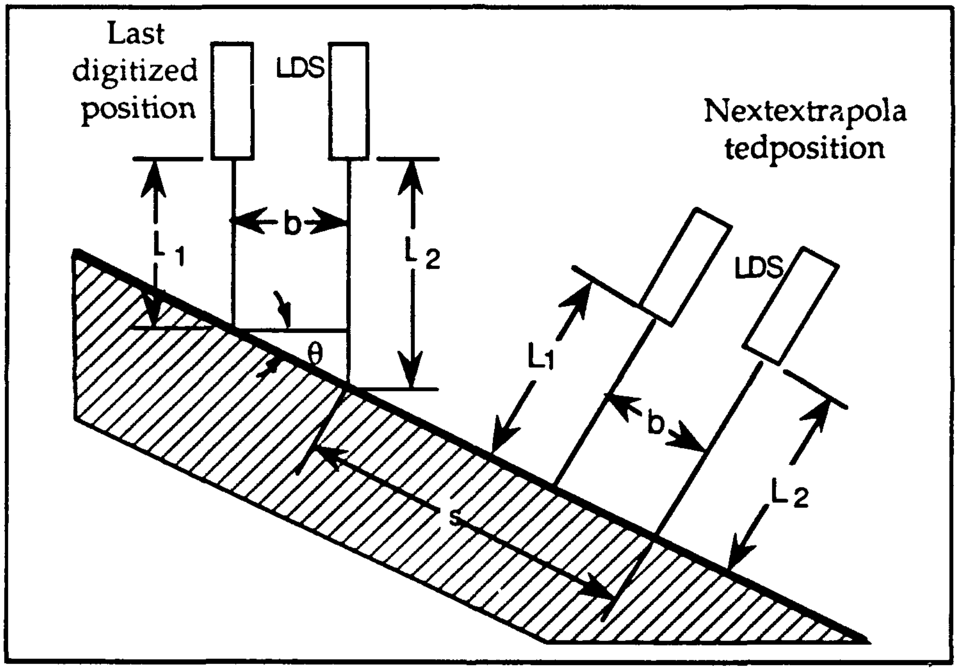
Last digitized position
LDS
Nextextrapola tedposition
b
L1
L2
θ
LDS
L1
b
L2
s

Figure 3.1 Multiple Beam Approach - Two LDS

In this case, two LDS are mounted as a set with their laser beams parallel to each other and separated by a short distance, b (the selection of the length of b will be discussed). The global position and orientation of the LDS is known. This is the case since LDS is assumed to be positioned using an accurate measuring device. The displacements from the LDS reference position can be measured and denoted as L_1 and L_2 respectively. From Fig. 3.1, it can be seen that the tangential angle of the curve at the point that the first beam strikes the curve can be measured by

$$\theta = \arctan[(L_2 - L_1)/b] \tag{3.1}$$

The surface is assumed to nearly follow the tangent vector between digitized points. The angle calculated from (3.1) is the amount that the LDS orientation will change for the next digitizing position. The next extrapolation position is calculated using the sampling arc length, s, the angle θ, and the difference between L_1 and the LDS zero displacement distance, L_1. It should be noted that only the measurement made by the first laser scanner will be saved as a surface measurement.

The distance between the two light beams, b, is determined by the maximum curvature of the surface as discussed in Chapter 4. If the maximum curvature is large on a surface, b must be small. Otherwise, the scanner may not be able to follow the surface. Ideally, b is adjustable to accommodate various surfaces and precision requirements.

The concept of the Multiple Beam Approach using three LDS can be explained by the illustration of Fig. 3.2.

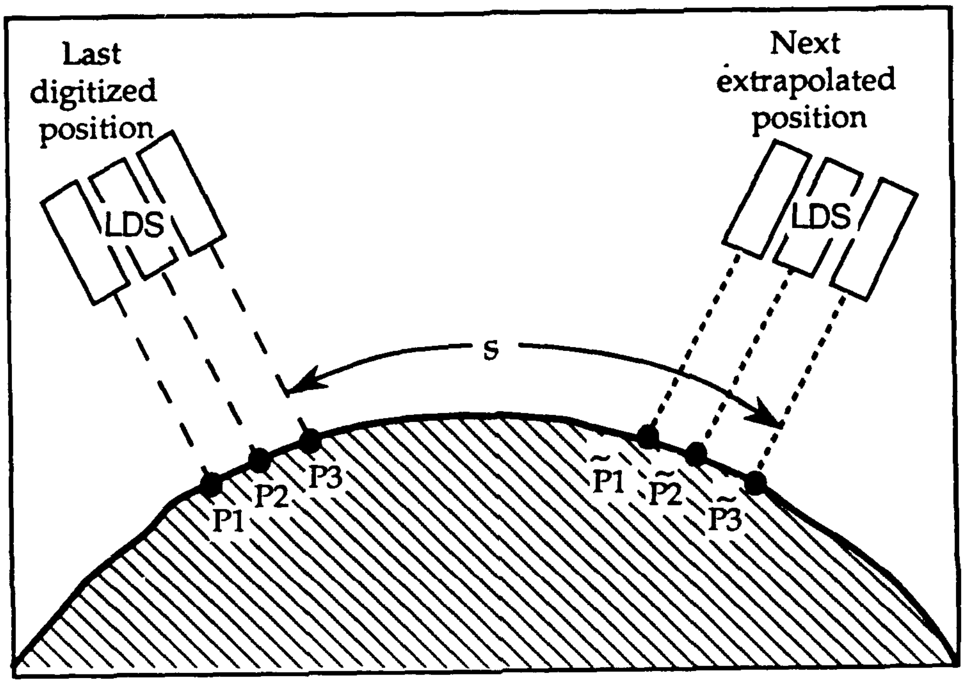
Last digitized position
Next extrapolated position
LDS
LDS
S
P1
P2
P3
$\tilde{P}1$
$\tilde{P}2$
$\tilde{P}3$

Figure 3.2 Multiple Beam Approach - Three LDS

The multiple beam approach using three LDS can measure the surface's local curvature. The three LDS are mounted so that the beams are parallel to each other like in the two beam approach. With the additional LDS, three points can be measured locally on the surface. These three points can determine local curvature by calculating the circle which will pass through these points. This circle is the osculating circle to the curve and has the same curvature as the curve does. The curve is assume to have constant curvature between digitized points and the extrapolated curve follows the osculating circle as shown in Fig. 3.2.

3.2 Extrapolation Approach

The extrapolation approach uses an n^{th} order polynomial to extrapolate the sculptured surface's height and orientation at the next digitizing location. The polynomial has the standard form:

$$z(x) = a_n x^n + a_{n-1} x^{n-1} + \dots + a_1 x + a_0 \tag{3.2}$$

The (n+1) unknown coefficients in the polynomial are solved for by using the previous (n+1) measurements of the sculptured surface. For example, a 2^{nd} order polynomial uses the last three measured surface points to solve for the unknown coefficients a_2, a_1, and a_0. Let $[(x_1,y_1,z_1), (x_2,y_2,z_2)$, and $(x_3,y_3,z_3)]$ represent the three most recently measured points, see Fig. 3.3.

If digitizing in the x axis direction, then y_1, y_2, and y_3 can be all equal. In addition, each point must satisfy Eq. (3.2). Therefore, from Eq. (3.2), the three constraining equations are:

$$z_1 = a_2 x_1^2 + a_1 x_1 + a_0$$

$$z_2 = a_2 x_2^2 + a_1 x_2 + a_0$$

$$z_3 = a_2x_3^2 + a_1x_3 + a_0$$

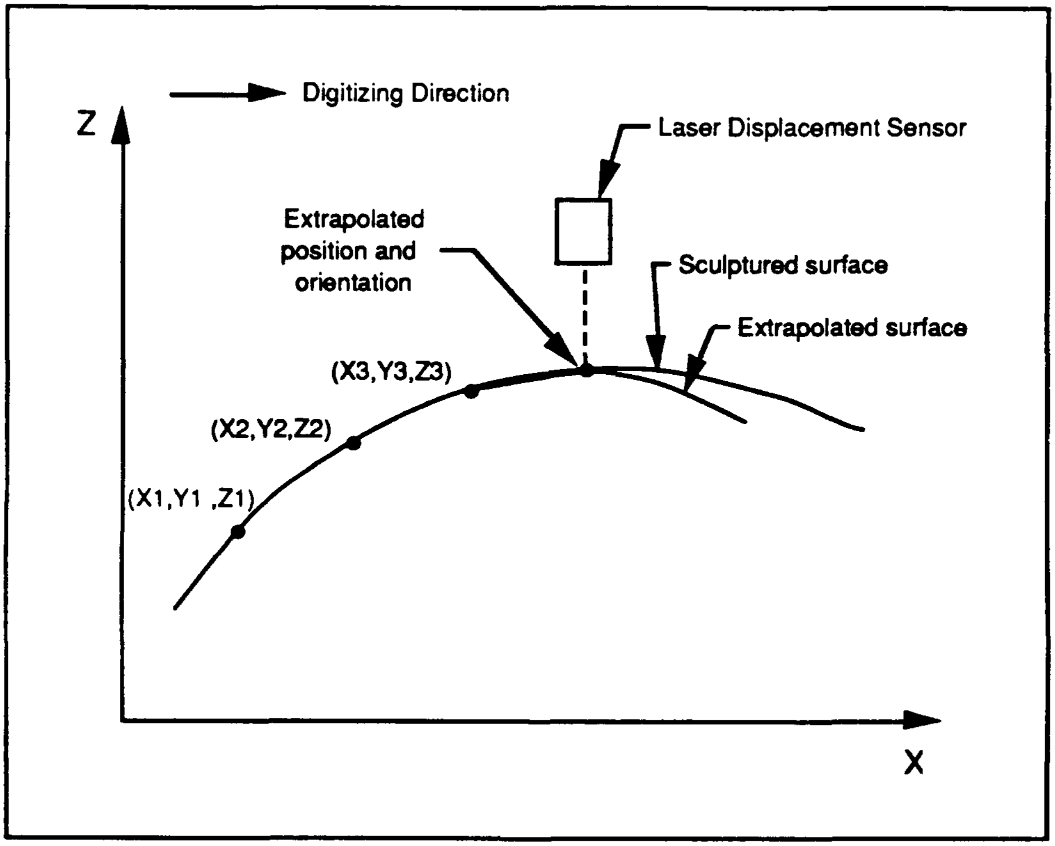
Digitizing Direction
Z
Laser Displacement Sensor
Extrapolated position and orientation
Sculptured surface
Extrapolated surface
(X3,Y3,Z3)
(X2,Y2,Z2)
(X1,Y1 ,Z1)
X

Figure 3.3 2nd Order Polynomial Extrapolation

Once the coefficients are known, Eq. (3.2) can be used to extrapolate the surface's height at the next location to be digitized. Surface orientation can also be extrapolated by evaluating the derivative of Eq. (3.2), see Eq. (3.3).

$$z'(x) = (n)a_nx^{n-1} + (n-1)a_{n-1}x^{n-2} + \dots + a_1 \tag{3.3}$$

Equation (3.3) gives an extrapolated tangent value of the sculptured surface. The orientation of the LDS is set perpendicular to this tangent value. Thus, the laser beam is oriented so that its slope is set equal to the negative inverse of z'. The z axis position for the LDS is calculated by Eq. (3.2). The x axis value for the position was used in Equations (3.2) and (3.3) and is a fixed distance apart from the last measured point. This distance is selected by the operator at run time.

Unfortunately, this extrapolation approach needs "n+1" surface points before it can be implemented. For n=2, three surface points must initially be measured using a different approach before implementing the 2nd order polynomial extrapolation approach. One solution is to use the polynomial extrapolation approach but limit the extrapolation order to the highest order that fits the data collected. Therefore, for n=2, a 0th order polynomial is used to extrapolate the 2nd point, a 1st order polynomial is used to extrapolate the 3rd point, and a 2nd order polynomial is used to extrapolate the remaining points. Note, a 0th order polynomial extrapolates the sculptured surface as a plane with a constant z axis value.

A variation to the approach just described is to use the robots initial orientation when extrapolating the 2nd point. In this case, the sculptured surface is still assumed to be a plane but the plane is assumed to be perpendicular to the initial orientation of the robot. This is a better assumption because the operator would naturally place the robot in a near perpendicular orientation before starting the digitizing process. This variational approach was used in the laboratory to extrapolate the 2nd point. The 3rd point was extrapolated using a 1st order polynomial. And subsequent points were extrapolated using a 2nd order polynomial as described.

Another digitizing location that needs special consideration, is the 1st point on subsequent rows. When the surface has been digitized across the requested x length, the LDS is moved in the y direction and the digitizing resumes in the opposite x direction. The x value, z value and orientation for the first point of the new row is assumed to be the same as the last point of the preceding row, only the y axis value is different. Subsequent points on the new row are extrapolated as they were at the start of the preceding row. Namely, the 2nd point on the row is extrapolated assuming the sculptured surface is a plane perpendicular to the LDS. The 3rd point in the row is linearly extrapolated by using the 1st and 2nd points of the row. All subsequent points in the row are extrapolated using a 2nd order polynomial.

The polynomial extrapolation equations can also be prameterized using the surface arc length between data points as the parameter. Using this approach the arc length between data points is held constant while determining what the next digitizing position should be. A parameterized variation to the extrapolation approaches is used in Chapter IV when developing theoretical limitations of these two approaches. However, the equations develop here were used in the experimental implementation.

3.3 Summary

This chapter outlined the Multiple Beam Approach and the Polynomial Extrapolation Approach. The Multiple Beam Approach uses a set of LDS positioned parallel to each other. The extrapolation curve for this approach is a constant curvature curve (i.e. a circle or a line). The Polynomial Extrapolation Approach uses past digitized points to evaluate a polynomial which passes through these data points. Note that if the polynomial has a near constant curvature at the past digitized points then it will have approximately the same curvature at the next digitized point. The next chapter will evaluate these extrapolation approaches.

CHAPTER IV

EVALUATION OF EXTRAPOLATION APPROACHES

In this chapter, the digitizing error parameters are shown to be bounded functions when using the proposed prediction approaches to digitize an unknown surface which has a finite maximum curvature. These functions can be used to determine an adequate sampling arc length, if the maximum surface curvature is known, or for a given sampling arc length, the maximum surface curvature that can be accurately digitized can be determined.

This chapter will develop as follows. First, a general overview of the digitizing error parameters and surface curvature is presented. Next, any plane curve with finite maximum curvature is shown to be bounded locally by two tangent circles of maximum curvature. Given this local bounding result, the maximum and minimum possible slopes of the curve at a point in this local bounding region is developed. Using these two results, the worst case prediction is then established, and the error parameter functions are derived for this case.

4.1 General Overview

In the multiple beam approach and the polynomial extrapolation approach, the surface is digitized one row at a time where the rows are formed by the intersection of parallel planes with the surface. The intersection of a plane with the surface forms a plane curve. Since the LDS's beam is kept within this intersecting plane while digitizing a row, the objective of these predicting approaches is to extrapolate the plane curve's position and normal vector, see Fig. 3.2. In this evaluation of the extrapolation approaches, the plane curve is assumed to have finite maximum curvature.

There are three error parameters associated with the digitizing process: ρ, θ, and Δs. The first two error parameters, ρ and θ, are a result of limitations associated with the LDS. ρ is the displacement between the LDS reference position and the object's surface. θ is the angle between the laser beam and the surface normal vector, see Fig. 4.1. Both, ρ and θ have bounded values which are specified by the manufacturer. If ρ is too large then the LDS will be out-of-range and the LDS will fail to give a displacement reading. If θ is too large then the LDS will either fail or give inaccurate readings. The last error parameter, Δs, is related to the the sampling arc length. It is the difference between the desired sampling arc length, s, and the actual arc length, $s + \Delta s$, as measured between adjacent digitized points.

Minimizing Δs keeps the sampling arc length uniform which is desirable for later surface reconstruction from the digitized points. This chapter shows that ρ, θ, and Δs are bounded when a surface with finite maximum curvature is digitized using one of the two proposed extrapolation approaches.

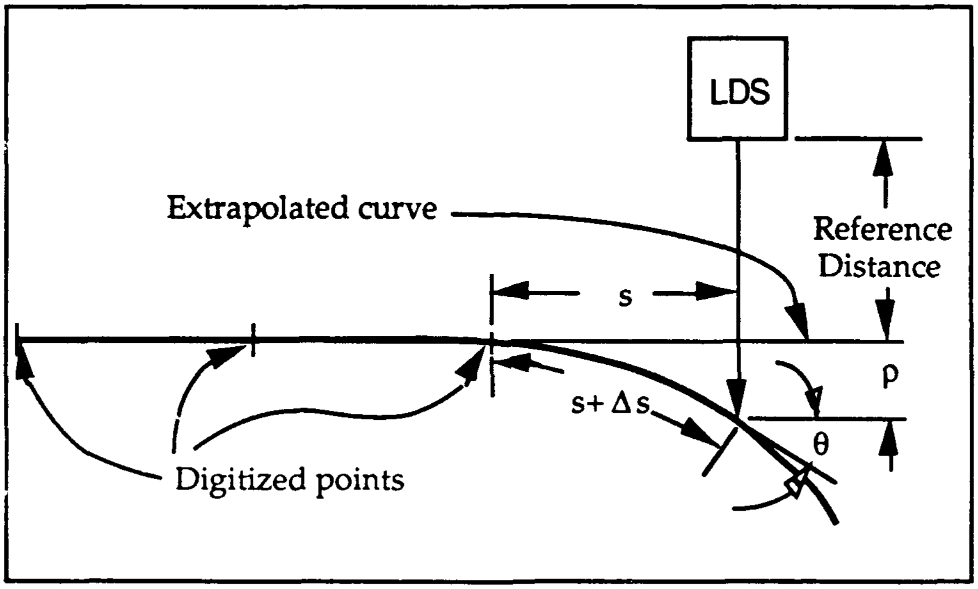
LDS
Extrapolated curve
s
Reference Distance
ρ
s+Δs
θ
Digitized points

Figure 4.1 Digitizing Error Parameters

The curvature, κ, of a plane curve is the absolute value of the rate of change in direction of the unit tangent vector at a point P on the curve as the point P moves along the curve, $\kappa = \left|\frac{d\theta}{ds}\right|$. The curvature can also be written as

$$\kappa = \frac{\left| d^2w/du^2 \right|}{\left[1 + (dw/du)^2\right]^{3/2}}, \qquad (4.1)$$

see Fig. 4.2. The symbols u and w represent orthogonal unit vectors in the plane of the curve. The symbol θ represents the angle between the tangent vector at P on the curve and u.

A circle is a curve which has constant curvature, and its radius, R, is related to the curvature by $R = 1/\kappa$. An osculating circle or circle of curvature is a circle which is tangent to a plane curve, lies on the concave side of the curve, and has the same curvature as the plane curve at the point of intersection [1].

4.2 A Plane Curve With Finite Max. Curvature is Bounded Locally

Theorem 4.1:

> A plane curve which is known to have a finite maximum curvature, κ_m, and to pass through the point, P_o, with a tangent vector, T_o, is bounded locally by two tangent circles with radii, R, where $R = 1/\kappa_m$, see Fig. 4.2. A sufficient condition for locality is $|s| \leq \frac{\pi}{2} R$ where s is the curve's arc length measured from the point P_o. The curve will not cross into these tangent circles as long as the arc length satisfies this condition.

Proof:

Let {u,w} be an orthogonal reference frame in the plane of the curve with its origin located at an arbitrary point P_o, and its principle axis, u, directed along the tangent vector, T_o, see Fig. 4.2.

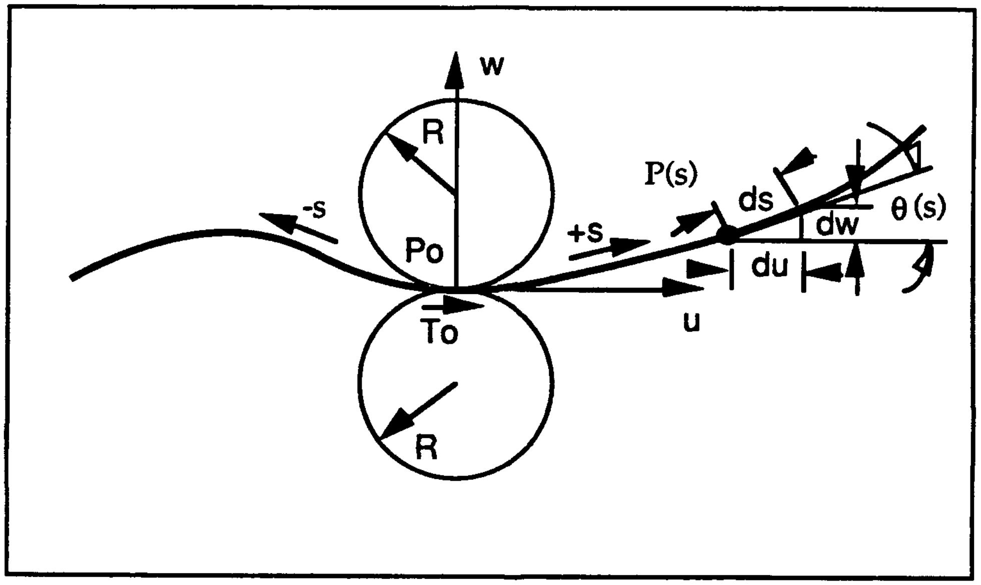

Figure 4.2 A Plane Curve and Bounding Tangent Circles

Given that the curvature is bounded so that $\kappa(s) = \left|\frac{d\,\theta(s)}{ds}\right| \leq \kappa_m$, the angle θ(s) is bounded by

$$\theta(s) = \int_0^s \frac{d\,\theta(\tau)}{d\tau}\,d\tau \leq \int_0^s \kappa_m \cdot d\tau = \kappa_m s. \tag{4.2}$$

where s is the arc length of the curve measured from P_o.

The differential positions along the curve are

$$du = \cos\{ \theta(s) \} \; ds,$$

and

$$dw = \sin\{ \theta(s) \} \; ds. \tag{4.3}$$

Therefore, positions on the curve, P(s) = {u(s), w(s)} are calculated as

$$u(s) = \int_0^s \cos\{ \theta(\tau) \} \; d\tau. \tag{4.4}$$

$$w(s) = \int_0^s \sin\{ \theta(\tau) \} \; d\tau. \tag{4.5}$$

Given the constraint on $\frac{d\,\theta(s)}{ds}$, corresponding bounds on u(s) and w(s) can be determined. u(s) is seen to be maximized, if $\theta(s) = 0$, which gives $u(s)_{max} = s$. u(s) is minimized and extreme values for w(s) are found by maximizing $\theta(s)$ until the value $\frac{\pm\pi}{2}$ is reached. This is done by holding $\frac{d\,\theta(s)}{ds}$ constant at its maximum value of $\pm\kappa_m$ for $|s| \leq \frac{\pi}{2\kappa_m}$. This results in $\theta(s) = \pm\kappa_m s$. Using this value for $\theta(s)$,

$$u(s)_{min} = \frac{1}{\kappa_m}\sin(\kappa_m s), \tag{4.6}$$

$$w(s)_{min} = \frac{-1}{\kappa_m}(1-\cos(\kappa_m s)), \tag{4.7a}$$

and

$$w(s)_{max} = \frac{+1}{\kappa_m}(1-\cos(\kappa_m s)). \tag{4.7b}$$

Thus, given an arc length $|s| \leq \frac{\pi}{2\kappa_m} = s_m$, the position, P(s), of the curve at s_1 is bounded by one of two rectangles depending on whether s_1 is positive or negative. These rectangles are formed by the the bounds on $u(s_1)$ and $w(s_1)$.

For $0 < s_1 \leq \frac{\pi}{2\kappa_m}$,

$$\frac{1}{\kappa_m}\sin(\kappa_m s_1) \leq u(s_1) \leq s_1, \text{ and} \tag{4.8}$$

$$\frac{-1}{\kappa_m}(1-\cos(\kappa_m s_1)) \leq w(s_1) \leq \frac{1}{\kappa_m}(1-\cos(\kappa_m s_1)). \tag{4.9}$$

For $\frac{-\pi}{2\kappa_m} \leq s_1 < 0$,

$$s_1 \leq u(s_1) \leq \frac{1}{\kappa_m}\sin(\kappa_m s_1), \text{ and} \tag{4.10}$$

$$\frac{-1}{\kappa_m}(1-\cos(\kappa_m s_1)) \leq w(s_1) \leq \frac{1}{\kappa_m}(1-\cos(\kappa_m s_1)). \tag{4.11}$$

A graphical representation of these boundaries when $s = s_1$ is shown in Fig. 4.3.

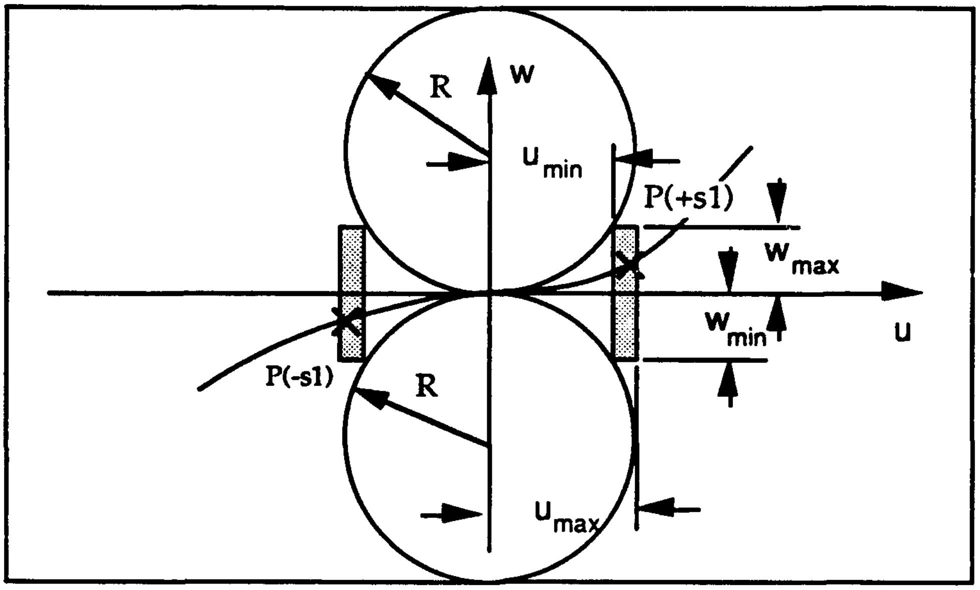

Figure 4.3 Bound on Local Curve Points.

Eliminating s_1 from (4.8), (4.9), (4.10), and (4.11) results in the following equations

$$u^2 + (w + 1/\kappa_m)^2 = (1/\kappa_m)^2,$$

and

$$u^2 + (w - 1/\kappa_m)^2 = (1/\kappa_m)^2. \tag{4.12}$$

These are the equations of two circles with radii, $R = 1/\kappa_m$, which are tangent to the curve at the point P_o. Because these boundary equations hold for all values of $|s| \leq s_m$, the curve is known to be bounded locally between two tangent circles, inclusively. The resulting locally bounded region which is known to contain the plane curve for $|s| \leq s_m$ is shown in Fig. 4.4.

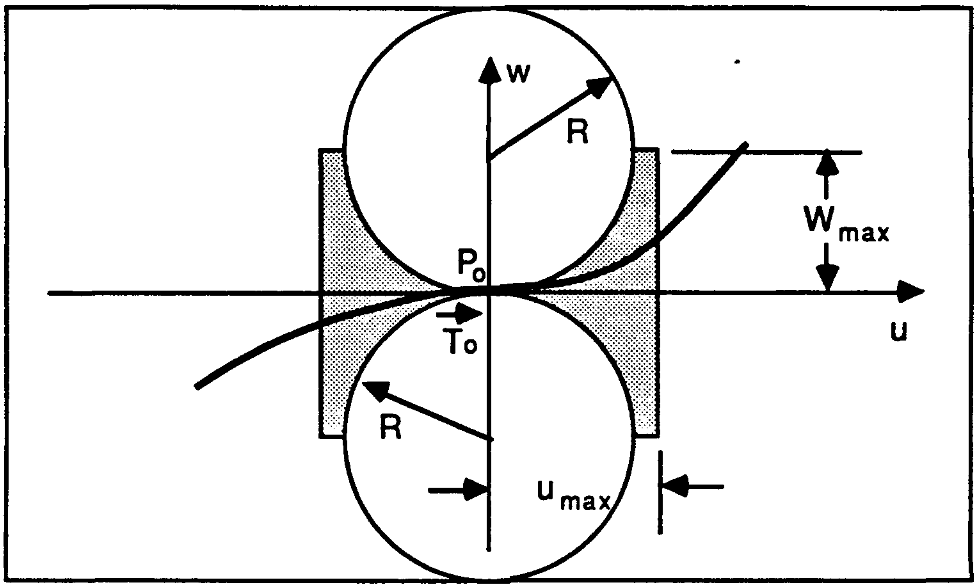

Figure 4.4 Locally Bounded Region

Thus, a plane curve with maximum curvature, κ_m, which passes through the point P_0 and has a tangent vector in the direction of T_0, is bounded locally by two tangent circles with radii, R, where $R = 1/\kappa_m$.

QED.

As a corollary to Theorem 4.1, the sharpest turn that a plane curve with a finite maximum curvature, κ_m, can make is to follow an osculating circle with radius $R=1/\kappa_m$. This result will be used to determine the worst case for the extrapolation approaches.

4.3 A Curve's Slope Is Bounded In The Locally Bounded Region

Suppose the following four things are known about a plane curve: 1) It has a finite maximum curvature, 2) It passes through the point P_0, 3) It has a known tangent vector, T_0, at the point P_0, and 4) It passes through the point P_2 where P_2 is located in the locally bounded region of Theorem 4.1. With these constraints, the slope of the curve at the point P_2 is known to be bounded, see Fig. 4.5. Because of symmetry, only the case where $u > 0$ will be considered. The path that the two limiting curves take will now be described.

Picture that you are on top of the curve at point P_0 and are "driving" it in the positive arc length direction (i.e. in the direction of T_0). The curve with the largest slope, ml, at the point P_2 starts out by following a constant maximum curvature curve to the right (i.e. the lower boundary circle) and then switches to following a constant maximum curvature curve to the left to reach the point P_2, see Fig. 4.5. The curve with the smallest slope, m_s, at the point P_2, starts out by following a constant maximum curvature curve to the left (i.e. the top boundary circle) and then switches at an appropriate place to following a constant maximum curvature curve to the right before passing through the point P_2. Note, that the values of ms and ml are functions of the location of P_2. However, any curve which satisfies theses four constraints is bounded locally (i.e. between the point P_o and P_2) by these two extreme curves and has a slope, m, at the point P_2 which is bounded by $m_s \leq m \leq m_l$. Also note, if the point P_2 lies on the top boundary circle, then ms = ml, and both curves simply follow the top boundary circle from the start. And similarly, if the point P_2 lies on the bottom boundary circle, then ms = ml, and both curves follow the bottom boundary circle to get to the point P_2.

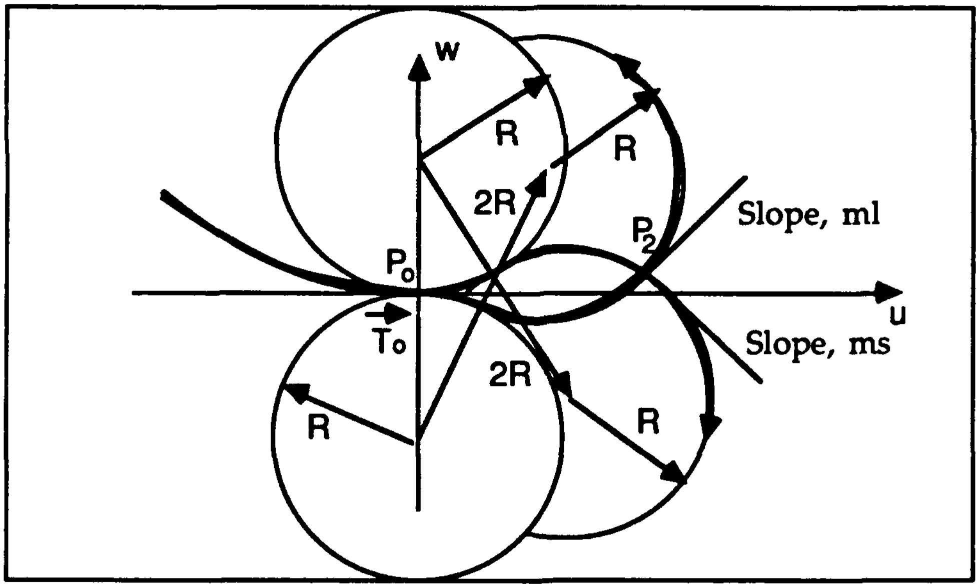

Figure 4.5 Bound on Local Slope Values.

To determine the worst possible orientation that the plane curve might have with the LDS's beam, maximum and minimum slope values will be calculated for points along a line which crosses the locally bounded region. This line represents the LDS's beam and it intersects the origin of the lower tangent circle while forming an angle, γ, with the w axis, see Fig. 4.6.

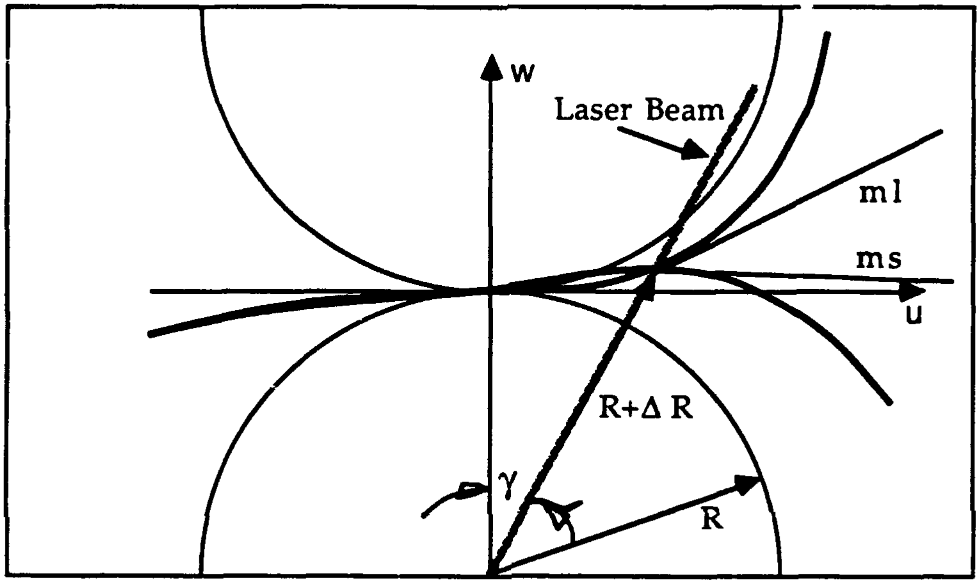

Figure 4.6 Extreme LDS Beam Orientation

This would be a reasonable position and orientation for the LDS's beam, if the curve had previously (i.e. for $s \leq 0$) followed this lower circle.

The minimum slope and maximum slope are functions of γ, and $\Delta R/R$ and ΔR is the distance along the laser beam from intersection with the lower bounding circle to the point P_2. Due to geometry constraints, γ is bounded by

$$0 < \gamma \leq \frac{\pi}{6} \tag{4.13a}$$

(i.e. for $\gamma > \frac{\pi}{6}$, the laser line will not intersect the top circle). The ratio $\frac{\Delta R}{R}$ is bounded by

$$0 \leq \frac{\Delta R}{R} \leq (2\cos(\gamma) - \sqrt{4\cos^2(\gamma)-3} - 1). \tag{4.13b}$$

The upper bound, R $(2\cos(\gamma) - \sqrt{4\cos^2(\gamma)-3} - 1)$, is the distance along the laser beam from intersection with the lower bounding circle to the upper bounding circle. Because the curve is known to be bounded by these two circles, this distance represents the largest possible $\frac{\Delta R}{R}$ value for a given γ value.

The maximum slope, ml, and minimum slope, ms, values of Fig. 4.5 and Fig. 4.6 can be determined for all points along the laser beam line between these two bounding circles. Finding the maximum values for these values will determine the worst possible orientation the LDS will have with the curve. The position of the point where the maximum and minimum slope values are calculated is a function of $\frac{\Delta R}{R}$ and γ.

Therefore, the maximum slope as a function of $\frac{\Delta R}{R}$ and γ is found by first solving and normalizing the triangle in Fig. 4.7 and then finding the slope of the curve. The max. slope function is

$$m_l = \tan(B + C - \gamma) \tag{4.14}$$

where

$$B = \cos^{-1}\left\{1 + \frac{1}{2}\frac{\Delta R}{R} + \frac{-1}{4}\left(\frac{\Delta R}{R}\right)^2\right\}, \tag{4.14a}$$

$$C = \cos^{-1}\left\{\frac{1 + \frac{1}{2}\frac{\Delta R}{R} + \frac{1}{4}\left(\frac{\Delta R}{R}\right)^2}{1 + \frac{\Delta R}{R}}\right\}. \tag{4.14b}$$

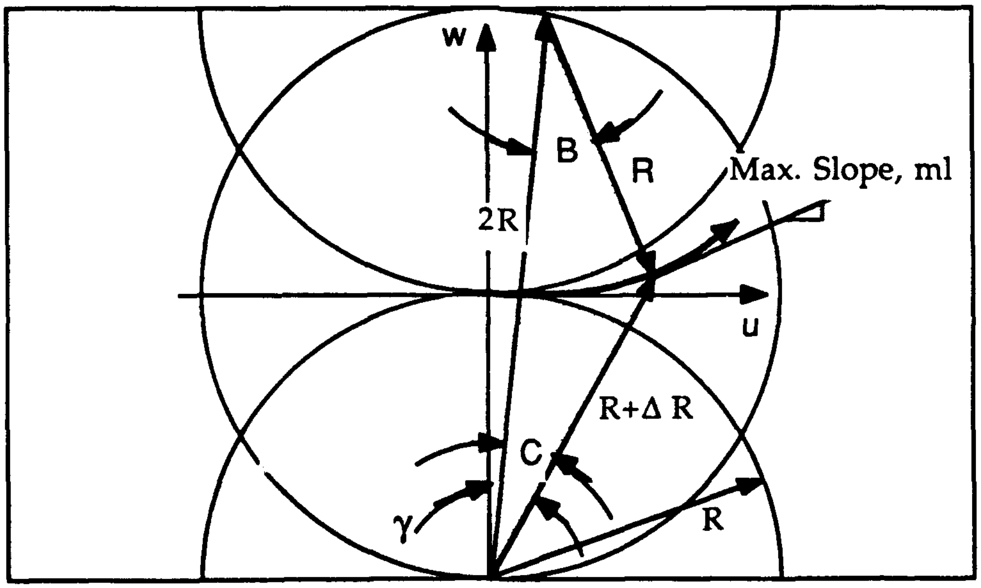

Figure 4.7 Maximum slope Curve Showing Angles {B, C}

The minimum slope as a function of $\frac{\Delta R}{R}$ and γ is found by first solving and normalizing the two triangles in Fig. 4.8 and then finding the slope of the curve. The minimum slope function is

$$m_s = \tan(A - D - F) \tag{4.15}$$

where

$$A = \cos^{-1}\left\{\frac{3 + \left(\frac{x}{R}\right)^2 - 2\frac{\Delta R}{R} - \left(\frac{\Delta R}{R}\right)^2}{4\frac{x}{R}}\right\}. \tag{4.15a}$$

$$D = \cos^{-1}\left\{\frac{3 + \left(\frac{x}{R}\right)^2}{4\frac{x}{R}}\right\}, \tag{4.15b}$$

$$F = \cos^{-1}\left\{\frac{5}{4} + \frac{-1}{4}\left(\frac{x}{R}\right)^2\right\}, \tag{4.15c}$$

and

$$\frac{x}{R} = \sqrt{\left(5 + 2\frac{\Delta R}{R} + \left(\frac{\Delta R}{R}\right)^2 + \left(-4 - 4\frac{\Delta R}{R}\right)\cos(\gamma)\right)}. \tag{4.15d}$$

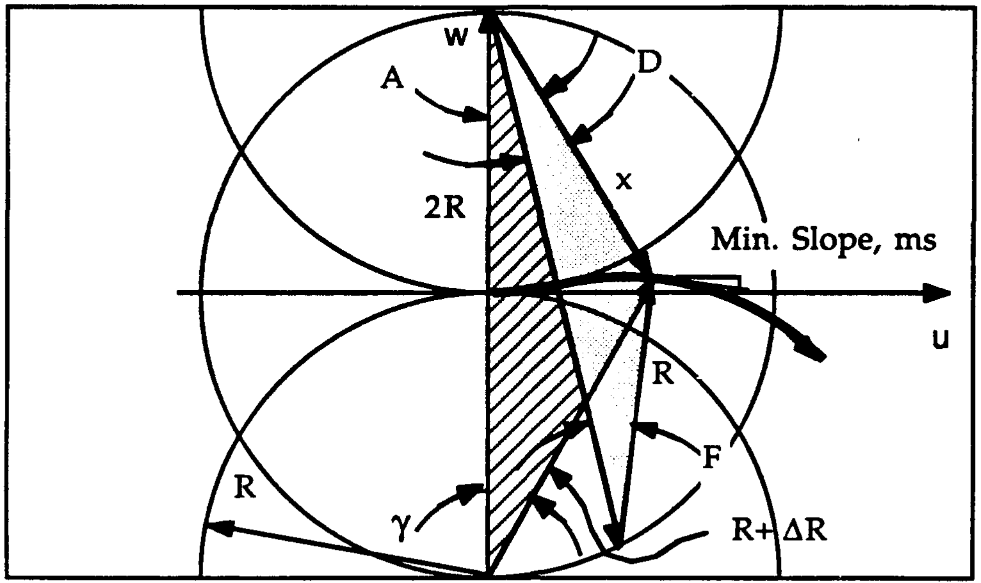

Fig. 4.8 Min. Slope Curve Showing Angles {A, D, F} and Side x.

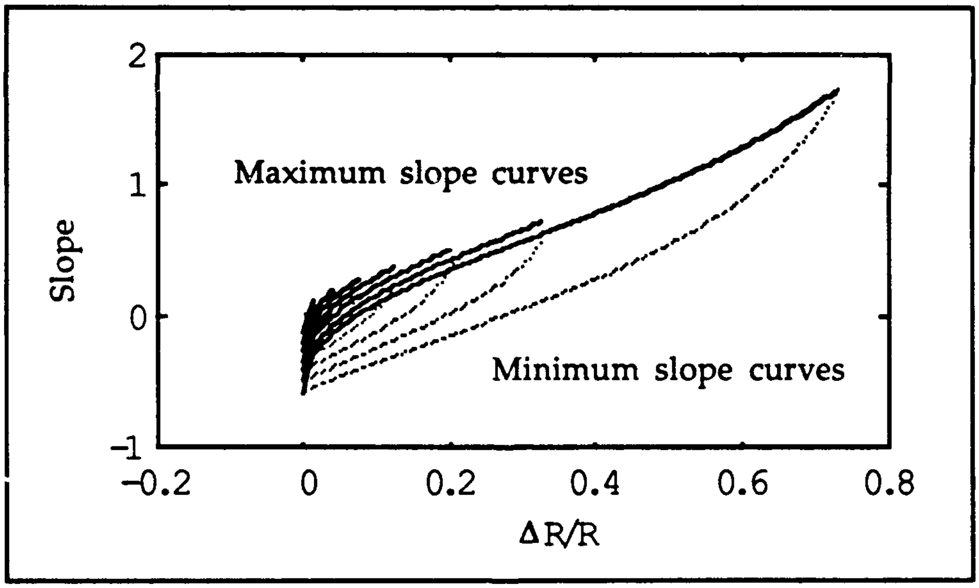

Figure 4.9 Extreme Slope Curves as a function of $\frac{\Delta R}{R}$ with LDS Orientation, γ, Held Constant. From left to right, γ is $\{\frac{1}{4}\frac{\pi}{6}, \frac{3}{8}\frac{\pi}{6}, \frac{1}{2}\frac{\pi}{6}, \frac{5}{8}\frac{\pi}{6}, \frac{3}{4}\frac{\pi}{6}, \frac{7}{8}\frac{\pi}{6}, \frac{\pi}{6}\}$.

The plots of (4.14) and (4.15) slope for seven different γ values as a function of $\frac{\Delta R}{R}$ are shown in Fig. 4.9. As can be seen from these plots, the max/min slope functions are monotonically increasing. At $\frac{\Delta R}{R} = 0$, the curve is perpendicular to the LDS's beam. However, as $\frac{\Delta R}{R}$ increases the inclination angle between the curve and the laser beams increases. Thus, the worst inclination occurs, (i.e. θ is maximized) when the curve follows the top tangent circle. The other error parameters, ρ and Δs, are also maximized under this condition. Fig. 4.9 also shows that the maximum errors are decreased as the angle γ decreases. Since γ is proportional to the sampling arc length, the maximum errors decrease as the sampling arc length is decreased.

4.4 Worst Extrapolation Case

Both the multiple beam approach using three LDS and the 2nd order polynomial approach (which uses one LDS) have the same worst case performance when digitizing a surface with a finite maximum curvature. These two approaches are comparable, because they both approximate the surface's local curvature. In contrast, a multiple beam approach using two LDS can only approximate the surface's local tangent. The reason both methods can approximate the surface's local curvature is that both methods use three local digitized points.

As discussed, the error parameters (θ, ρ, and Δs) for these approaches are found to be monotonic functions of the sampling arc length. Because the leading LDS has the largest sampling arc length out of the three LDS, it also has the largest error parameters. Both extrapolation approaches have the same worst case error parameters, because, both will predict the same worst case curve to follow. This happens if the leading LDS is positioned at the point of inflection where the curve has been following a constant positive maximum curvature and then switches to following a constant negative maximum curvature, or vice versa. This situation results in the maximum error between the predicted position and orientation for the LDS and the ideal position and orientation for the LDS, see Fig. 4.10.

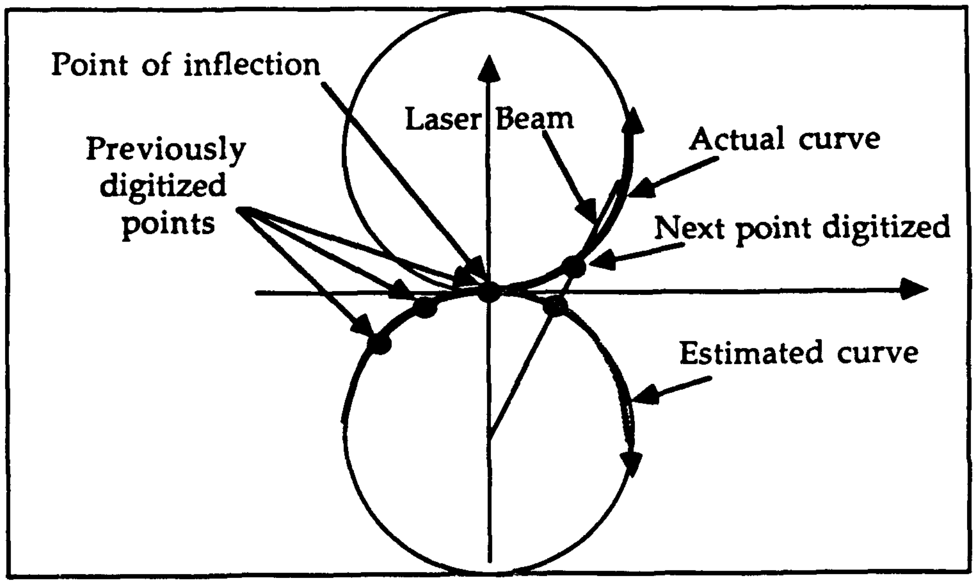
Point of inflection
Laser Beam
Actual curve
Previously digitized points
Next point digitized
Estimated curve

Figure 4.10 Worst Case Curve Estimation.

The maximum error parameter values can be minimized by using a linear extrapolation approach (i.e. a two-laser multiple beam approach or a 1st order polynomial approach). In this approach, the extrapolation curve would be a line parallel to T_0 which passes through P_0. This puts the extrapolation curve in the middle of the locally bounded region. This approach would be the best if there was rarely any correlation between the curve's curvature to be digitized (the extrapolated curvature) and the curve's curvature previously measured. More commonly, however, the curve's curvature is near constant over several consecutive digitized points. Using this constant curvature assumption, the average error parameter values would be smaller than in using a linear approximation, however, the maximum error values could be larger.

4.5 Deriving Error Parameter Functions

Extreme values for the error parameters (θ, ρ, and Δs) will now be calculated as functions of the ratio of sampling arc length to radius of maximum curvature. These values are based on the assumption that the plane curve being digitize has a bounded maximum curvature. As discussed, a curve with finite maximum curvature is known to be bounded locally by the two extreme osculating circles. The error parameters all have their largest values if the estimated curve follows one osculating circle but the actual curve follows the other osculating circle.

Because of symmetry, the maximum error values are the same regardless as to which circle is the estimated curve and which is the actual curve or which side the curve is being digitized on. For arguments sake, the osculating circle on the right is assumed to be the estimated curve and the osculating circle on the left is assumed to be the actual curve. This estimation curve is reasonable if the plane curve had been following a constant maximum curvature curve, see Fig. 4.10. This estimation curve will cause the LDS to be positioned and oriented in relation to the actual curve so that the error parameters are maximized.

4.5.1 Relationship Between Δs/R and s/R

The error parameter Δs is the difference between the desired sampling arc length and the actual sampled arc length, see Fig. 4.11.

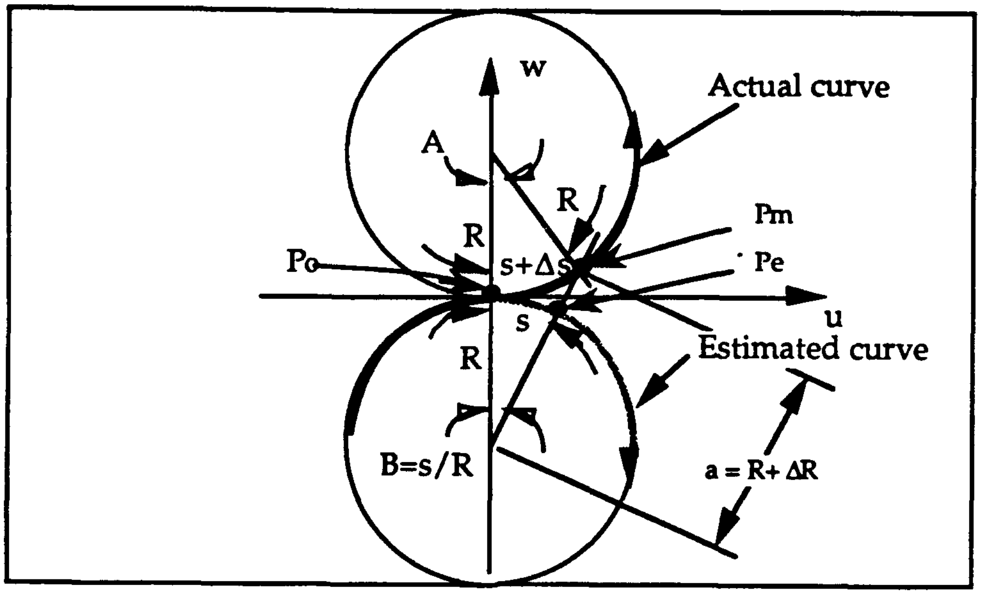

Figure 4.11 Measured Curve's Arc Length.

Under worst case conditions, the LDS will be positioned at the point Pe, a distance s along the lower circle from the last measured point Po, and will be oriented so that the laser points towards the center of this circle. The actual point measured, Pm, will be the intersection of this "laser" line and the tangent circle on the left. Using the law of cosines, the law of sines, and trigonometric identities, the relating equation is

$$\frac{\Delta s}{R} = \frac{-s}{R} + \sin^{-1}\left\{\sin\left(\frac{2s}{R}\right) - \sin\left(\frac{s}{R}\right)\sqrt{\left(2\cos\left(\frac{2s}{R}\right)-1\right)}\right\} \qquad (4.16)$$

where $0 < \frac{s}{R} < \frac{\pi}{6}$.

The bound on $\frac{s}{R}$ is the result of the problem's geometry. If the ratio of arc length to radius is greater that $\frac{\pi}{6}$ then the LDS might not measure the actual curve at all. This is the same geometry constraint that bounded γ in (4.13a). A plot of $\frac{\Delta s}{R}$ as a function of $\frac{s}{R}$ is shown in Fig. 4.12.

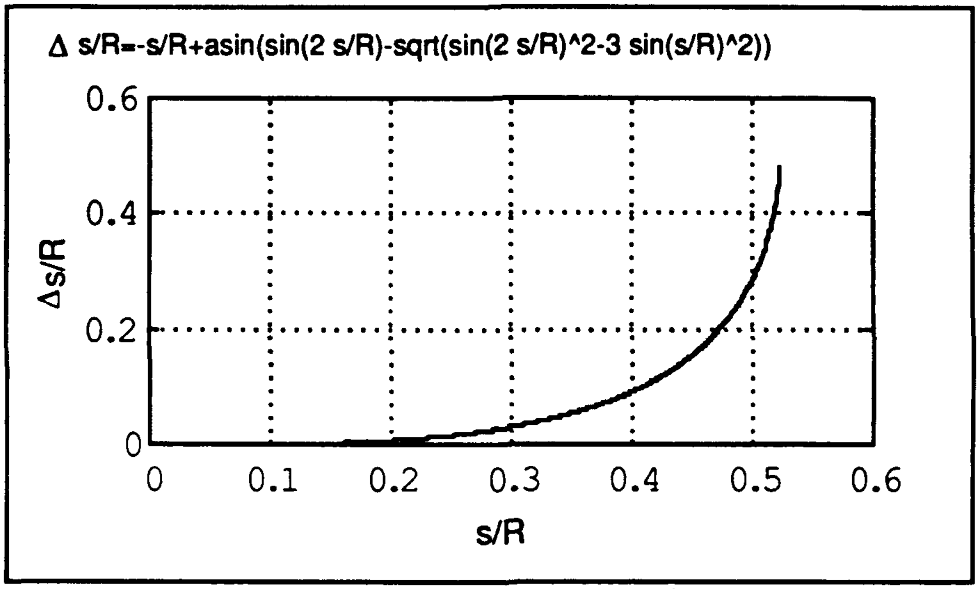

Figure 4.12 Plot of Error Parameter $\frac{\Delta s}{R}$ as a function of normalized sampling arc length, $\frac{s}{R}$

4.5.2 Relationship Between ρ/R and s/R

The displacement in a LDS is measured from the reference zero position along the laser beam's projection (line of sight of the LDS) to the object's surface. As discussed, the reference zero position is placed on the estimated curve. Thus, the displacement, ρ, is the distance between the estimated curve and the actual curve as measured along the LDS's line of sight. This value normalized by the radius of maximum curvature is found directly from using the law of cosines. The equation is

$$\frac{\rho}{R} = 2\cos\left(\frac{s}{R}\right) - 1 - \sqrt{\left(2\cos\left(\frac{2s}{R}\right) - 1\right)} \tag{4.17}$$

where $0 < \frac{s}{R} < \frac{\pi}{6}$.

The plot of (4.17) is shown in Fig. 4.13.

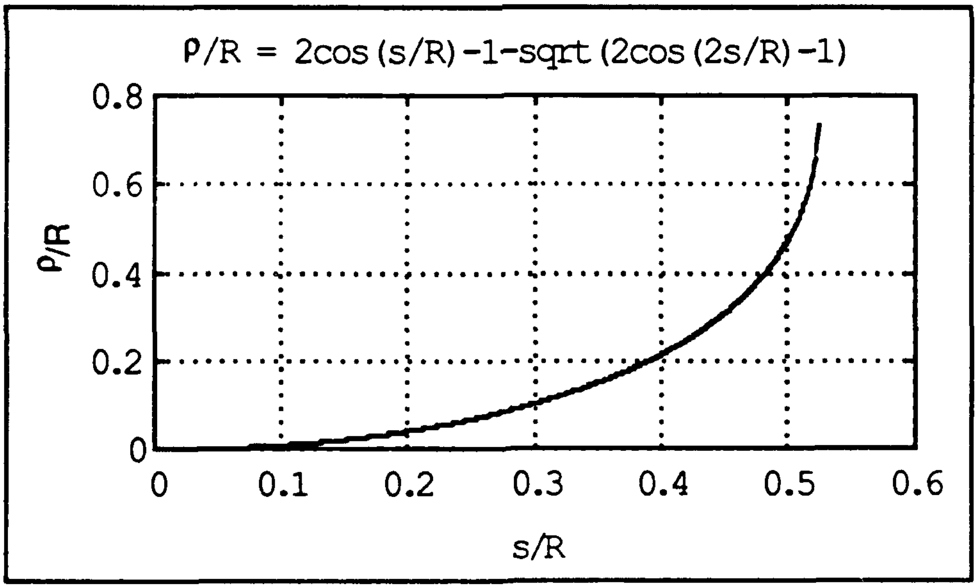

Figure 4.13 Plot of Error Parameter $\frac{\rho}{R}$ as a Function of Sampling Arc Length, $\frac{s}{R}$.

4.5.3 Relationship Between θ and s/R

The angle, θ, is the angle between a normal vector at point Pm and a vector parallel to the line of sight of the LDS. Thus, the cos(θ) is equal to the inner product of these two unit vectors. Using this result and substituting the right hand side of (4.16) for $\frac{\Delta s}{R}$, the relating equation is

$$\theta = \frac{s}{R} + \sin^{-1}\left\{ \sin\left(\frac{2s}{R}\right) - \sin\left(\frac{s}{R}\right) \sqrt{\left(2\ \cos\left(\frac{2s}{R}\right) - 1\right)} \right\} \qquad (4.18)$$

where $0 < \frac{s}{R} < \frac{\pi}{6}$.

The plot of θ as a function of $\frac{s}{R}$ is shown in Fig. 4.14 and a composite plot of figures 4.12, 4.13, and 4.14 is shown in Fig. 4.15.

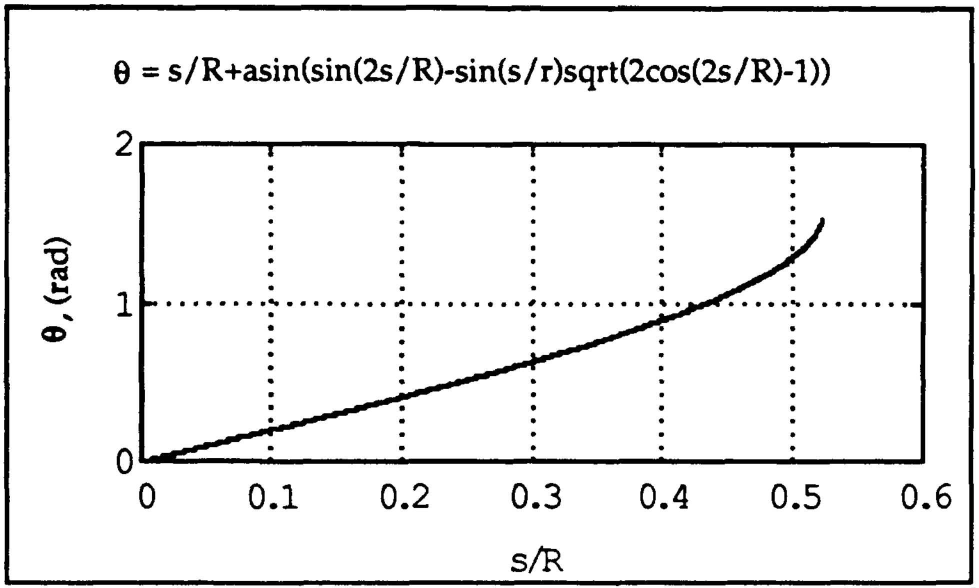

Figure 4.14 Plot of Error Parameter θ as a Function of Sampling Arc Length, $\frac{s}{R}$

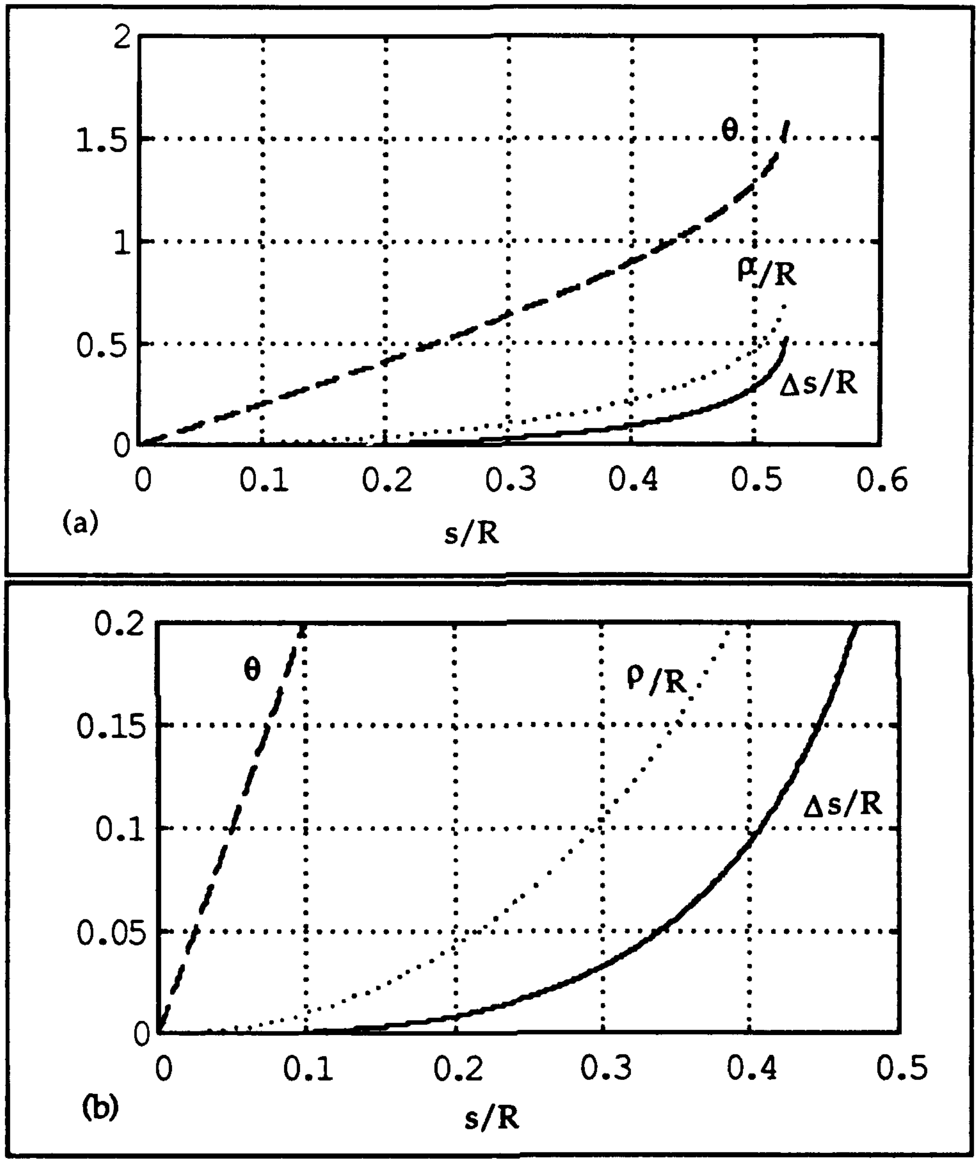

Figure 4.15 Composite Plot of Error Paramters as a Function of Sampling Arc Length

Figure 4.15 (Continued)

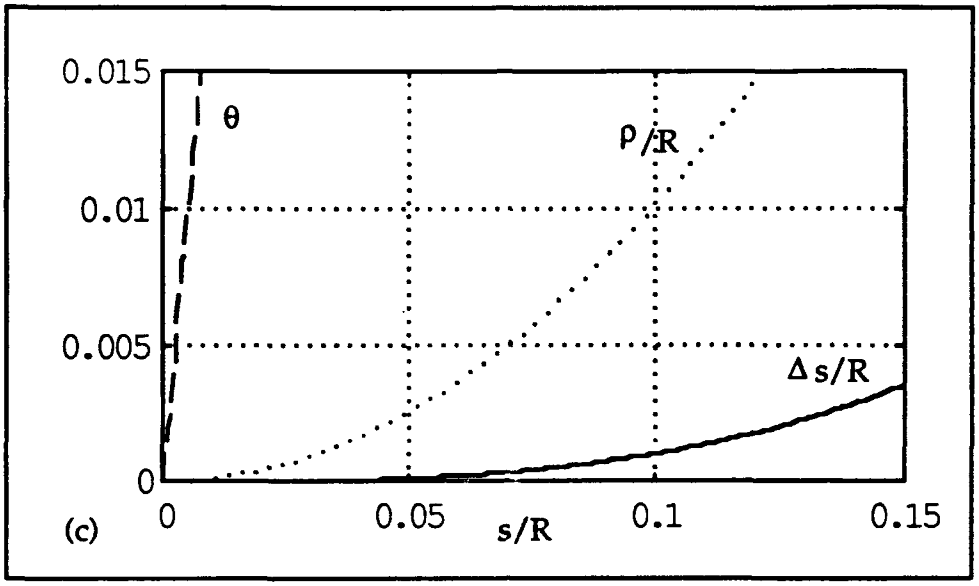

4.6 An Example Of Calculating The Sampling Arc Length

The error parameter plots in Fig. 4.15 can be used to select the ratio of sampling arc length to radius of maximum curvature, $\Delta s/R$, that will bound the error parameters within a desired range.

For example, suppose the desired bound on the error parameters is as follows: $|\theta| < 12^\circ \approx 0.21$ radians, $|\rho| < 10$ mm, and $|\Delta s| < 0.05s$. The last inequality restricts the actual sampled arc length to be within 5% of the estimated arc length. Suppose, further that the maximum radius of curvature of the surface is $R = 4$ mm. As seen from Fig. 10, for the error parameter, θ, to be bounded so that $|\theta| < 0.21$ rad, then the inequality $\frac{s}{R} \leq 0.1$ must be satisfied. Likewise, for $\frac{\rho}{R}$ to be bounded so that $\left|\frac{\rho}{R}\right| < 10/4 = 2.5$, then the inequality $\frac{s}{R} < \frac{\pi}{6}$ must be satisfied (this is the maximum possible value $\frac{s}{R}$). And finally, for $\left|\frac{\Delta s}{R}\right| < 0.01\frac{s}{R}$ to be true $\frac{s}{R} < 0.2$ must be satisfied. Consequently, selecting $\frac{s}{R} = 0.1$ will satisfy all three inequalities. Therefore, if $s = 0.1\ R = 0.4$ mm is used as the estimated arc length value, then the error parameters are bounded as follows: $|\theta| \leq 0.2$ rad $\approx 11^{\circ}$, $|\rho| \leq 0.01R = 0.04$ mm, and $|\Delta s| < 0.001R = 0.004$ mm. This will always be true so long as the estimated curve is selected so that its maximum curvature less than or equal to the maximum curvature of the digitized curve (i.e. $R \leq 4$ mm).

The error parameter plots in Fig. 4.15 can also be used to determine the limitations on the surface to be digitize if given a particular sampling arc length and LDS's limitations. Thus, if a sampling arc length of 0.4mm is used and if the LDS has the limitations that $|\theta| < 12^{\circ} \approx 0.21$ radians, and $|\rho| < 10$ mm, then the surface curvature must be larger than 1/(4mm) to be sure that the measurement readings are accurate.

4.7 Summary

This chapter evaluated how well the extrapolation approaches work in digitizing an unknown surface which has a finite maximum curvature. The error parameters (θ, ρ, and Δs) were defined. They were found to be bounded functions of the ratio of sampling arc length to radius of maximum curvature. These functions were derived by identifying the worst prediction case. The two extrapolation approaches were shown to have the same bounded error parameter functions. The worst extrapolation case was determined by using the result that a plane curve which has a finite maximum curvature is bounded locally by two tangent circles with maximum curvature. The bounding error parameter functions can be used to determine a sampling arc length that will keep the error parameters within desired bounds. They can also be used to determine the maximum surface curvature which can be accurately digitized given a particular sampling arc length and LDS limitations.

CHAPTER V

EXPERIMENTAL SYSTEM

This chapter presents the digitizing system which was constructed in the laboratory to demonstrate and evaluate the proposed extrapolation approaches. The overall requirements and architecture of the system are first presented. This is followed by a discussion of the controlling software. Lastly, the nonlinear position accuracy of rotary joint robots is illustrated with two examples.

5.1 System Architecture

The digitizing system implemented to study the proposed extrapolation approaches needed to meet several requirements. The system had to be capable of positioning and orienting the LDS with a reasonable degree of accuracy. The implementation of the extrapolation approaches required a computation and a control unit that could accept the output from the LDS, control the re-positioning of the LDS, and record collected data. Finally, the equipment had to be chosen from what was on hand (where possible) due to budget constraints.

The digitizing system that was constructed consisted of two Laser Displacement Sensors, a six degrees-of-freedom PUMA robot, and an IBM PC, see Fig. 5.1.

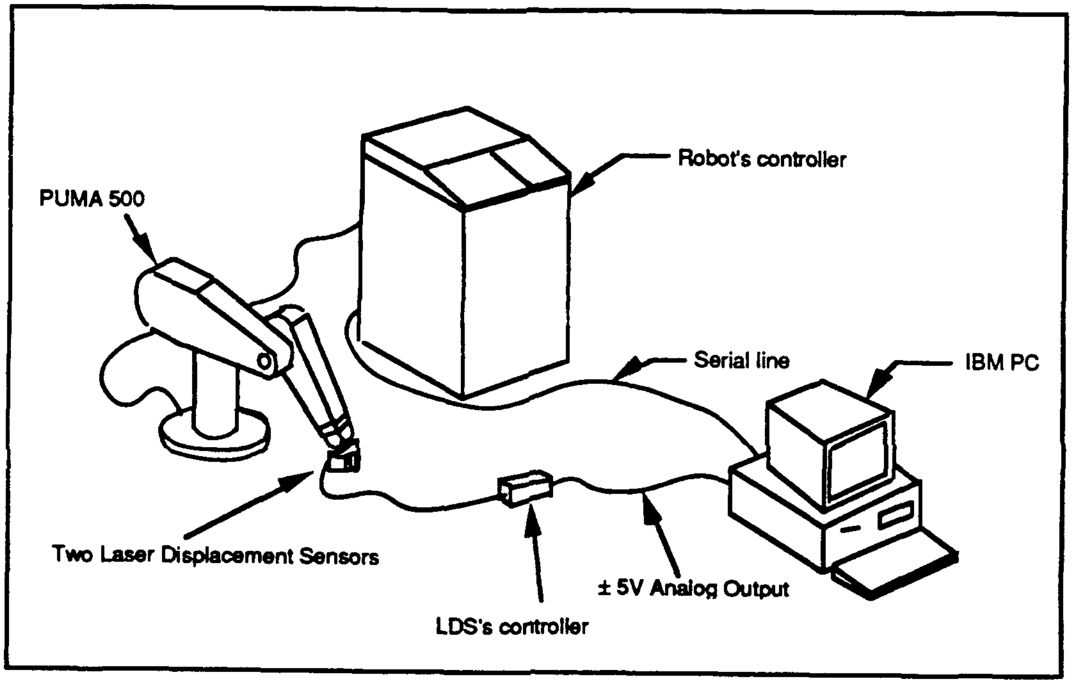
Robot's controller
PUMA 500
Serial line
IBM PC
Two Laser Displacement Sensors
± 5V Analog Output
LDS's controller

Figure 5.1 Major Components in Digitizing System

A fixture mounted on the robot's end-effector holds the two LDS and positions their beams parallel to each other and separated by a distance of 17.85 mm. The analog ± 5 volt output of the two LDS is converted to a digital value by a MetraByte DAS-8 board in the IBM PC. The IBM PC communicates to the PUMA robot's controller via a serial port. As needed, the control software on the IBM PC requests the robot's current position and directs the robot to move. The control software uses the LDS data and the robots position-orientation information to determine data points on the sculptured surface. These data points are then used to implement the multiple beam approach or the polynomial extrapolation approach described above.

Selected specifications on the major hardware components are listed in Table 5.1.

Table 5.1 Selected Hardware Specifications

- Keyence LB-72/LB-12: Laser Displacement Sensor
  - Stand-off distance: 40 mm
  - Measurement range: ± 10 mm
  - Resolution: ± 0.015 mm (Object: white paper at a distance of 40mm, at 2ms)
  - Linearity: 1% of the displacement (Object: white mat paper, tilted ± 30°)
- PUMA Mark III 500 Series Robot
  - 6 axes of rotation,
  - 914 mm (3.0 ft) reach range,
  - Position Repeatability ± 0.1 mm (± 0.004 in)
- IBM PC
  - 4.77 MHz clock speed
- MetraByte DAS-8: Data Acquisition Board
  - ± 5 volt, 12 bit Analog to Digital Converter

5.2 System Software

The control software was made up of several low level and high level modules. The low level modules include: Serial communication, Screen memory management, and data acquisition. The high level modules include: protocol to communicate with robot's controller, terminal emulation mode, digitizing mode, and a stand alone user program running on the robot's controller, see Fig. 5.2.

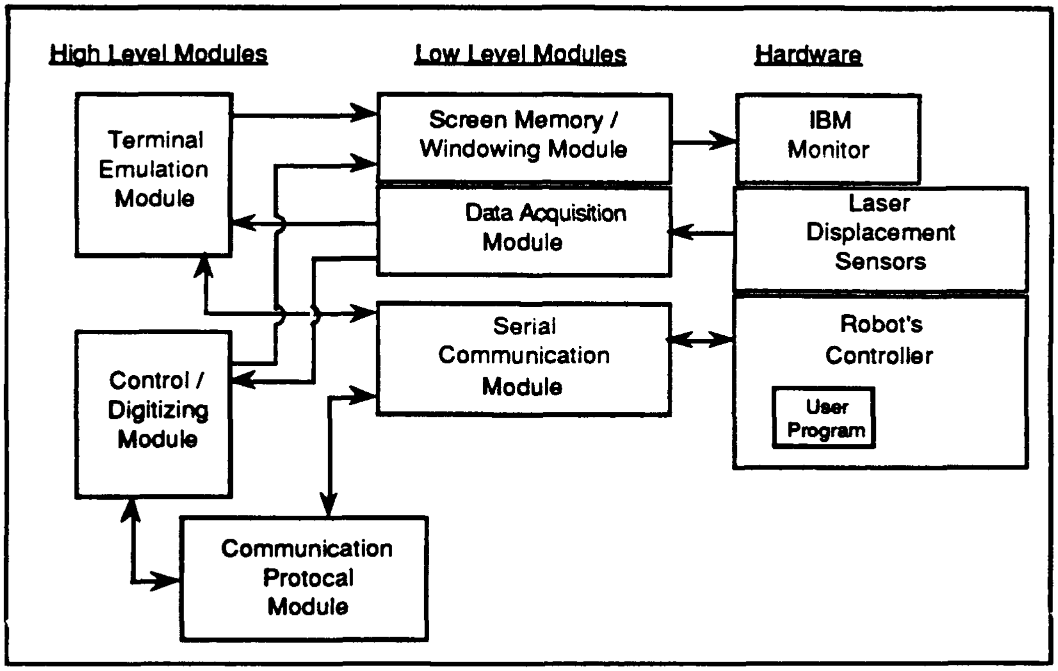
High Level Modules
Low Level Modules
Hardware
Terminal Emulation Module
Screen Memory / Windowing Module
IBM Monitor
Data Acquisition Module
Laser Displacement Sensors
Serial Communication Module
Robot's Controller
User Program
Control / Digitizing Module
Communication Protocol Module

Figure 5.2 Control Software Modules

The low level serial communication software was constrained to be interrupt driven due to the speed at which the robot's controller transmitted serial data. The interrupt service routine, IRQ4, written for this experiment, uses two circular queues to buffer in-coming and out-going data. When called, this routine checks the 8250 UART for receive-data ready. If there is in-coming data, the character is placed in the in-coming queue. Otherwise, if the transmitter holding register is empty then a character for the output queue is transmitted. The interrupt service routine executes fast enough to prevent an overflow from occurring. Thus, the high level control software only reads from and writes to the in-coming and out-going queues, respectively, to communicate with the robot's controller. When the control software wants to transmit data to the robot's controller, it fills the output queue with data and calls a flush routine which enables interrupts when the UART's transmitter-holding register is empty. After the out-going queue is empty, the flush routine disables interrupts on transmitter-holding-register empty and returns to the calling functions.

The screen memory management routines divide up the screen memory into two windows. The top window is used for displaying terminal emulation mode data. The bottom window is used for the digitizing control mode. Scrolling is supported in both windows. The center line of the screen memory is used for displaying current LDS readings.

The data acquisition module is used to read the LDS voltage values and convert them to displacement units (millimeters). The DAS-8 board uses 12 bits for the analog-to-digital conversion. Therefore, the displacement measurements are quantized in increments of 0.005 mm (20 mm / 2^12 = 5 mm). This quantization value is 5% of the magnitude of the robot's position repeatability and is therefore considered negligible. An out-of-range error signal from the LDS is also read and the results are passed on to higher level modules. If an out-of-range error is detected, then the higher level control modules try reorienting the LDS in order to get a good reading.

Higher level functions are written to handle the protocol of the robot's controller. These functions oversee the format of data transmitted to the robot's controller. Because the robot's controller operates in full-duplex, all data transmitted to the robot is checked for transmission errors. If a transmission error is detected, an abort signal (^U) is sent to the robot's controller and the command line is re-transmitted.

This software first runs in terminal emulation mode. In this mode, the robot is operated as if it is connected to a terminal and the robot can be manually positioned into its starting position before digitizing begins.

The control mode modules coordinates and controls the digitizing operation. This module reads the LDS values and the robot's position and orientation. It implements the surface-to-sensor orientation approaches and saves all digitized surface data points in a file. The control mode is initiated from the terminal mode by using the hot key, (^K). Once initiated, the software first prompts the user for overall control information, such as: output data file name, size of area to digitize, number of digitizing points to collect, and orientation approach to use.

A small VAL-II user program is executed on the robot's controller concurrently with the control software. This program is menu driven and has two options. Option 1 outputs the robot's current position and option 2 reads (X,Y,Z,O,A,T) data to reposition the robot. The program uses prompts to identify which mode it is in. The "?" prompt signifies the program is waiting for an option selection. The program displays a ">" prompt when it is waiting for (X,Y,Z,O,A,T) data and it uses the "*" prompt to signify that the robot has not completed a move.

5.3 Nonlinear Robot Position Accuracy

The PUMA robot used in this experiment has six rotary joints. With six degrees-of-freedom, the robot was able to position the LDS in any desired orientation. However, rotary joints have a nonlinear relation between changes in joint angles and changes in position of the end-effector. Therefore, the accuracy in positioning the end-effector is a function of the robot's configuration. In comparison, machining centers and coordinate measuring machines use three screw (or prismatic) joints which are orthogonal to each other, and changes in the screw joint angles are linearly related to changes in the tool's position. This linear relation holds for all tool positions in the operating envelope. These linear-orthogonal joints are able to achieve higher positioning accuracy over rotary joints. But rotary joints are necessary to dynamically reorient the LDS. This section will illustrate the nonlinearities of rotary joints using a two link robot.

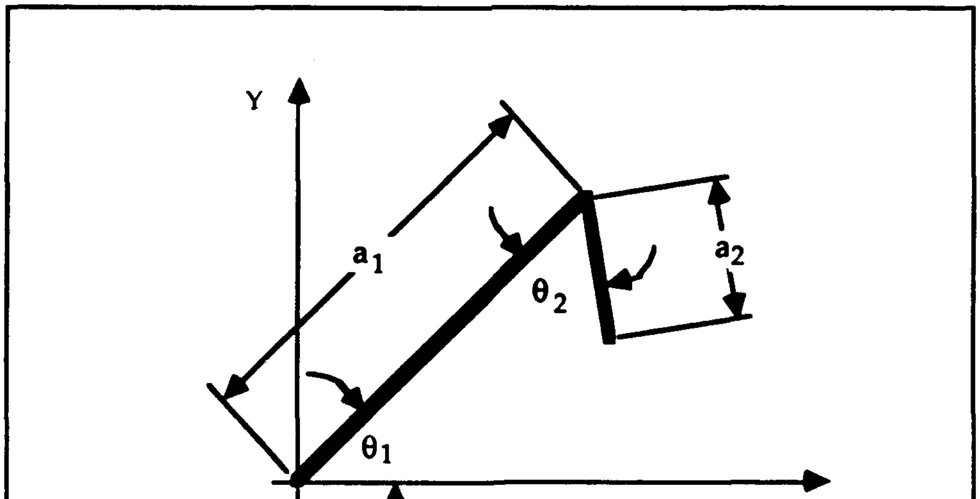

Figure 5.3 Two link Robot

The nonlinearities of positioning a robot with rotary joints will be illustrated using the two-link robot arm shown in Fig. 5.3. The joint angles are θ_1 and θ_2 are used to position the two links of length a_1 and a_2. The position of the end-effector as a function of joint angles is given by

$$\underset{\sim}{P}=[x,y]^T = f(\underset{\sim}{\theta}) \tag{5.1}$$

where $\underset{\sim}{P} \in R^2$, T represents transpose, $\underset{\sim}{\theta} = [\theta_1, \theta_2]^T \in R^2$,

$x = a_1 \cos(\theta_1) - a_2 \cos(\theta_1+\theta_2)$,

$y = a_1 \sin(\theta_1) - a_2 \sin(\theta_1+\theta_2)$,

$0 \leq \theta_1 \leq 2\pi$, and $0 \leq \theta_2 \leq \pi$.

First, let the joint angles be quantized so that $\theta_1 = m\,\Delta\theta$ and $\theta_2 = n\,\Delta\theta$ where m = 0,1,2,3,... and n = 0,1,2,3,... (This will typically be the case if optical encoders are used). To give a simple graphical illustration of the robot's nonlinearities, the operating envelope of the two-link robot of Fig. 5.3 is shown in Fig. 5.4 where $\Delta\theta = \pi/8$ and $a1=2\,a_2$. It is also shown in Fig. 5.5 where $\Delta\theta = \pi/8$ and $a1=a_2$. The semicircles represents the path of the end-effector as θ_1 is held constant at $m\,\Delta\theta$ and θ_2 varies from 0 to π. The concentric circles in the figures represents the path that the end-effector would take if θ_2 is held constant at $n\,\Delta\theta$ and θ_1 varies from 0 to 2π. The intersection of the circles and semicircles are all possible end-effector positions due to the quantization of the joint angles. The density of these intersection points represents the positioning resolution of the robots. Higher position accuracy corresponds to the point being closer together. Thus, the highest accuracy in the x axis is obtain when $\theta_2 = \pi$, and the highest accuracy in the y axis is obtain when $\theta_2 = 0$.

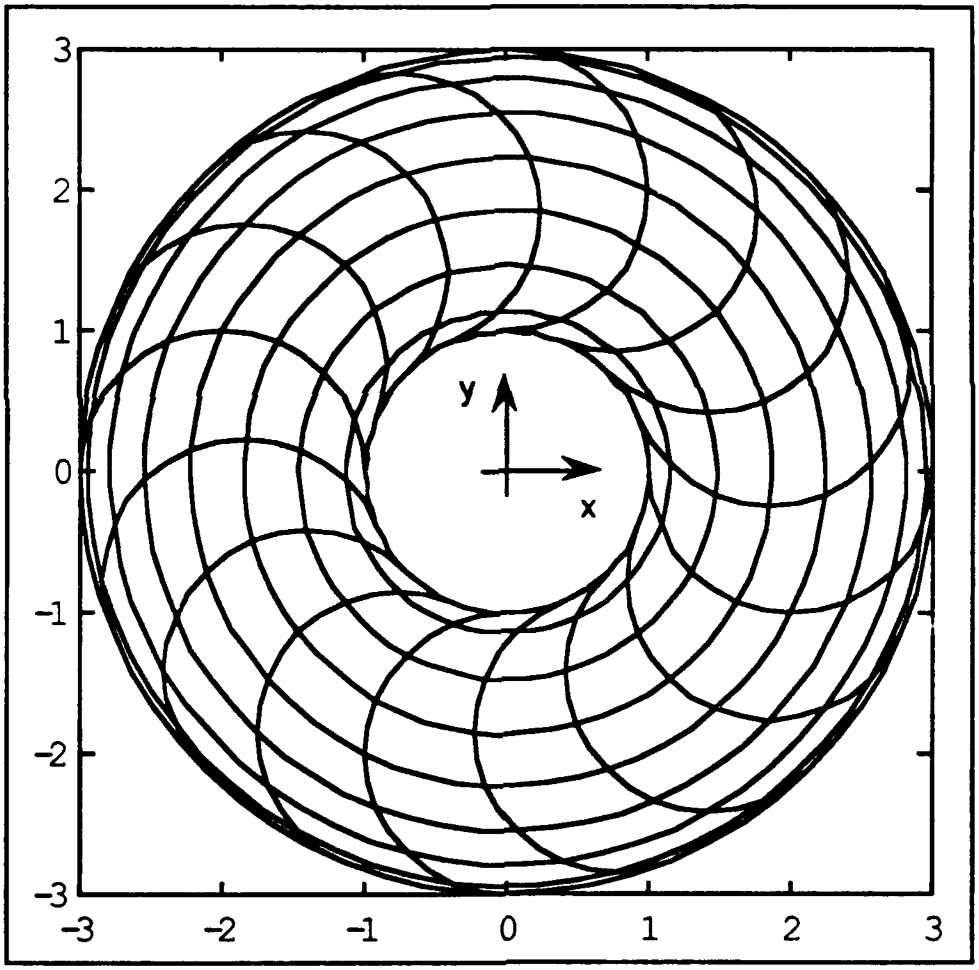

Figure 5.4 Positioning Locations within the Operating Envelope of a Two-Link Robot Arm with a_1=2 a_2.

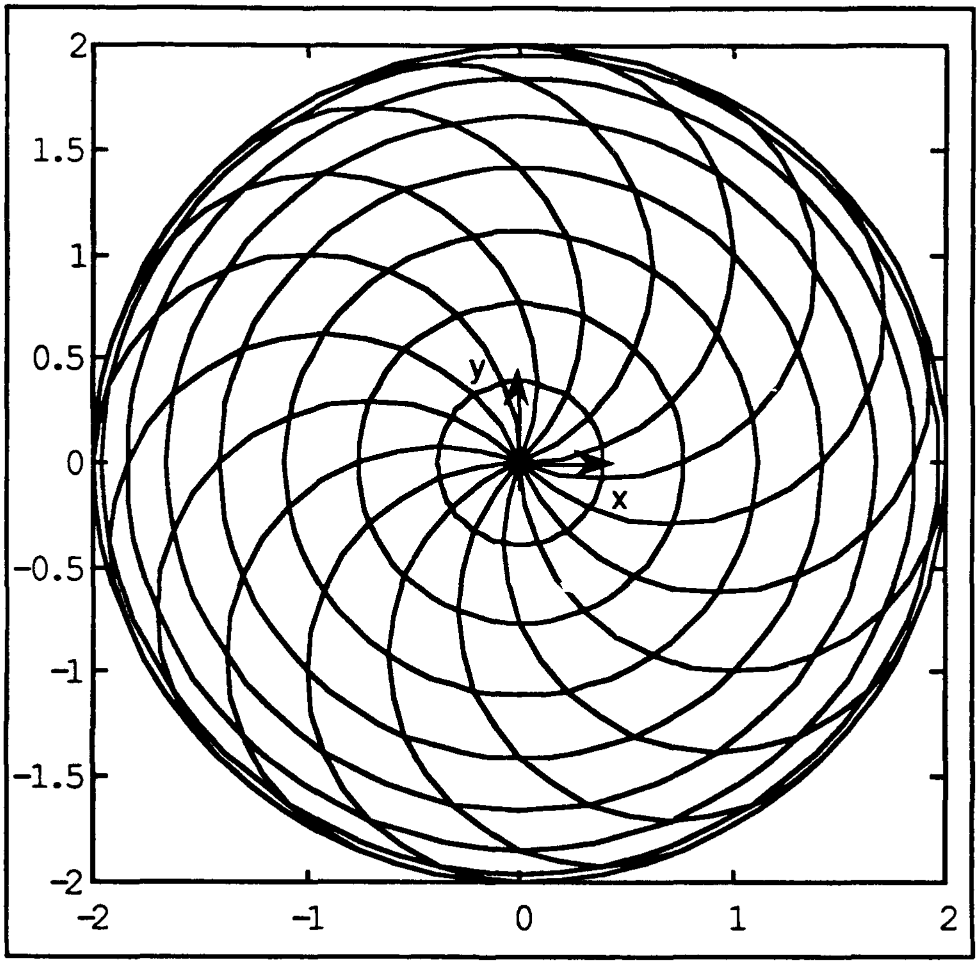

Figure 5.5 Positioning Locations within the Operating Envelope of a Two-Link Robot Arm with $a_1 = a_2$

Now, let θ_1 and θ_2 take on all real values within their respective ranges. Then, the time derivative of (5.1) is

$$\frac{d\underset{\sim}{P}}{dt} = \left[\frac{\partial \underset{\sim}{P}}{\partial \theta_1} \; \frac{\partial \underset{\sim}{P}}{\partial \theta_2}\right] \frac{d\underset{\sim}{\theta}}{dt} ,$$

where

$$\left[\frac{\partial \underset{\sim}{P}}{\partial\theta_1}\ \frac{\partial \underset{\sim}{P}}{\partial\theta_2}\right] = J(\underset{\sim}{\theta}) \in R^{2x2} \text{ which is called the Jacobian,}$$

$$\frac{\partial \underset{\sim}{P}}{\partial\theta_1} = \left[-a_1 \sin(\theta_1) + a_2 \sin(\theta_1+\theta_2), a_1 \cos(\theta_1) - a_2 \cos(\theta_1+\theta_2)\right]^T,$$

and

$$\frac{\partial \underset{\sim}{P}}{\partial\theta_2} = \left[a_2 \sin(\theta_1+\theta_2), -a_2 \cos(\theta_1+\theta_2)\right]^T.$$

Thus, $J(\underset{\sim}{\theta})$ relates the change in joint angles to the change in end-effector position. In [49,50], Yoshikawa used the Jacobian of a robot to define the manipulability ellipsoid. He showed that the subset S_v of $\frac{d\underset{\sim}{P}}{dt}$ in the space R^m realizing $\frac{d\underset{\sim}{\theta}}{dt}$ such that $\left\|\frac{d\underset{\sim}{\theta}}{dt}\right\| \leq 1$ is an ellipsoid where the principal axes are found directly from the singular value decomposition of the Jacobian. He used the ellipsoid to introduce the idea of manipulability, however, these ellipsoids can also be used to determine a robot's position accuracy for a given configuration.

The ellipsoids map incremental changes in the position of the end-effector for a given set incremental changes in the rotary joint angles. As seen in the previous example where the rotary joint angle is measured using an optical encoder, smaller changes in the endeffectors position for the same change in the rotary angle corresponds to higher positioning accuracy. The two-link robot with $a_1=2a_2$ was seen to have the highest resolution with $\theta_2 \approx 0$. A small ellipsoid represents small end-effector movement for the given set of joint angular motion. Thus, smaller ellipsoids correspond to higher positioning resolution.

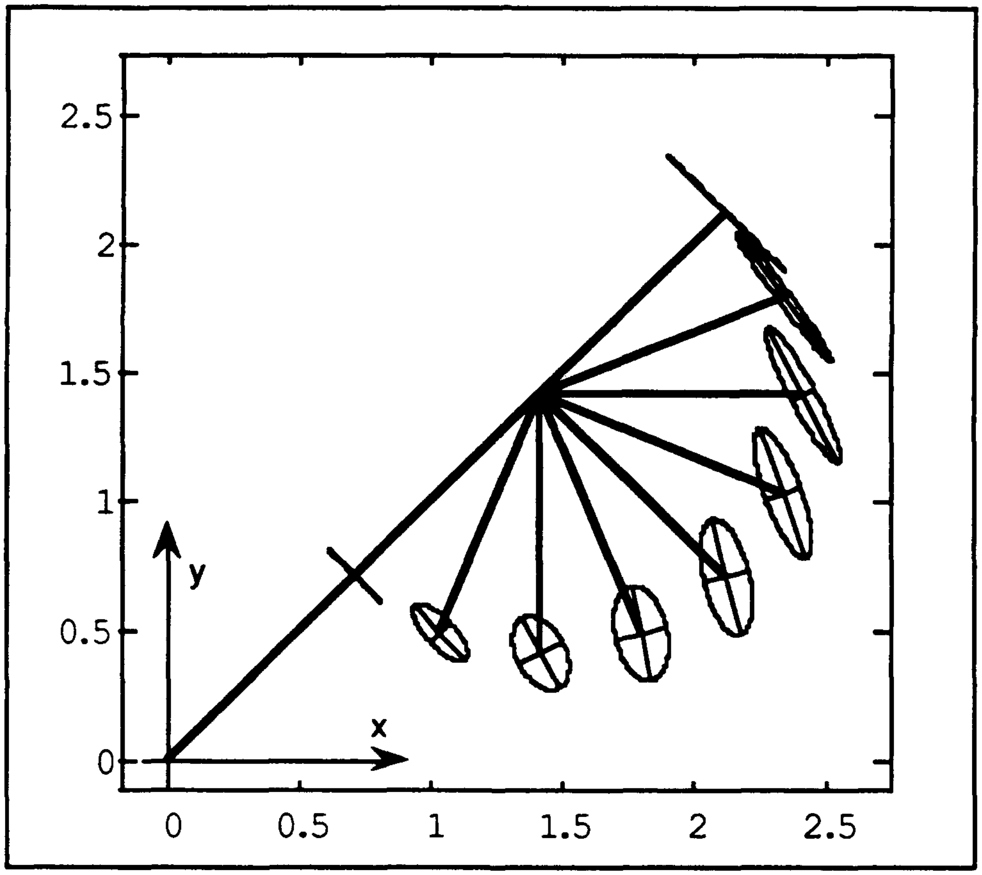

Figure 5.6 Manipulability Ellipsoids with $a_1 = 2\ a_2$.

The principal axes of the ellipsoid shows the direction in which $\frac{d\underset{\sim}{P}}{dt}$ will have the highest and lowest resolution. If the axes have the same magnitude then the resolution will be equal in all directions. These ellipsoids for the two-link robot have been plotted in Fig. 5.6 and Fig. 5.7 for select robot configurations.

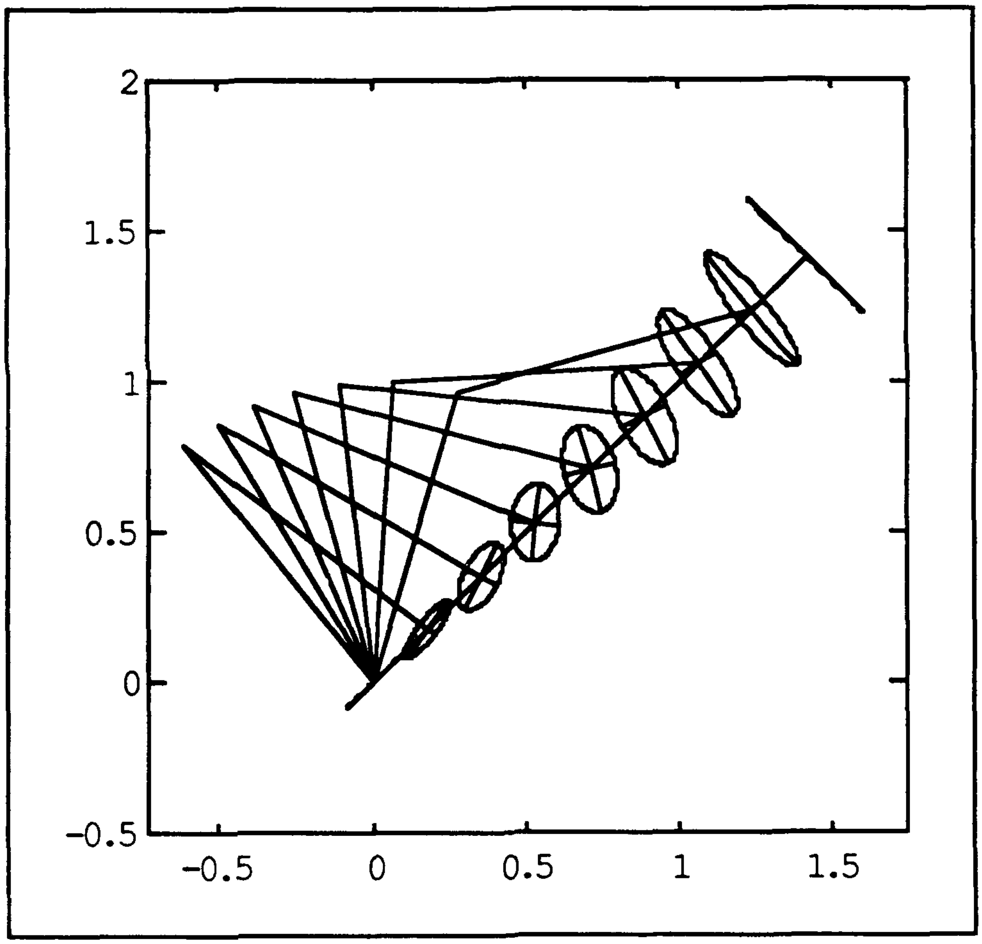

Figure 5.7 Manipulability Ellipsoids with $a_1 = a_2$.

Fig. 5.6 shows the robot with $a_1 = 2\ a_2$, $\theta_1 = \pi/4$, and $\theta_2 = n\ \pi/8$ where n=0,1,2,..,8. Fig. 5.7 shows the robot with $a_1=a_2$ and the end-effector moving radially out at $\pi/4$. Note that the smaller ellipsoids are located in the same area as the higher resolution areas of Fig. 5.4 and Fig. 5.5. These examples illustrate that rotary joint robots have nonlinear positioning accuracy. That is the accuracy of the robot changes for different configurations. Evaluating the manipulability ellipsoids over the operation envelope of the robot identifies areas were the robot has the highest positioning accuracy.

5.4 Summary

This chapter outlined the system architecture of the digitizing system designed for this research. Both the hardware and the software of the system was explained. The nonlinear positioning accuracy of an ideal robot with rotary joints was illustrated using a two link robot. The next chapter will discuss the experiments conducted with this digitizing system.

CHAPTER VI

EXPERIMENT

This chapter discusses the procedures used to calibrate the digitizing system. A mesh diagram of the data collected from digitizing a simple concave and convex surface is also presented. The digitizing rate of the system was measured. A qualitative analysis of the performance of the two extrapolation methods is given, and an observation that high surface reflectivity adversely affects the digitizing system is reported.

6.1 Calibration

Before using the digitizing system, the Keyence LB-72/LB-12 Laser Displacement Sensors were calibrated and a transformation matrix from the end-effector to the LDS was defined. The LDS have two calibration adjustments. One is the 0-ADJ adjuster trimmer which adjusts the 0 volt stand-off distance. The stand-off distance on one LDS was set to roughly the center of its measuring range. Then, the other LDS was adjusted carefully to have the same stand-off distance as the first LDS. The second calibration adjustment is the SPAN adjuster trimmer. This adjustment varies the volts per displacement value. Both LDS were calibrated to 5 volts per 10 mm displacement.

After the lasers were calibrated, the transformation matrix from the end-effector to the 0 volt reference position was determined. The PUMA robot's controller has a reserved name for this transformation matrix, named "TOOL". Once this transformation matrix is defined, the robot can be positioned using locations for the LDS rather than the end-effector. Robotic system calibration has been studied previously, but not in the context of the robot being used as a measurement device [45,46,47].

6.2 Digitizing Rate

The overall digitizing rate was measured in the laboratory. The results are shown in Table 6.1. The rate was measured while using the Multiple Beam Approach to digitize a plane.

Table 6.1 Digitizing Rate

Motor Speed	Sampling Distance	Digitizing Rate
5%	10 mm	0.77 (data points / second)
5%	1 mm	0.91
100%	10 mm	1.00
100%	1 mm	0.91

The serial communication and error checking between the IBM PC and the robot's controller is believed to contribute significantly to the time needed to digitize. Speed improvements could possibly be made by using a more sophisticated communication protocol available on the robot's controller. The serial communication interface used was chosen because it was thought to be faster to implement. In addition, the PUMA robot controller uses a deceleration mode when the arm approaches the final position. If the overall distance to go is small, the arm does not reach its full speed but always remains in the deceleration mode. Thus, the communication protocol used and the deceleration mode is believed to be the major reason the digitizing speed is not significantly affected by the motor speed setting.

6.3 Demonstration of Extrapolation Approaches

Both the Multiple Beam Approach and the Extrapolation Approach to maintaining surface-to-sensor orientation were demonstrated by digitizing a complex surface. The complex surface used is a draw die model of an automoble fire wall, see Fig. 6.1. The model was donated courtesy of General Motors. The left half of the model was digitized and ploted in Fig. 6.2. A sampling arc length of 2.5 mm was used.

Regardless of the approach used, the surface is digitized in a grid pattern. The distance between adjacent points, as measured along the

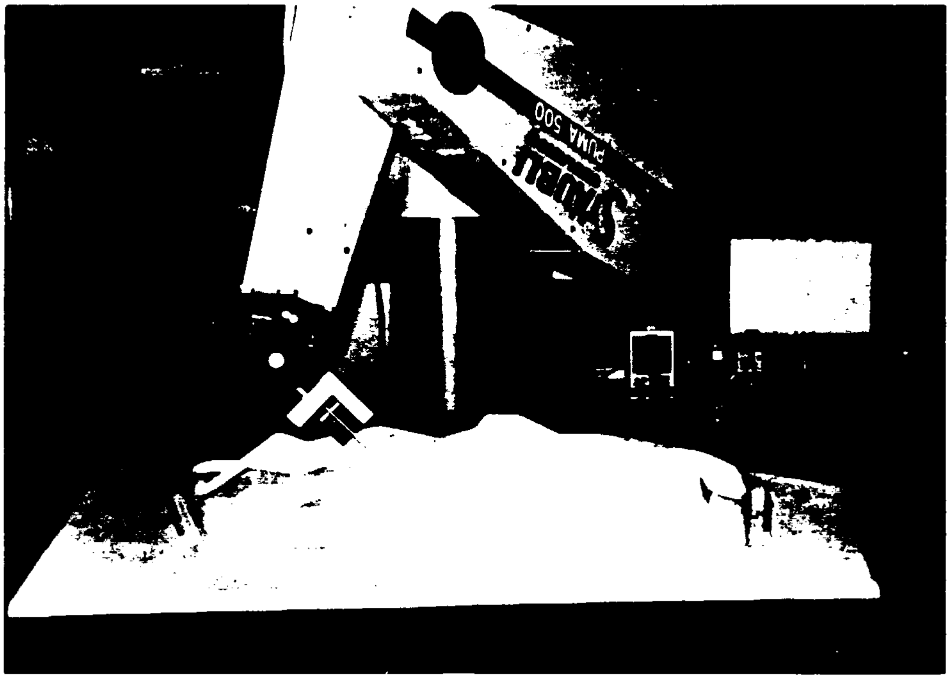

Figure 6.1 Photograph of Complex Surface and Digitizing System

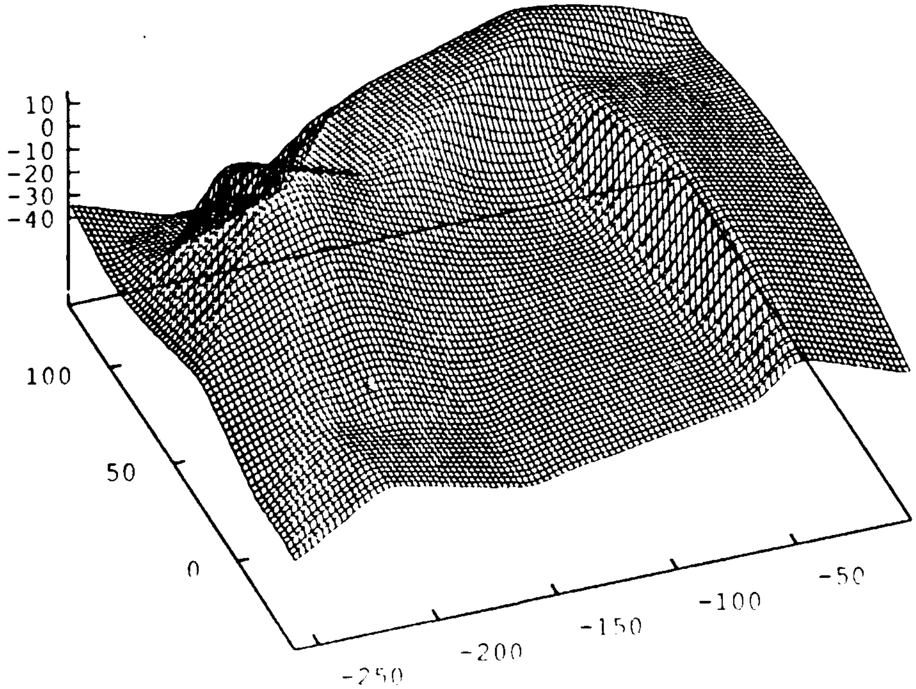

Figure 6.2 Plot of Digitized Complex Surface (units=mm)

coordinate axis, is the same in any row or in any column. The surface is digitized row by row, where a row is parallel to the x axis. When the end of the row is reached, digitizing continues on the next row but in the opposite direction. Therefore, if a row is digitized in the positive x direction, then the next row will be digitized in the negative x direction. For the Multiple Beam Approach, the second laser would be leading the digitizing laser on one row and following the digitizing laser on the next row.

The Multiple Beam Approach using two LDS gave consistent, reliable results provided the surface's radius of curvature was large in comparison with the distance between the two lasers. Smaller radius of curvatures produce larger errors between the predicted and the actual position and orientation of the sculptured surface, as expected. This observation is, to some degree, intuitive if you consider digitizing the cross-section of a semi-circle which has a smaller diameter than the distance between the two laser beams. In this extreme case, only one laser beam, at most, shines on the semi-circle at any time. Under this condition, the Multiple Beam Approach fails. However, the Extrapolation Approach could be used because the distance between measured points can be adjusted as discussed in chapter IV.

For the polynomial extrapolation approach, a 2nd order polynomial extrapolation method was implemented. This order of polynomial was observed to be sensitive to errors in surface point measurements. This sensitivity is increased with smaller digitizing intervals. This is illustrated in Fig. 6.3.

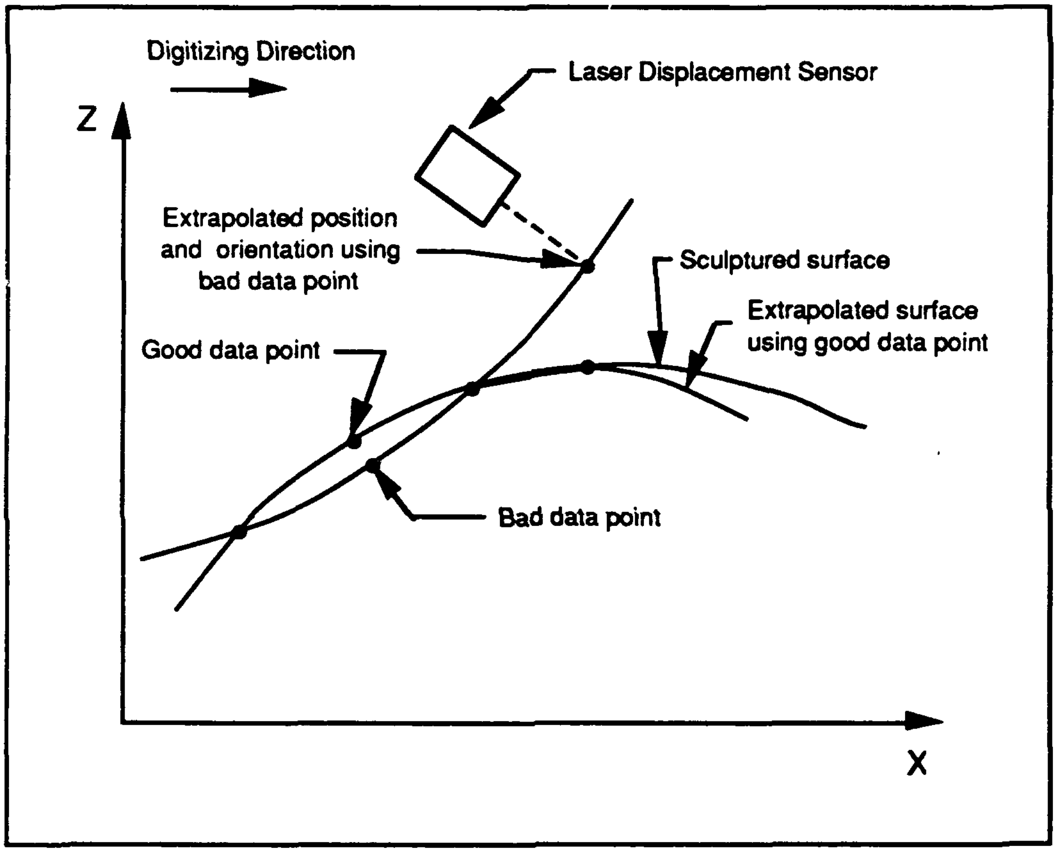
Digitizing Direction
Laser Displacement Sensor
Z
Extrapolated position and orientation using bad data point
Sculptured surface
Extrapolated surface using good data point
Good data point
Bad data point
X

Figure 6.3 2nd Order Polynomial Extrapolation with Bad Data Point

Note that changes in the middle point changes the predicted surface from concave to convex. In this case, the distance between digitized points in the X axis was held constant rather than the arc length as in chapter IV.

6.4 Surface Reflectivity

The reflectivity of the sculptured surface affected the LDS's ability to function properly. The LDS failed to provide correct displacement readings when digitizing highly reflective surfaces. If a surface is highly reflective and the LDS is oriented so that the laser beam is reflected away from the sensor in the LDS then an error reading will result.

6.5 Angle of Incidence Error

The measurement error caused by the LDS being oriented in a non-perpendicular (90°) orientation with the surface was evaluated. This was done by repetitively digitizing the same points on a flat surface with the LDS oriented at 60°, 90°, and 120°. The surface digitized was a sheet of paper taped onto a plane of glass. For each LDS orientation, thirty points parallel to the x axis were digitized five times and the average z axis values determined. The largest variation between the z axis readings was <±0.005" which is within the repeatability of the robot and accuracy of the LDS. The difference between the average values with the LDS at 60° and the average values with the LDS at 90° is plotted in Fig. 6.4. Also, the difference between the average values with the LDS at 120° and the average values with the LDS at 90° is plotted in Fig. 6.5.

The average z axis values with the LDS oriented at 90° has the smallest LDS measurement error. The difference between this value and the average values measured with the LDS oriented at 60° and 120° shows the measurement errors caused by a non-perpendicular orientation. These errors are a combination of the inaccuracy in the LDS measurement and in the inaccuracy in calibrating the robot. The average error value of the plot in Fig. 6.4 is -1.50 mm and the average error value of the plot in Fig. 6.5 is 1.43 mm. These are significant errors and they illustrate the importance of maintaining a perpendicular orientation between the LDS and the surface.

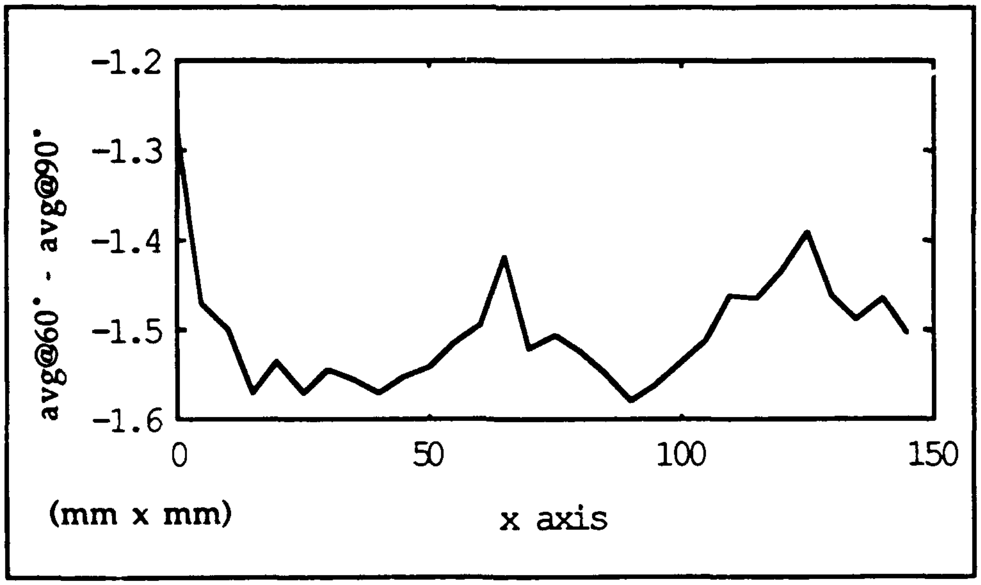

Figure 6.4 The Difference Between the Average Digitized z Axis Value with the LDS Oriented at 60° and the Average Value with the LDS Oriented at 90°

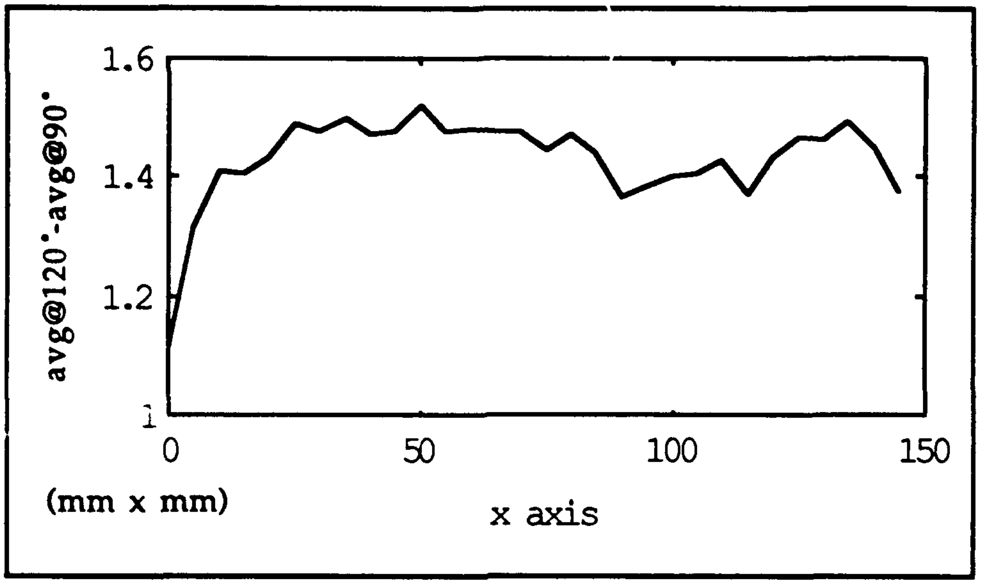

Figure 6.5 The Difference Between the Average Digitized z Axis Value with the LDS Oriented at 120° and the Average Value with the LDS Oriented at 90°

6.6 Summary

This experiment demonstrated the feasibility of both extrapolation methods being implemented in a digitizing system. They were successful at keeping the LDS within desired position and orientation limits while digitizing simple concave and convex surfaces. In addition, the experiment provided some insight of the approaches sensitivity to bad data and of the LDS sensitivity to surface reflectivity.

CHAPTER VII

CONCLUSIONS

This Master's research project implemented a robotic non-contact 3-D digitizing system to digitize unknown sculptured surfaces. Two extrapolation approaches, the multiple beam approach and the polynomial extrapolation approach, were demonstrated with this digitizing system. This project illustrated that more general sculptured surfaces can be digitized using a six degrees-of-freedom robot to position and orient the LDS than can be digitized using a three axis coordinate measuring machine or machining center.

Another advantage of this digitizing system is that it was built on feasibly available and relatively low cost equipment, such as, robot manipulators and a microcomputers.

As discussed in chapter II, keeping the laser beam perpendicular to the surface is a key factor that affects the precision and robustness of the digitizing process. This research has shown that if the surface has a finite maximum curvature, then a sampling arc length can be selected which will keep the error parameters of the LDS within desired bounds. The positioning accuracy of a rotary joint machine was show to be nonlinear. The positioning accuracy of the robot is a limiting factor in the overall accuracy of this digitizing system.

Typically, digitizing a sculpture surface produces more data points than required to describe the surface. In this case, the data points can be lumped together to create a mathematical model to describe the surface. The mathematical surface models provides a more flexible and efficient way of describing the surface. More work, however, needs to be done to automate the process of going from digitized data points to a mathematical surface model.

APPENDIX

COMPANY REFERENCE LIST

Laser Displacement Sensors

Aromat Corporation
629 Central Avenue
New Providence, NJ 07974
Phone: 800-228-2350

CyberOptics Corporation
2331 University Avenue SE
Minneapolis, Minnesota 55414
Phone: 612-331-5702

Keyence Corporation of America
17-17 Route 208 North
Far Lawn, NJ 07410
Phone: 800-328-2238

Kohgakusha Engineering Co., LTD
Osumi-Bld., Higashi-Ikebukuro 2-39-2
Toshima-Ku, Tokyo, Japan T170
Phone: 03-987-6331

Micro Switch
Honeywell Inc.
11 West Spring Street
Freeport, Illinois 61032-9945
Phone: 815-235-6600

Perceptron
23855 Research Drive
Farmington Hills, Michigan 48024
Phone: 313-478-7710

Renishaw Inc.
623 Cooper Court
Schaumburg, IL 60173
Phone: 708-843-3666

Selcom
P.O. Box 250
Valdes, North Carolina 28670
Phone: 704-874-4102

SAM, Inc.
6360 Hawthorne Drive
Winsor, Ontario (Canada) N8T1J9
Phone: 519-944-6641

Medar
38700 Grand River Avenue
Farmington Hills, Michigan 48335
Phone: 313-477-3900

Laser Digitizing Systems

Chesapeake Laser Systems
4473 Forbes Blvd.
Lanham, Maryland 20706
Phone: 301-459-7977

Hymark Ltd.
Ottawa, Canada
Phone: 613-727-1584

Laser Design Inc.
9401 James Avenue South • Suite 162
Minneapolis, Minnesota 55431
Phone: 612-884-9648

Okada Machinery Corporation
c/o Tomen America Inc,
Chicago Branch
1000 Corporate Grove Drive
Buffalo Grove, IL 60089-4507
Phone: 708-215-6850

Robotic Vision Systems Inc. (RVSI)
425 Rabro East
Hauppauge, New York 11788

Sharnoa Corporation
23996 Freeway Park Drive
Farmington Hills, Michigan 48335
Phone: 313-476-2600

REFERENCES

[1] D. J. Porembiak, Private Communication, General Motor Corporation, Advanced Development Center, September, 1991.

[2] K. G. Harding, "Sensors for the '90s," Manufacturing Engineering, April 1991, pp. 57-61.

[3] K. Saito, et al., "Noncontact 3-D Digitizing and Machining System for Free-Form Surfaces," *Annals of the CIRP*, vol. 40, p. 483-486,1991.

[4] K. Kobayashi, et al., "Laser-scanning imaging system for real-time measurements of 3-D object profiles," *Opt. Commun. (Netherlands)*, vol. 74, no. 3-4, p. 165-170, Dec. 1989.

[5] "Keyence LB-70,LB-72 Laser Displacement Sensor Instruction Manual," *Keyence Corporation*, 1991.

[6] B. Mason, and A. L. Harfvey, "Digitizing. Printless part programming comes of age," *Tooling and Production*, vol. 56, no. 6, p. 188-189, Sep. 1990.

[7] B. K. P. Horn, "Robot Vision," *The MIT Press, Cambridge*, MA, 1986.

[8] "Laser Displacement Sensor Catagories," CyberOptics, 1991.

[9] M. Soucy, et al., "Behavior of the center of gravity of a reflected Gaussian laser spot near a surface reflectance discontinuity," *Ind. Metrol. (Netherlands)*, vol 1, no. 3, p. 261-274, Sept. 1990.

[10] E. J. Little, and A. N. Vavreck, "Condensation-assisted triangulation system (CATS)," *Conference Record of the IEEE Industry Applications Society Annual Meeting (Cat. No90CH2792-0), San Diego, CA, USA*, Oct. 1989 (New York, NY, USA: IEEE 1990), vol. 2, p. 1675-7.

[11] P. Saint-Marc, et al., "A versatile PC-based range finding system," IEEE Transactions on Robotics and Automation, vol. 7, no. 2 p. 250-256, Apr. 1991.

[12] T. Matsumoto, "3D profile measuring instrument for shoes CAD system using laser displacement sensor," *Syst. Control (Japan)*, vol. 32, no. 5, p. 321-326, May 1988 (In Japanese).

[13] R. Bolle, and B. C. Vemuri, "On three-dimensional surface reconstruction methods," *IEEE Transactions on Pattern Analysis and Machine Intelligence*, vol. 13, no. 1, p. 1-13, Jan 1991.

[14] M. E. Mortenson, "Geometric Modeling," *John Wiley and Sons*, 1985.

[15] W. E. Grimson, "An implementation of computational theory for visual surface interpolation," *Computer Vision, Graphics, Image Processing*, vol. 6, no. 22, p.39-69, 1983.

[16] S. Muraki, et al., "3-D surface reconstruction from contour line image by a regularization method," *Proc. SPIE - Int. Soc. Opt. Eng. (USA)*, vol. 1395, p. 226-235, Sep. 1990.

[17] C. Chen and Y. F. Zheng, "Visual surface reconstruction using patches," Report, AML-07-C2-91, *Dept. of Electrical Engineering, The Ohio State University*, 1991.

[18] B. C. Vemuri, A. Mitiche, and J. K. Arraswal, "Curvature - based representation of objects from range data," *Image and Vision Comput.*, vol. 4, no. 2, p. 107-114, May 1986.

[19] B. C. Vemuri, "Representation and recognition of objects from dense range maps," Ph.D dissertation, *Univ. of Texas at Austin, Dept. of Electrical and computer Engineering*, Austin, TX, 1987.

[20]. D. B. Torok, "Scanning the options: hand held, non-contact laser scanners," *Material Handling Engineering*, vol. 7, p. 75-76, Sep. 1990.

[21] I. Moring, et al., "Acquisition of three-dimensional image data by a scanning laser range finder", *Optical Engineering*, vol. 28, p. 897-902, Aug. 1989.

[22] G. T. Reid, et al., "A laser scanning camera for range data acquisition", *Journal of Physics. D, Applied Physics*, vol. 21 no. 10s, p. s1-3, Oct. 1988.

[23] V. Noviski, "When to use scanning laser sensors", *Machine Design*, vol. 60, PP. 120+, Sep. 1988.

[24] C. R. Steinmetz, "Performance evaluation of laser displacement interferometry on a precision coordinate measuring machine," *Ind. Metro. (Netherlands)*, vol. 1, no. 3, p. 165-191, Sep. 1990.

[25] E. J. Davis, "The scope of three dimensional topography," *Ind. Metrol. (Netherlands)*, vol. 1, no. 3, p. 193-216, Sep. 1990.

[26] S. K. Case, et al., "3-D inspection for quality control in surface mount manufacturing," *The Proceedings of SMTCON, Surface Mount Technology Conference and Exposition, Alantic City, NJ, USA*, p. 199-206, 3-6 April 1990.

[27] G. Begin, "Real time large depth of field 3-D vision system [robot vision]," *Proc. SPIE - Int. Soc. Opt. Eng. (USA)*, vol. 900, p. 25-31, Jan. 1988.

[28] S. J. Marshall, et al., "Development of a 3-D data acquisition system for human facial imaging," *Proc. SPIE - Int. Soc. Opt. Eng. (USA)*, vol. 1231, p. 61-74, Feb. 1990.

[29] T. Huiming, "Laser non-contacting displacement measurement," *Proc. SPIE - Int. Soc. Opt. Eng. (USA)*, vol. 1230, p. 427-428, Aug. 1990.

[30] M. Samson, and M. L. Dufour, "A new stereo laser triangulation device for specular surface inspection," *Proc. SPIE - Int. Soc. Opt. Eng. (USA)*, vol. 1332, p. 314-322, Jul. 1990.

[31] T. Kanada, "A three-dimensional surface profile measuring system with a specimen-levelling device," *Meas. Sci. Technol. (UK)*, vol. 2, no. 3, PP. 191-197, Mar. 1991.

[32] "Machining centers that can digitize and reproduce models," *Modern Machine Shop*, vol. 58, p. 126+, Nov. 1985.

[33] "A new entry in laser digitizing," *American Machinist*, vol. 134, p. 43, Jan. 1990.

[32] 3D laser digitizing at 10,000 points/sec," *American Machinist*, vol. 133, p. 17, Apr. 1989.

[34] "Laser head turns machining center into 3D digitizing system," *Modern Machine Shop*, vol. 61, p. 162+, Dec. 1988.

[35] T. Miyoshi, et al., "Development of an Automatic Non-Contact Measuring System of 3-D Model Shapes for Injection Molds," *JSPE*, vol. 55, no. 2, p. 393, 1987.

[36] B. Breuckmann, "Optical 3 D-measuring systems for online-applications," *Tech. Mess. tm (Germany)*, vol. 57, no. 10, p. 389-394, Oct. 1990, (In German).

[37] C. P. Hoffmann, "Non-contact optical distance measurement using PSD (position sensitive detector) elements," *Technica (Switzerland)*, vol. 39, no. 25, p. 93-95, Nov. 1990, (In German).

[38] T. Miyoshi, et al., "Development of noncontact 3-D digitizing system," *J. Jpn. Soc. Precis. Eng. (Japan)*, vol. 56, no. 6, p. 1021-1026, June 1990, (In Japanese).

[39] B. I. Rebaglia, "Laser systems in industrial environment metrological applications," *Autom. Strum.(Italy)*, vol. 38, no. 7-8, p. 121-128, July-Aug 1990, (In Italian).

[40] A. Sona, "Introduction to the laser," *Elettrotecnica (Italy)*, vol. 77, no. 6, p. 515-522, June 1990, (In Italian).

[41] V. Kuhnel, et al., "Laser system with quadrant detector for measuring small side shifts," *Jemna Mech. Opt. (Czechoslovakia)*, vol. 35, no. 10, p. 299-306, Oct. 1990, (In Czech).

[42] H. Nishino, "Acquisition of 3-dimensional object shape using slit-ray projection and reconstruction of surface model," *Systems and Computers in Japan*, vol. 21, no. 13, p. 42-53, 1990.

[43] C. H. Menq, "Statistical evaluation of form tolerances using discrete measurement data," *Advances in Integrated Product Design and Manufacturing American Society of Mechanical Engineers,* vol. 47, p. 135-149, 1990.

[44] F. R. Livingstone, M. Rioux, "Development of a large field of view 3-D vision system", *Proc. SPIE - Int. Soc. Opt. Eng. (USA),* vol. 665, p. 188-192, Jun. 1986.

[45] J. Chen and L. M. Chao, "Positioning error analysis for robot manipulators with all rotary joints," *IEEE J. of Robotics and Automation,* vol. RA-3, no. 6, p. 539-545, Dec. 1987.

[46] J. H. Borm and C. H. Meng, "Determination of optimal measurement configurations for robot calibration based on observability measure," *Int. J. of Robotics Research,* vol. 10, no. 1, p. 52-63, Feb. 1991.

[47] S. A. Hayati, "Robot arm geometric link parameter estimation," *Proc. 22nd IEEE CDC,* San Antonio, Texas, p. 1477-1483, Dec. 1983.

[48] THOMAS, G. B. J. and FINNEY, R. L. (1980), Calculus and Analytic Geometry. Arrison-Wesley, Reading, Mass.; pp. 551

[49] T. Yoshikawa, "Analysis and Control of Robot Manipulatiors with Redundancy," *Preprints 1st Int. Symp. of Robotics Res,* p. 735-747, Sep. 1983.

[50] T. Yoshikawa, "Manipulability of Robotic Mechanisms," *Int. J. of Robotics Research,* vol. 4, no. 2, p. 3-9, 1985.